UNIVERSITY OF CALIFORNIA

Santa Barbara

Remote Sensing of Urban Climate and Vegetation in Los Angeles

A dissertation submitted in partial satisfaction

of the requirements for the degree

Doctor of Philosophy

in

Geography

By

Erin Blake Wetherley

Committee in charge:

Professor Joseph P. McFadden, Chair

Professor Dar A. Roberts

Professor C. Naomi Tague

Dale A. Quattrochi, Ph.D.

December 2018

The dissertation of Erin Blake Wetherley is approved.

_____

Dar A. Roberts

_____

C. Naomi Tague

_____

Dale A. Quattrochi

_____

Joseph P. McFadden, Committee Chair

September 2018

Remote Sensing of Urban Climate and Vegetation in Los Angeles

ACKNOWLEDGEMENTS

I would like to thank my co-advisors, Joseph McFadden and Dar Roberts, for their support in almost every aspect of this dissertation, for their wise mentorship, for helping me stay funded, and for their patience.

Thank you to my dissertation committee members, Naomi Tague and Dale Quattrochi, for their guidance and willingness to share their expertise. I would also like to thank my former committee member, Phaedon Kyriakidis for his help in getting this project off the ground.

Thanks to all colleagues and collaborators, from inside and outside the lab, for insightful discussion and thoughtful critique: David Miller, Michael Allen, Olaf Menzer, Helen Chen, Susan Meerdink, Mingquan Chen, Sarah Wells Shivers, Seth Peterson, Zachary Tane, Alana Ayasse, Fernanda Ribeiro, Gabriel Antunes Daldegan, Chris Kibbler, Mike Alonzo, Marcia Zilli, Brandi Gamelin, Charles Jones, Becky Powell, Ben Somers, Jeroen Degerickx, Laurent Tits, and Paul Gader.

Additionally, thank you to the several people who volunteered to help me in the field: Noah Eckhous, Annie Ferguson, Raul Garcia, Nareg Gourdikian, David Liu, Susan Meerdink, Keri Opalk, Sarah Shivers, and Nancy Yu.

Special thanks to Susan Meerdink for processing data, sharing code, connecting me to NASA conference calls, providing IT support, organizing social gatherings, and doing several other things that generally helped me make it to the end.

Thanks to the Cohort of 2012. You're all amazing.

Thank you to my supporters: Mom, Dad, Emily, Russell, Josh, Jasper, Bill, Lu, Arthur, and Payam. I succeeded because of you.

This work was funded in part by the NASA Earth and Space Science Fellowship (NNX16AO58H), the Brython Davis Endowment Graduate Fellowship, and the Belgian Science Policy Office in the framework of the STEREO III Program—Project UrbanEARS (SR/00/307). Additional support from the Academic Senate at UCSB and from Jack and Laura Dangermond allowed me to share this research at conferences.

VITAE OF ERIN BLAKE WETHERLEY DECEMBER 2018

EDUCATION

2018	PhD in Geography, University of California, Santa Barbara, CA
2008	BA in Environmental Studies and History, Brown University, Providence, RI

PROFESSIONAL EMPLOYMENT

2008-2012	GIS Manager, Civil War Trust, Washington, DC
2007	Summer Internship, U.S. Public Interest Research Group, Washington, DC
2006	Summer Internship, Western Watersheds Project, Boise, ID

PUBLICATIONS

1. Dennison, P.E., Kokaly, R.F., Thompson, D.R. Qi, Y., Daughtry, C.S.T., Meerdink, S.K., Quemada, M., Gader, P.D., Roberts, D.A., and **Wetherley, E.B.** Submitted. Comparison of Methods for Modeling Fractional Cover using Simulated Satellite Hyperspectral Imager Spectra. Remote Sensing of Environment.
2. Roberts, D.A., Roth, K., Perroy, R., Meerdink, S.K., and **Wetherley, E.B.** Submitted. Hyperspectral Vegetation Indices. In, Hyperspectral Remote Sensing of Vegetation, 2nd Edition, Ed. By Prasad S. Thenkabail et al.
3. **Wetherley, E.B.**, McFadden, J.P, and Roberts, D.A. 2018. "Megacity-Scale Analysis of Urban Vegetation Temperatures." Remote Sensing of Environment 213 (4): 18-33.
4. Goodridge, B.M., Hanan, E.J., Aguilera, R., **Wetherley, E.B.**, Chen, Y., D'Antonio, C.M., Melack, J.M. 2018 "Retention of nitrogen following wildfire in a chaparral ecosystem." Ecosystems.
5. **Wetherley, E.B.**, Roberts, D.A., and McFadden, J.P. 2017. "Mapping Spectrally Similar Urban Materials at Sub-Pixel Scales." Remote Sensing of Environment 195 (6): 170–83.
6. Roberts, D., Alonzo, M., **Wetherley, E.B.**, Dudley, K., and Dennison, P. 2017. Multiscale analysis of urban areas using mixing models. In, Integrating Scale in Remote Sensing and GIS, Ed. By Dale Quattrochi et al.
7. Somers, B., Tits, L., Roberts, D.A., and **Wetherley, E.B.** 2016. Endmember Library Approaches to Resolve Spectral Mixing Problems in Remotely Sensed Data: Potential Challenges and Applications. In, Resolving Spectral Mixtures with applications from ultrafast time-resolved spectroscopy to super-resolution imaging, Ed. By C. Ruckbusch.

AWARDS

2016-2018	NASA Earth and Space Science Fellowship
2018	Excellence in Research Award, UCSB Geography
2017	American Geophysical Union Outstanding Student Presentation Award
2017	Estes Memorial Award, UCSB Geography
2017	American Meteorological Society Outstanding Poster Presentation Award
2015-2016	Brython Davis Endowment Graduate Fellowship

ABSTRACT

Remote Sensing of Urban Climate and Vegetation in Los Angeles

by

Erin Blake Wetherley

In cities, microclimates are created by local mixtures of vegetation, constructed materials, vertical structure, and moisture, with significant consequences for human health, air quality, and resource use. Vegetation can moderate microclimates through evapotranspiration, however this function is dependent on local conditions so its effect may vary over space and time. This dissertation used hyperspectral and thermal remote sensing imagery to derive key observations of urban physical and biophysical properties and model urban microclimates across the megacity of Los Angeles. In Chapter 1, I used Multiple Endmember Spectral Mixture Analysis (MESMA) to map sub-pixel fractions of different vegetation types, as well as other types of urban cover, at 4 m and 18 m resolution over Santa Barbara, California (Wetherley et al., 2017). Fractional estimates correlated with validation fractions at both scales (mean R^2 = 0.84 at 4 m and R^2 = 0.76 at 18 m), with accuracy affected by image spatial resolution, endmember spatial resolution, and class spectral (dis)similarity. Accuracy was improved by using endmembers measured at multiple spatial resolutions, likely because they incorporated additional spectral variability that occurred across spatial scales. In Chapter 2, I applied this methodology to derive sub-pixel cover for the greater Los Angeles metropolitan area (4,466 km^2) (Wetherley et al., 2018). Further improvement in quantifying sub-pixel vegetation types was achieved by modifying the MESMA shade parameter. Land

surface temperature (LST), derived from thermal imagery, was used to model temperature change along vegetation fractional gradients, with slopes of LST change showing significant differences between trees and turfgrass ($p < 0.001$). Expected per-pixel LST was derived from these gradients based on sub-pixel composition, and when compared to measured LST was found to deviate with a standard deviation of 3.5°C across the scene. These deviations were negatively related to irrigation and income, while building density was observed to affect tree LST more than it affected turfgrass LST. In Chapter 3, I used the map of Los Angeles landcover, along with data from LiDAR, GIS, and WRF climate variables, to parameterize an urban climate model (Surface Urban Energy and Water Balance Scheme: SUEWS) for 2,123 neighborhoods (each 1 km^2) across Los Angeles. Modeled latent fluxes were correlated with remote sensing LST ($R^2 = 0.39$) collected over a period of 5 hours, with an overall diurnal pattern modified by irrigation timing. Spatial variability across the study area was related to local landcover, with albedo and vegetation fraction strongly influencing latent and sensible fluxes. A strong regional climatic gradient was observed to affect latent fluxes based on coastal proximity. Overall, this dissertation quantifies the key drivers of urban vegetation function in a large city, and further demonstrates the potential of hyperspectral and thermal imagery for observing city scale surface and microclimate variability.

TABLE OF CONTENTS

LIST OF FIGURES

Introduction

More than half the world's population lives in cities, with urban populations increasing by an estimated 1.5 million people per week (PwC, 2014). Urban environments represent an extreme form of land cover modification that produces elevated urban heat and leaves urban populations increasingly vulnerable to illness, poor air quality, and strained resources (Akbari et al., 2001; IPCC Report, 2014; United Nations, 2015). Material, structural, and vegetation variability combine at a local scale to produce urban microclimates, which may either mitigate or exacerbate urban heating (Oke, 1987; Smith & Levermore, 2008; Livesley et al., 2016). In particular, vegetation modifies urban microclimates through evapotranspiration as well as local shading. Urban greening therefore underlies many municipal plans for climate management, such as the Los Angeles 'Million Trees LA' initiative (McPherson et al., 2011).

Vegetation transpiration represents a biological control on latent heat fluxes, and is sensitive to local surface conditions including local structure, materials, and plant type, as well as regional climate (Voogt & Oke, 1998; Grimmond & Oke, 1999; Arnfield, 2003; Peters et al., 2011; Stewart & Oke, 2012; Myint et al., 2013). These factors can combine in ways that produce contradictory results—for example, asphalt has been shown to both increase evapotranspiration by advection of warm air over well-watered vegetation, and decrease evapotranspiration by inducing stomatal closure (Oke, 1979; Oke, 1988; Kjelgren & Montague, 1998). These types of complex interactions make it difficult to scale up our knowledge of urban microclimate drivers to large-domain urban climate modeling, mitigation, or management.

Analyzing the interactive effects between urban vegetation and microclimates across large domains has remained a challenge because urban surface heterogeneity typically occurs at fine spatial scales relative to the resolution of many Earth observing satellites. For example, the recommended minimum pixel size for classifying an urban image is 5 m or smaller, while Landsat and the Advanced Spaceborne Thermal Emission and Reflection Radiometer (ASTER) have a coarser resolution of 30 m (Myint et al., 2013; Weng, 2012). For many non-urban ecosystems, remote sensing measurements of reflectance in the visible, near-infrared, and short wave infrared (VSWIR) at 30 m spatial resolution is adequate for quantifying surface variability and landcover change, however applications for urban remote sensing have been limited due to insufficient spatial resolution.

Growing interest in the use of remote sensing to study more functional aspects of ecosystems has led to the development of hyperspectral sensors, which measure tens or hundreds of very narrow bands across the electromagnetic spectrum. For example, the Airborne Visible Infrared Imaging Spectrometer (AVIRIS) measures 224 bands between 350 – 2500 nm, and can be used study ecosystem function by detecting subtle spectral variations that represent changes in plant chemistry, physiology, and structure (Ribeiro da Luz & Crowley, 2007). At fine spatial resolutions (~4 m), hyperspectral imagery has been found to improve classification of urban cover types and vegetation species, in part because it is better able to discriminate between spectrally similar landcover (Xiao et al., 2004; Herold & Roberts, 2005; Franke et al., 2009; Alonzo et al., 2013). However, in the near-future orbital hyperspectral sensors will collect imagery at 30 m spatial resolution or greater, necessitating methodologies for deriving sub-pixel cover (Settle & Drake, 1993; Roberts et al., 1998; Bateson et al., 2000; Stein, 2003; Somers et al., 2012; Goenaga et al., 2013; Zare & Ho,

2014). One unmixing method that is particularly well suited for urban scenes is Multiple Endmember Spectral Mixture Analysis (MESMA), because it allows the number and type of endmembers representing sub-pixel classes to vary per pixel (Roberts et al., 1998).

In urban areas, MESMA and other unmixing methods are often used to estimate generalized fractions of vegetation, impervious surfaces, and soil (Ridd, 1995; Wu, 2004). However, this does not discriminate between different plant types, such as turfgrass and tree, which each have distinct microclimate effects (Peters et al., 2011). Mapping these plant types separately would allow for analysis of their effects on local heat exchanges that differ due to albedo, water access, and shading. Therefore, there is a growing interest in the potential of hyperspectral imagery for expanding the categories of landcover that can be detected at sub-pixel scales (Roberts et al., 2012; Okujeni et al., 2015).

Another key biophysical measurement for assessing urban microclimates across a city is land surface temperature (LST). LST can be used to measure canopy temperatures, which affect many aspects of plant function such as transpiration, photosynthesis, and respiration (Leuzinger et al., 2010; Serbin et al., 2015). Because LST is derived from thermal imagery, and because thermal wavelengths have lower energy than wavelengths in the VSWIR, a larger pixel size is required. Typical thermal pixel resolutions for orbital imagers range from 90 m (ASTER) to 1 km (Moderate Resolution Imaging Spectroradiometer: MODIS). This has limited remote sensing assessment of urban thermal dynamics to relationships that can be observed at these coarser scales. For example, studies have used urban LST imagery to characterize the urban heat island, model urban sensible heat flux, and examine the links between urban cover and heat response (Weng & Quattrochi, 2006; Xu et al., 2008; Jiang & Tian, 2010; Wang et al., 2016). In this vein, several studies have

investigated how sub-pixel fractions of green vegetation and impervious surface relate to measured LST and vegetation indices such as the Normalized Difference Vegetation Index (NDVI) (e.g., Li et al, 2011; Deng & Wu, 2013). However, the coarse resolution of LST imagery has so far prevented city-scale assessment of urban canopy temperatures as a potential indicator of vegetation stress.

There are two other significant factors that limit remote sensing analyses of urban microclimates. First, the temporal resolution of remote sensing imagery is typically too coarse to observe diurnal change (e.g., Landsat repeat overpass is ~16 days). The exception to this is geostationary satellites, such as the Geostationary Operational Environmental Satellite (GOES-16); however, imagery is collected at very coarse spatial resolutions (0.5 – 2 km) and its analysis is further hindered by clouds. Second, there are several environmental variables that cannot be easily quantified remotely, including soil moisture and latent heat flux. For this reason, much of our understanding of urban fluxes comes from in situ and flux tower studies of urban evapotranspiration, energy budgets, vegetation stress, and microclimates (Voogt & Oke, 1998; Grimmond & Oke, 1999; Arnfield, 2003; Peters et al., 2011). However, direct-measurement methods are subject to locational biases that make their findings difficult to extrapolate beyond their study area (Grimmond et al., 2011; Luederitz et al., 2015). Urban energy balance models, which can be based on observed (in situ or flux tower) as well as known physical, chemical, or biological processes, offer a potential solution. By combining them with remote sensing data, urban fluxes can be evaluated at high temporal scales at the spatial resolution of remote sensing inputs.

The goal of my research is to contribute to a better understanding of urban microclimate variability across quantified urban surface heterogeneity, with a particular

emphasis on interactive effects with urban vegetation. In my dissertation, I focus on Los Angeles, California, the second largest city in the United States with a population that has grown from around 5 million in 1950 to over 18 million in 2012 (U.S. Census, 2012). Los Angeles experiences a Mediterranean climate, with warm dry summers and wet winters, and in the past decades has been subject to several severe droughts, including a state-wide megadrought from 2012-2015 (Griffin & Anchukaitis, 2014; Asner et al., 2016). Los Angeles offers a large urban extent over which a wide range of possible surface cover permutations and associated microclimates can be evaluated. I do this using a unique remote sensing dataset collected by the NASA Hyperspectral Infrared Imager (HyspIRI) airborne campaign over Los Angeles and the nearby city of Santa Barbara in the summer of 2014. This campaign collected airborne hyperspectral imagery coincident with thermal imagery, which I use to derive urban landcover and quantify associated thermal variability across the study area (Green et al., 1998; Hook et al., 2001). I augment this dataset using additional airborne imagery, field measurements, and GIS data to better characterize urban climate and vegetation variability.

In Chapter 1, I use hyperspectral AVIRIS imagery of Santa Barbara, California to quantify sub-pixel urban composition at fine (4 m) and coarse (18 m) spatial resolutions (Wetherley et al., 2017). I develop spectral libraries of single- and multiple-resolution endmembers, and use MESMA to estimate sub-pixel fractions of spectrally dissimilar materials (vegetation, impervious, pervious) as well as pairs of spectrally similar materials (turfgrass and tree, paved and roof, non-photosynthetic vegetation and soil) at both resolutions. The sub-pixel fractions are validated using 1 m orthophotography. I then

compare fractional maps produced at both resolutions to evaluate the scalability of fractional estimates of urban materials using hyperspectral imagery.

In Chapter 2, I conduct a large-scale analysis of urban surface composition and temperature variability across the Los Angeles metropolitan area (4,466 km^2). Sub-pixel fractions of two plant functional types (tree and turfgrass) and 4 urban materials (impervious surface, commercial roof, non-photosynthetic vegetation, and soil) are quantified using AVIRIS. Fractional cover gradients of plant types and non-vegetated materials are developed using 1.7 million pixels, from which I model LST changes using simultaneously collected thermal imagery (MODIS-ASTER Airborne Simulator: MASTER). Vegetation LST variability is mapped by subtracting modeled LST from observed LST and examining it relative to building density and vegetation management.

In Chapter 3, I model and assess urban flux variability for 2,123 continuous neighborhoods (each ~1 km^2) across Los Angeles. I use the Surface Urban Energy and Water Balance Scheme (SUEWS: Järvi et al., 2011), with localized parameters for urban surface materials, plant type, albedo, and structural variability extracted from a suite of remote sensing imagery (airborne hyperspectral and LiDAR). Additional GIS data, as well as climate variables from a high-resolution (3 km, hourly) WRF climate model, are used to further parameterize variability across the city (Skamarock & Klemp, 2008). Model outputs are assessed using MASTER LST imagery (36 m resolution), and diurnal flux variability investigated across gradients of urban surface cover and regional climate.

Chapter 1

Mapping Spectrally Similar Urban Materials at Sub-Pixel Scales

With Dar A. Roberts and Joseph P. McFadden.

Reproduced with permission from Remote Sensing of Environment:

Wetherley, E.B., Roberts, D.A., and McFadden, J.P. 2017. “Mapping Spectrally Similar Urban Materials at Sub-Pixel Scales.” Remote Sensing of Environment 195 (6): 170–183. doi: 10.1016/j.rse.2017.04.013.

1. Introduction

Accurately mapping urban composition is critical for understanding the urban environment, because the distribution of materials across an urban surface directly affects energy and water fluxes, which in turn impact urban climate, resource use, and human health (Jensen & Im, 2007; Powell & Roberts, 2008; Behling et al., 2015; Gu et al., 2015; Fu & Weng, 2016). Imaging spectrometry, which measures the reflected visible, near-infrared, and short wave infrared (VSWIR) range as contiguous, narrow bands, is capable of detecting spectral differences between urban materials that would otherwise appear spectrally similar in broadband imagery (Herold et al., 2004; Heiden et al., 2007; Ferrato & Forsythe, 2013). However, such imagery is rarely deployed for urban mapping, where fine spatial resolution (ideal for identifying object boundaries) is typically prioritized over fine spectral resolution (Small, 2001; Hodgson et al., 2003; Myint et al., 2013).

Highly accurate maps of urban vegetation and materials have been produced using imagery that has both a fine spatial and fine spectral resolution (Xiao et al., 2004; Herold et al., 2008; Franke et al., 2009; Alonzo et al., 2013). These data are measured by airborne imaging spectrometers, such as the Airborne Visible Infra-Red Imaging Spectrometer (AVIRIS), flying at low attitude. However, airborne data is expensive, manually intensive to process, and difficult to acquire for multiple urban areas or multiple time periods. An orbital imaging spectrometer would overcome many of these limitations, making it possible to measure and compare urban composition globally and track changes in urban composition over time. Currently, there are several planned orbital imaging spectrometer missions that would collect repeat, global imagery, including NASA's Hyperspectral Infrared Imager (HyspIRI), Germany's Environmental Mapping and Analysis Program (EnMAP), and Italy's

PRecursore IperSpettrale della Missione Applicativa (PRISMA) (Labate et al., 2009; Guanter et al., 2015; Lee et al., 2015).

Data imaged by these first-generation orbital spectrometers will have coarser spatial resolutions than typically used for fine-scale urban composition mapping. For example, HyspIRI and EnMAP will collect VSWIR measurements at 30 m resolution, similar to that of Landsat or ASTER (Lee et al., 2015). Orbital imaging spectrometry will still capture the full VSWIR range, however at this resolution urban spectra will likely be highly mixed and represent multiple materials per pixel (Small, 2001). This leaves open the possibility of extracting important global urban compositional information if we can first understand the effect of spatial resolution on urban composition estimates.

When pixels are too large to identify landscape features, sub-pixel composition must be estimated from measured signals. Methods for doing so primarily rely on linear spectral mixture analysis (SMA), which assumes that the measured reflected signal of a mixed-composition pixel is a linear combination of reflectance from all sub-pixel surfaces, proportional to their pixel fraction (Settle & Drake, 1993). In practice, scene materials are grouped into classes, which are then represented by a smaller number of representative spectra, known as spectral endmembers (EM). These can be extracted from the image itself (image EMs) or derived from field or laboratory measurements or simulated (reference EMs) (Somers et al., 2011). The collective group of EMs used to unmix an image is called a spectral library, and ideally captures the full spectral variability of materials present in the scene. For scenes that contain high levels of material diversity, identifying representative EMs can be particularly challenging (Roberts et al., 2012). For example, an urban impervious

class may include many spectrally unique water resistant materials such as asphalt, concrete, metal, rubber, etc. (Herold et al., 2004).

Methods have been developed to incorporate inter-class variability into SMA, broadening its ability to overcome challenges associated with spectrally diverse, coarse spatial resolution imagery. These methods include using bundles of EMs, local unmixing using EMs extracted from a moving window, and estimating fractions based on statistical distributions (Bateson et al., 2000; Stein, 2003; Somers et al., 2012; Goenaga et al., 2013; Zare & Ho, 2014). Multiple Endmember Spectral Mixture Analysis (MESMA) is another type of SMA that allows the number and type of EMs to change on a per-pixel basis, and has been shown to be robust enough to unmix highly variable urban landscapes using either broadband or high spectral resolution imagery (Roberts et al., 1998; Powell et al., 2007; Franke et al., 2009; Roberts et al., 2012; Wu et al., 2014).

As these techniques have enabled SMA to capture spectral variability across an urban scene, it continues to be primarily used to estimate sub-pixel fractions of broad cover classes. Many urban pixel-unmixing studies are modeled on the Vegetation-Impervious-Soil (VIS) scheme, which classifies all urban components as a mixture of these three surfaces, plus water (Ridd, 1995; Wu, 2004). However, this scheme lumps together surfaces that have very different effects on urban environmental function and ecosystem services. For example, trees and turfgrass both fall into the vegetation class, however they have very different water use and while trees shade nearby surfaces and may overhang impervious (e.g., a street tree) or pervious surfaces (e.g., in an urban park), turfgrass provides no shade and is more consistently pervious (Peters et al., 2011; Grimmond et al., 2011). Similarly, non-photosynthetic vegetation (NPV) is difficult to distinguish from soil in broadband imagery,

however these two surfaces could represent different levels of soil compaction (e.g., a field of dead vegetation versus a soil parking lot) and thus have different potential for erosion and perviousness. Recognizing this, studies have started to explore the potential of imaging spectrometry to perform SMA using narrower class definitions (Okujeni et al., 2013; Okujeni et al., 2015; Roberts et al., 2015).

As narrower class definitions expand the material fractions that SMA can map, other studies have begun to examine the effect of image spatial resolution on fractional estimate accuracy (Roberts et al., 2012; Okujeni et al., 2015). However this work has not yet been extended to examine the effects of spectral library spatial resolution. This is a critical question, because the spectral diversity of a material class is augmented by the spatial resolution of its measurement. In an urban area, this is largely related to object structural diversity. For example, the spectral signature of a leaf will be different from that of a full tree crown, where light is absorbed, reflected, and scattered throughout the canopy, while that of a roof will be impacted not only by the roofing material but also the shape of the roof tiles and slope of the roof relative to incoming solar radiation (Meister et al., 2000; Roberts et al., 2004; Ollinger, 2011). The spatial resolution at which a surface is measured will therefore determine the extent to which its structure affects the spectral signature. This creates an intrinsic link between an EM and its resolution, adding variability that may or may not be present in the image being analyzed.

This study used fine and coarse resolution imaging spectrometry, collected over the same area and at the same time of year, to expand upon recent research and better understand how the spatial resolution of spectral libraries and imagery affects the accuracy of fractional estimates in an urban scene. Specifically, we asked the following questions:

1. How does the spatial resolution of image EMs affect spectral library performance?

2. Is fractional cover information conserved as image resolution coarsens?

3. Can imaging spectrometry accurately estimate fractions of both VIS classes and VIS sub-classes?

We used two AVIRIS images acquired at resolutions considered typical for urban remote sensing (4 m) and coarse for urban classification (18 m) (Jensen & Cowan, 1999). We produced single- and multiple-resolution libraries using spectra from both images, and applied these libraries to both resolutions of imagery to test which produced more accurate fractional estimates and at which scales.

2. Methods

2.1 Study Site

This study used imagery of the Santa Barbara, California urban area, which includes the cities of Santa Barbara and Goleta as well as developed, unincorporated land between these cities (Fig. 1.1). Study area boundaries were determined by the overlap of study imagery (described in Section 2.2) with the urban area. The study area is situated between the southern base of the Santa Ynez Mountains and the south-facing California coast. Highway 101 bisects the study area, connecting the primary downtown center, commercial zones, and a mix of neighborhoods that include low-density development with high tree cover and areas with more compact housing. Additional land cover includes agriculture (orchards and tilled fields), tree-covered riparian corridors, unirrigated open space, and the Santa Barbara Airport.

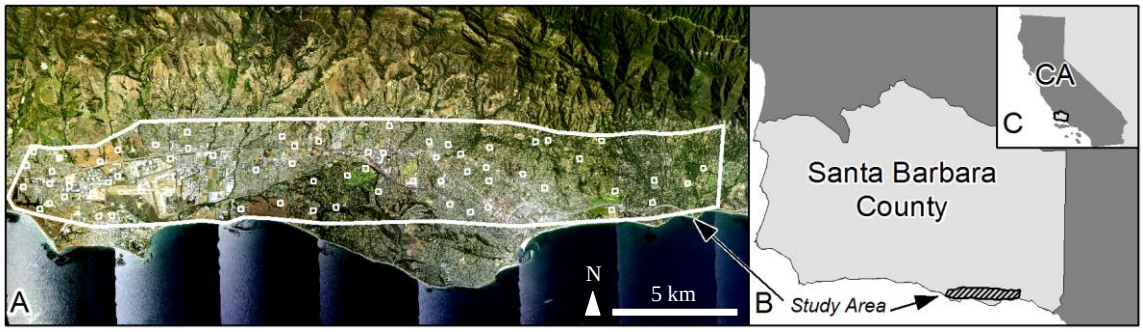

Figure 1.1. Study area location (A) in Santa Barbara County (B), California (C). The thick white line delineates the study area boundaries, while small white boxes indicate validation polygon locations.

Study area composition includes materials typical of North American cities as well as a few materials more common to the southwestern United States. Dominant built materials include asphalt, concrete, metal, wood and composite shingle roofs, gravel, brick, stone, and recreational surfaces such as tennis courts and artificial turf. Collectively, these materials are spectrally variable, with broadband albedos ranging from very low reflectivity (e.g., asphalt albedo of approximately 0.05) to moderately reflective (e.g., concrete albedo up to 0.35) to highly polished, specular surfaces such as glass or polished metal (Oke, 1987). A regionally specific material prevalent throughout the study area is red clay tile, found on residential and downtown commercial roofs. Vegetation is irrigated and maintained in developed areas, and includes irrigated turfgrass (defined here as any of a variety of grasses that are commonly grown to form turf in lawns, sport fields, etc.) as well as over 450 tree species, the majority of which are broadleaf evergreen (Alonzo et al., 2013). Urban vegetation is also spatially diverse, ranging from small residential lawns or isolated street trees to large golf courses and closed-canopy parks. Unmaintained vegetation, found in undeveloped areas, includes native and invasive grasses, shrubs, and riparian coast live oak forests. Due to the region's Mediterranean climate, with winter rain and dry summers, natural grasslands and deciduous

shrublands tend to vary seasonally between green vegetation (GV) and NPV, while irrigated urban vegetation remains more strongly GV throughout the year.

2.2 Data

Image data were collected at two spatial resolutions, allowing for a comparison of imagery dominated by pure pixels (< 5 m resolution) versus mixed pixels (> 5 m resolution). Fine resolution imagery (3.6 m) was collected by the AVIRIS-Next Generation (AVIRIS-NG) sensor on September 5, 2014. AVIRIS-NG samples 432 bands of radiance between 0.35 – 2.5 μm at continuous intervals of 5 nm (Hamlin et al., 2011). The sensor was flown aboard a Twin Otter platform at an altitude of 3.5 – 4 km, imaging two flightlines along an east-west axis between 20:56 UTC and 21:34 UTC. Coarse resolution imagery was collected by the AVIRIS-Classic (AVIRIS-C) sensor one week earlier on August 29, 2014. AVIRIS-C measures 224 contiguous bands of radiance between 0.38 – 2.5 μm with a full width half maximum of 10 nm and an instantaneous field of view of 1 milli-radian (Green et al., 1998). It was flown at a 35° northeast-southwest orientation aboard the NASA ER-2 high altitude platform as part of the HyspIRI Airborne Preparatory Campaign. Two flightlines with a ground instantaneous field of view of 15.6 m and 15.8 m were imaged between 18:05 UTC and 18:47 UTC.

Initial image processing was conducted by the Jet Propulsion Laboratory, and included calibrating each scene to radiance, converting it to reflectance, and spatially resampling the AVIRIS-C imagery to 18 m (Thompson et al., 2015). We used ENVI to spectrally resample the AVIRIS-NG imagery to AVIRIS-C wavelengths using a Gaussian model and full width half maximum equal to that of the AVIRIS-C imagery. Bands unusable

due to atmospheric interference were removed, with identical bands extracted from both images, leaving 178 bands for analysis. We corrected remaining locational errors with a basemap of mosaicked National Agriculture Imagery Program (NAIP) digital orthophotos (acquired in the spring and fall of 2014), resampled from its 1 m native resolution to 4 m and 18 m. We used Delaunay triangulation to georectify the AVIRIS-NG flightlines to the 4 m map with 165 and 185 ground control points, and the AVIRIS-C flightlines to the 18 m map with 79 and 110 ground control points. Delaunay triangulation is ideal for correcting airborne urban imagery because the variable terrain across each flightline cannot be corrected for by a single polynomial model, and it has therefore been used by other studies to correct locational errors with a high degree of accuracy (Alonzo et al., 2013; Frolking et al., 2013). The final average locational error was 0.68 pixels for AVIRIS-NG and 0.49 pixels for AVIRIS-C. We masked areas outside of the study area.

To confirm that both images were similarly calibrated, we conducted a simple test comparing histograms of normalized difference vegetation index (NDVI) values from the 4 m imagery, the 18 m imagery, and an additional image with the 4 m values spatially resampled to 18 m, using a procedure similar to that used by Song (2004) (Fig. 1.2). The 4 m histogram displays three prominent peaks, which correspond to pure pixels of impervious surface (NDVI = 0.06), NPV (NDVI = 0.23), and GV (NDVI = 0.81). The histograms of the resampled and the 18 m images display a single peak around NDVI = 0.23, and follow a similar curve. We took this as confirmation that 4 m and 18 m images were similarly calibrated and that no major changes had occurred in the study area in the week separating the two flights. This also confirmed our initial assumption that the 4 m imagery was dominated by pure pixels while the 18 m imagery contained more mixtures.

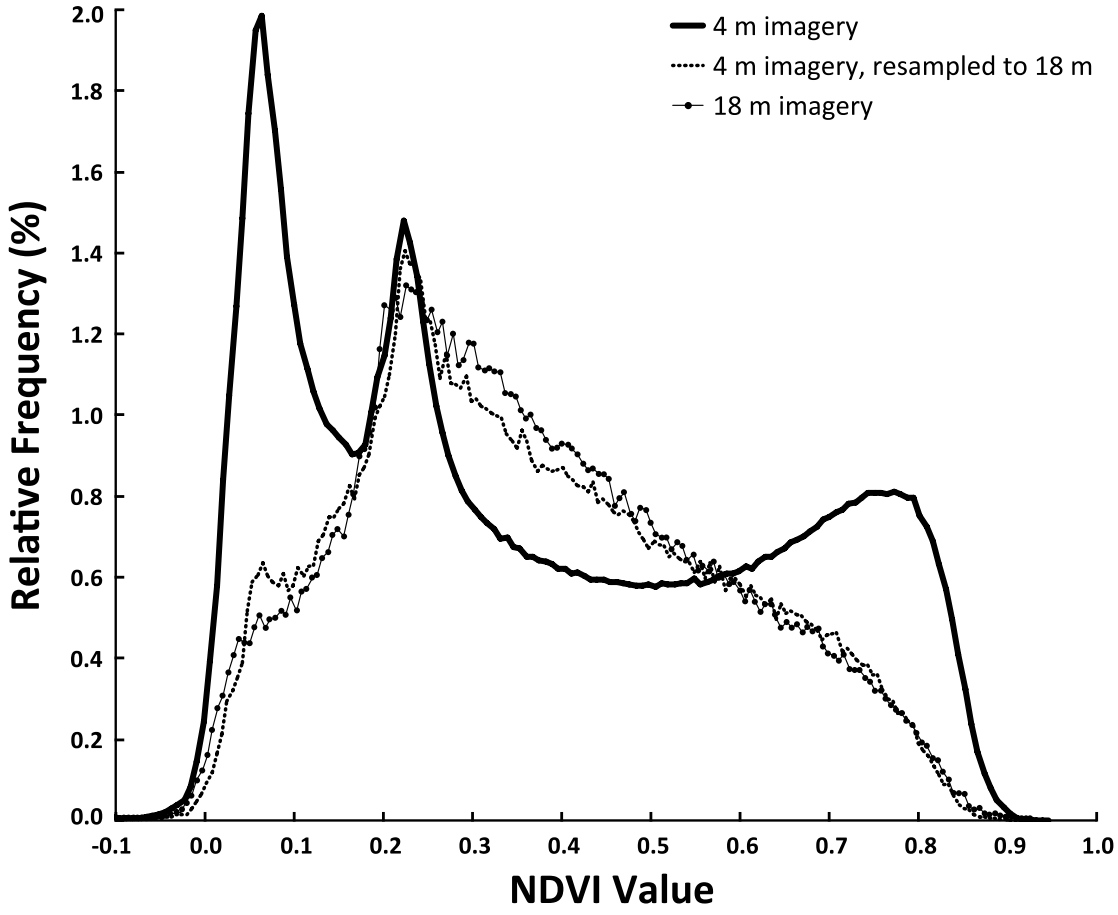

Figure 1.2. Comparison of NDVI value histograms for the 4 m image, the 4 m image resampled to 18 m, and the 18 m image.

2.3 Spectral Library Development

To assess the effect of spectral library spatial resolution, we created single- and multiple-resolution libraries using parallel techniques designed to maintain within-class spectral variability and class separability. We first extracted spectra from each image to build large reference libraries, and then reduced the spectra down to only optimal EMs. Figure 1.3 shows a flow chart of this process, which we describe in greater detail below.

We first manually identified urban materials in the 4 m scene, and then used polygons to extract "pure" spectra of these materials. To simplify this process, we extracted spectra from mosaicked 4 m flightlines, however other studies have extracted two sets of spectra with the same polygon if it was located where two images overlapped, capturing different sun-sensor geometries (e.g., Roberts et al., 2015). We produced 240 polygons across the 4 m imagery, extracting spectra from multiple roof types (commercial, shingle, metal, and red tile), asphalt, concrete, brick, trees, low shrubs, irrigated turfgrass, soil, NPV, as well as other less common urban materials including rubber, solar panels, artificial turf, clay tennis courts, and canvas and plastic tarps of various colors. We determined that these less common spectra represented impervious surfaces in the scene, so we included them in the broader impervious class and then categorized them as either ground or roof cover.

We next applied these polygons to the mosaicked 18 m scene. Polygon boundaries were adjusted or polygons deleted completely if they were found to contain a mixed surface (such as vehicles in a parking lot), did not conform to object boundaries at the 18 m scale, or were too small to encompass a full 18 m pixel. This was to avoid introducing spectrally mixed EMs into the library. In total, we removed 92 polygons, or 39.6% of the original 4 m polygons. When possible, we replaced them with new polygons encompassing the same cover type but at spatial scales resolvable at 18 m, resulting in 237 polygons.

While using identical polygons to extract spectra from the 4 m and 18 m scenes would have allowed for a more direct comparison of material spectra at different spatial resolutions, modifying our polygons enabled us to capture different scene-level spectral variability. All 6 classes were represented at both scales, however at 4 m we extracted spectra from targets smaller than those resolvable at 18 m, including individual tree crowns, roof

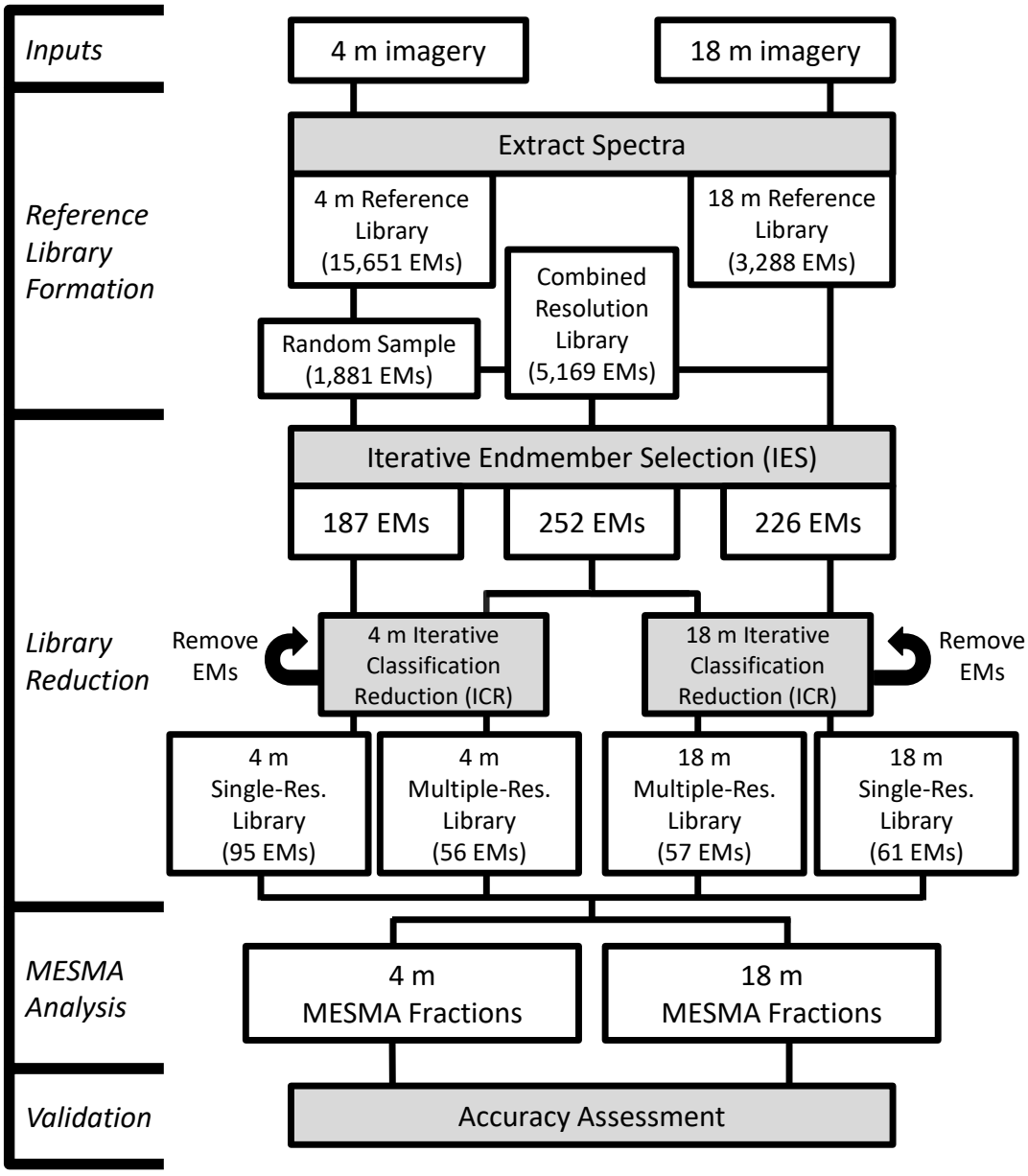

Figure 1.3. Flow chart of library development and image analysis (read from top to bottom).

types other than commercial roofs, and less common materials such as solar panels. Conversely, larger surfaces were represented in the 18 m library, including irrigated golf courses or large lawns, closed canopy trees, open space NPV, large commercial roofs, wide

highways, and empty parking lots. Consequently, the average polygon size on the 4 m imagery was 1,193.6 m^2, or 74.6 pixels, while the average polygon size on the 18 m imagery was 5,572.8 m^2, or 17.2 pixels.

We developed metadata for each individual spectrum describing multiple levels of land use and cover material detail. These included a broad pervious/impervious distinction, land use (parking lot, road, recreational field, etc.), and plant functional type. The final, most detailed category of metadata described both material and use (e.g., red tile roof or asphalt parking lot). Metadata were verified by viewing the surfaces using Google Earth imagery acquired in August, 2014, in addition to inspecting the spectral signatures. Knowledge of local spectra was derived in part from a field spectral library of Santa Barbara area urban spectra (Herold et al., 2004). We divided all spectra into spectrally dissimilar classes based on the VIS model: GV, Impervious, and non-GV Pervious. We then sub-divided each dissimilar class into pairs of spectrally similar VIS sub-classes: turfgrass and tree (GV), paved and roof (Impervious), and NPV and soil (non-GV Pervious). We conducted a Bhattacharyya distance analysis on the 18 m library, using all 178 bands, to confirm that spectrally similar class pairs were more similar to each other than to other classes. The Bhattacharyya distance measures spectral separability using the mean and covariance matrix of each class, and has been used to assess the spectral separability of classes using high-spectral resolution data (Kailath, 1967; Herold et al., 2004).

The initial sets of extracted spectra and metadata formed reference libraries. After excluding duplicate spectra, these included 3,288 unique 18 m EMs and 15,651 unique 4 m EMs. The 4 m reference library was significantly larger than the 18 m reference library because its finer spatial resolution yielded a greater number of pixels per polygon. This also

resulted in a high amount of spectral redundancy in the 4 m library. To reduce redundancy and produce a 4 m reference library more similar in size to the 18 m library, we used the procedure outlined in Roth et al. (2012) to produce 10 libraries of randomly sampled EMs from the 4 m library. EMs were randomly selected based on the finest level of metadata describing both use and material to maintain as much variability as possible with the minimum number of spectra. We restricted any polygon from contributing more than 50% of its spectra or 10 spectra total to any particular library, creating 10 libraries of 1,881 randomly selected EMs. Because the 18 m library was less redundant, with a smaller pixel to polygon ratio, and was more manageable at 3,288 spectra, we chose to prioritize conserving spectral variability and not run random sampling.

We achieved further library reduction using Iterative Endmember Selection (IES) (Schaaf et al., 2011). IES is an automated algorithm that selects spectra that are representative of the larger reference library. It does so by comparing all pairs of EMs and selecting those that result in the highest kappa value for classifying the entire reference library. Each time an EM is added to the smaller IES library, IES will test for further improvement by individually subtracting each selected EM and recalculating the kappa value. IES continues to iteratively add and subtract spectra until the reference library is optimally represented. We ran IES on all 10 randomly selected 4 m libraries and on the 18 m reference library. The 4 m libraries yielded a range of kappa values from 0.940 to 0.966 and contained between 161 and 187 EMs. We selected the library with the highest kappa and 187 EMs and discarded the other 9 random libraries. The 18 m IES library yielded a kappa of 0.941 and 226 EMs.

Ideally, the reduced set of EMs in the 4 m and 18 m IES libraries optimally captured the variability of each reference library. We next set out to maximize class separability using

an iterative classification-reduction (ICR) procedure similar to that used by Roberts et al. (2012). We used MESMA to classify each scene with its native resolution IES library (i.e., the 18 m IES library was used to classify the 18 m image and the 4 m IES library was used to classify the 4 m image), constraining MESMA to select only one EM per pixel. We classified pixels as turfgrass, tree, paved, roof, NPV, or soil, incorporating an additional shade factor to control for brightness differences between EMs and measured signals. We visually inspected the results to identify and remove EMs that tended to overmap (classify surfaces outside its class) or undermap (classify few surfaces within its class). ICR was repeated with the reduced library until removing EMs produced no discernable improvement. This refined our 4 m library to a final size of 95 EMs and our 18 m library to 61 EMs.

We produced two multiple-resolution libraries using the same procedure, starting with a combined reference library that contained the 18 m reference library (3,288 spectra) and the randomly selected 4 m library (1,881 spectra). IES yielded a kappa of 0.968 and reduced the library to 252 spectra. We used ICR on the 4 m and 18 m images separately, and because different EMs performed better or worse on each image, this parallel process produced two different reduced multiple-resolution libraries. The 4 m multiple-resolution library contained 56 EMs, while the 18 m multiple-resolution library contained 57 EMs.

In total, we produced four reduced libraries for comparison:

- 4 m single-resolution library: 4 m spectra.
- 18 m single-resolution library: 18 m spectra.
- 4 m multiple-resolution library: 4 m and 18 m spectra, iterated (ICR) on the 4 m image.
- 18 m multiple-resolution library: 4 m and 18 m spectra, iterated (ICR) on the 18 m image.

2.4 MESMA Analysis and Accuracy Assessment

We used MESMA to apply each library to the 4 m and 18 m imagery and estimate sub-pixel classes and their fractions. MESMA selects the best fitting model based on maximum and threshold RMSE values. We used values obtained from the literature of 2.5% and 0.7%, respectively, meaning any pixel that could not be modeled with an RMSE below 2.5% reflectance would remain unclassified, and a more complex model (more per-pixel EMs) would be used only if doing so improved the RMSE by at least 0.7% (Roberts et al., 2012). Fractions were constrained between 0 and 1, no pixel could contain more than 80% shade, and overall pixel complexity (the number of EMs per pixel) was limited to a maximum of three, plus shade. While more complex models almost always perform better than simple models in terms of RMSE, greater model complexity has also been positively correlated with computation time and negatively correlated with accuracy, and therefore urban unmixing studies tend to limit complexity to three or fewer EMs (Powell et al., 2007). Finally, MESMA restricts the overall EM combination to one class representative per pixel, e.g., it will not evaluate a possible mixture of two roof EMs or two tree EMs. However, when calculating fractions of spectrally similar classes, MESMA did evaluate mixtures of impervious (paved and roof), mixtures of GV (turfgrass and tree), and mixtures of pervious (NPV and soil). Within these constraints, MESMA evaluated all possible EM combinations pixel by pixel to select the best fitting model. We initially produced fractional estimates on unwarped imagery, which we then shade normalized, rotated, warped, mosaicked, and clipped to the study area.

We developed 59 validation polygons to assess the accuracy of our MESMA products, illustrated in Fig. 1.1a. Each polygon was 180 x 180 m in size, representing a 10 x

10-pixel area on the 18 m imagery or a 45 x 45 pixel area on the 4 m imagery. While larger validation polygon sizes tend to produce higher measures of fractional accuracy, 180 x 180 m polygons contained a desirable fractional mix of all or most of the 6 classes of interest, while smaller polygons contained inadequate combinations of fractional cover (Powell et al., 2007). We used the pixel grid of the 18 m imagery to randomly generate polygon locations, setting a minimum inter-polygon distance of 400 m to evenly distribute them across the study area. Within each validation polygon, we used E-Cognition to classify the 1 m NAIP imagery into turfgrass, tree, paved, roof, NPV, and soil cover. NAIP classification accuracy was visually assessed and manually corrected based on a comparison to August 2014 Google Earth imagery. This was particularly important for adjusting turfgrass surfaces that had senesced to NPV by the time of the flights. We also discarded two polygons. One contained 40% open water, which we did not include as an urban cover class due to the lack of any significant urban waterways in the study area. The other was a row crop agricultural field for which we could not determine (from validation imagery) its cover at the time of the AVIRIS flights. We replaced these with two additional randomly generated polygons. Once all polygons were classified, we evaluated the range of class cover fractions and determined that soil was inadequately represented, with no polygons exceeding 18% soil cover. This limited soil coverage is an accurate reflection of the absence of soil in our scene, however we decided to augment our validation dataset to better assess our ability to detect soil. We added five polygons representing larger soil percentages, bringing our total number of validation polygons to 64.

We used validation polygon boundaries to extract the total fractional coverage of dissimilar VIS classes (GV, Impervious, non-GV Pervious) and similar VIS sub-classes

(turfgrass, tree, paved, roof, NPV, soil) from all MESMA products. We plotted MESMA fractions (y) against validation fractions (x) to calculate the linear R^2, slope, and intercept for each class.

2.5 Synthetic Mixtures

While polygon-level validation is a common method for assessing fractional estimates, it provides no information regarding accuracy at the pixel level (Roberts et al., 2012; Okujeni et al., 2015). To better understand this, we produced a set of synthetic mixtures using spectra that had been excluded from our 4 m library during random sampling, and then unmixed them using MESMA and the 4 m multiple-resolution library. To produce the synthetic mixtures, we calculated the median broadband brightness value for each class, randomly selected 20 spectra with brightness values below and above this value, and then averaged together each group of 20 spectra. This produced one bright and one dark generalized spectrum of turfgrass, tree, paved, roof, NPV, and soil, for a total of 12 spectra. Because the paved and roof classes had a greater level of material diversity, thus greater spectral variability, we selected spectra from smaller sub-groups of each. For the paved class we produced an averaged asphalt spectrum (dark) and an averaged concrete spectrum (bright), while the roof class was limited to dark and bright commercial roof spectra only. We synthesized linear mixtures of every possible two-class combination using these spectra, varying fractions by 1%, for a total of 6,048 mixtures, and then unmixed them, limiting the number of EMs to a maximum of two (plus shade) but leaving all other constraints identical to those used in our image analysis.

3. Results

3.1 Producing single- and multiple-resolution libraries

We produced a set of comparable single- and multiple-resolution spectral libraries to investigate the effect of EM spatial resolution on fractional estimates. Because a small library is preferable when using MESMA, we combined a variety of automated and manual techniques to reduce the size of larger reference libraries while conserving class variability and separability as much as possible.

The 4 m single-resolution reference library was the largest in the study, containing 15,651 (non-duplicate) spectra extracted from 240 polygons. Because many of these spectra were redundant, we used random sampling to remove nearly 90% of the EMs and cut the library to 1,881 spectra. IES, which also provided a method for evaluating each randomly selected library through its kappa coefficient, reduced the library by another 90% to 188 spectra. ICR required 5 passes to reduce the library to 95 EMs, including 5 turfgrass, 45 tree, 17 paved, 16 roof, 7 NPV, and 5 soil spectra. Final turfgrass spectra were derived from large, well-irrigated areas, while tree spectra represented both open and closed canopies. Trees were also the largest class because additional bright tree spectra were needed to separate well-illuminated tree fractions from turfgrass. Library reduction, particularly ICR, stripped much of the material variability from the paved class, with the reduced library containing primarily asphalt of various brightnesses, while roof spectra included white and grey commercial roofs and red tile roofs. NPV spectra were drawn from unmaintained open space, while soil came from a variety of sites, including a racetrack, construction zone, and baseball diamond.

The 18 m single-resolution reference library did not require random selection. Together, IES and ICR reduced it from 3,288 spectra to 61 spectra, including 10 turfgrass, 11

tree, 6 paved, 17 roof, 14 NPV, and 3 soil spectra. Turfgrass, paved, and NPV spectra were drawn from similar targets as the 4 m library, while the coarser spatial resolution limited roof spectra to commercial roofs, tree spectra to closed canopy areas, and soil spectra to large targets including a beach and two bare agricultural fields.

We produced the two multiple-resolution reference libraries using an identical technique, beginning with the 1,881 randomly-selected 4 m spectra and 3,288 18 m spectra, for a combined library of 5,169 spectra. IES reduced this library to 248 EMs, consisting of a nearly equal number of 4 m (125) and 18 m (123) spectra. All 6 classes in the multiple-resolution IES library were represented by EMs from both spatial resolutions, with the majority of EMs for tree, roof, and soil classes represented by 4 m spectra and the majority of EMs for turfgrass, paved, and NPV represented by 18 m spectra. The balance between 4 m and 18 m spectra in the final multiple-resolution libraries depended on the scene each was iterated upon during ICR, with native resolution spectra being conserved over non-native spectra at a 2:1 ratio — the 4 m multiple-resolution library was 60.1% 4 m and 39.9% 18 m spectra, while the 18 m multiple-resolution library was 63.0% 18 m and 37.0% 4 m spectra. The two final multiple-resolution libraries shared 46% of their spectra (16 EMs from the 18 m image and 10 EMs from the 4 m image) while the remaining 54% of each library were unique.

As expected, classes with greater material diversity were represented by more spectrally variable EMs (Fig. 1.4). The most variable class was roof, with an average standard deviation (SD_{AV}) across all wavelengths of 0.123, followed by the paved class (SD_{AV} = 0.089). Soil (SD_{AV} = 0.052) and NPV (SD_{AV} = 0.057) had similar levels of variability. Turfgrass was the least variable, with SD_{AV} = 0.039, followed by tree (SD_{AV} = 0.042). These

libraries do not represent the full material diversity present in the imagery. EMs representing less common materials, such as artificial turf, rubber, brick, and solar panels, tended to be conserved through IES, but performed poorly during ICR by either over-representing their coverage (e.g., a solar panel EM modeling shaded or otherwise dark surfaces), or identifying so few pixels as to make their inclusion too computationally costly for the MESMA process. Had the goal of this study been to produce a classification map, and not fractional estimates, these unique EMs would likely have remained in the library.

3.2 Fractional Estimates

We applied each single-resolution and multiple-resolution library to the 4 m and 18 m scenes to produce eight maps of sub-pixel fractional estimates. We assessed accuracy for two groups of classes: spectrally dissimilar VIS classes of GV, Impervious, and non-GV Pervious, and spectrally similar VIS sub-classes of turfgrass and tree (GV), paved and roof (Impervious), and NPV and soil (non-GV Pervious). Multivariate analysis of variance (MANOVA) revealed a significant effect of library resolution (single- or multiple-resolution library; $p < 0.01$, $n = 72$), image resolution (4 m or 18 m; $p < 0.05$, $n = 72$), and spectral (dis)similarity ($p < 0.001$, $n = 72$) on polygon-level accuracy as measured by R^2 (Table 1).

3.2.1 Library Resolution

In nearly all cases, multiple-resolution libraries of 4 m and 18 m spectra produced more accurate fractional estimates compared to single-resolution libraries. Multiple-resolution libraries estimated fractions of spectrally dissimilar classes with average $R^2 = 0.91$, while single-resolution libraries estimated fractions of dissimilar classes with $R^2 = 0.82$. On

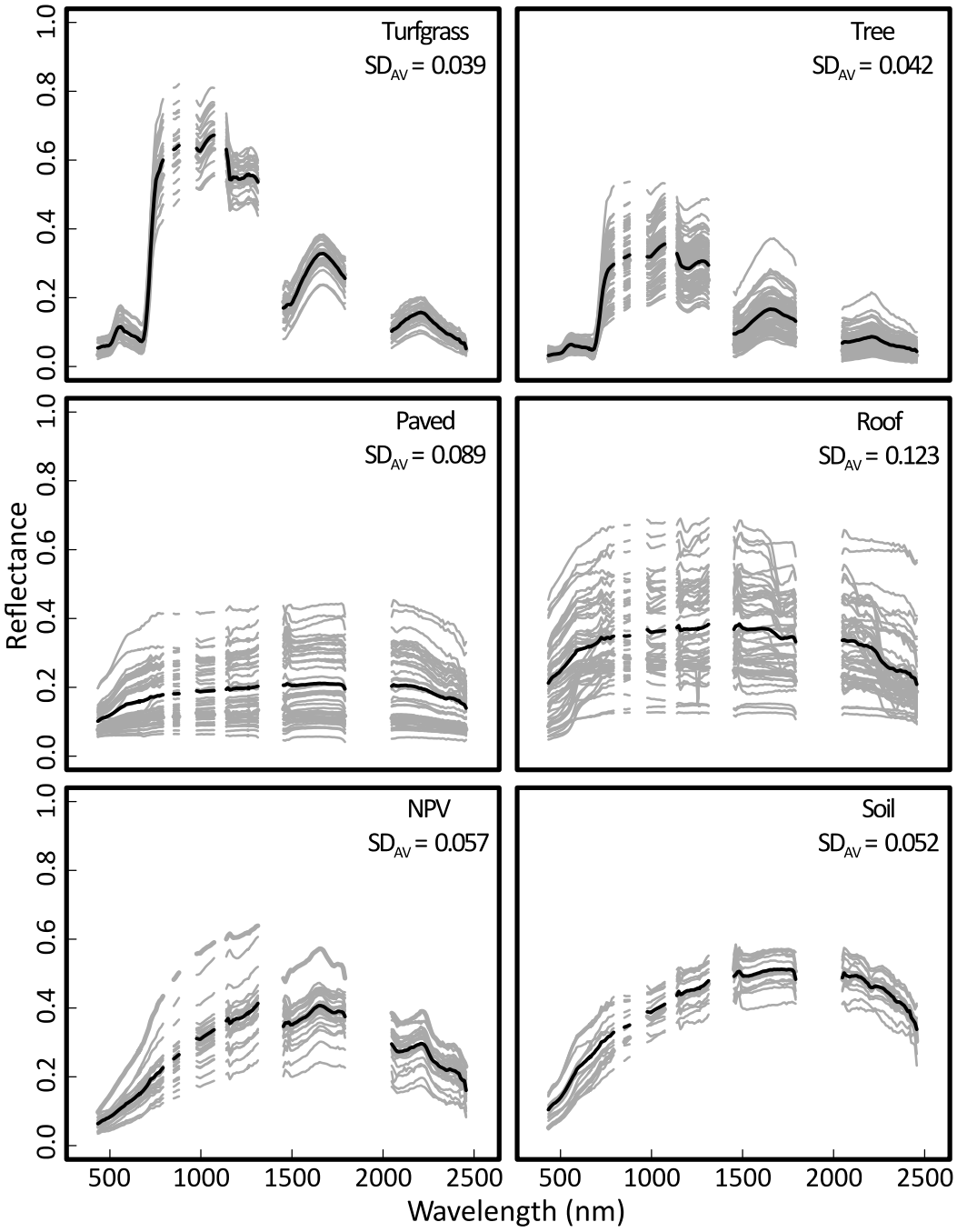

Figure 1.4. Spectra from all final libraries. Grey lines indicate spectra used to model turfgrass, tree, paved, roof, NPV, and soil fractions. The thick black line represents the average spectrum for each class. Reflectance standard deviation was calculated at each wavelength and then averaged together to produce a class average standard deviation (SD_{AV}).

Table 1. R^2 values for all library-imagery combinations for dissimilar and similar classes. Highlighted values indicate $R^2 > 0.80$.

		R^2							
		4 m Imagery				18 m Imagery			
		4 m Library		18 m Library		4 m Library		18 m Library	
		Single-Res.	Multiple-Res.	Single-Res.	Multiple-Res.	Single-Res.	Multiple-Res.	Single-Res.	Multiple-Res.
Dissimilar	*GV*	**0.954**	**0.954**	**0.925**	**0.938**	**0.907**	**0.916**	**0.930**	**0.927**
	Impervious	**0.940**	**0.923**	**0.868**	**0.921**	0.716	**0.909**	**0.844**	**0.879**
	Pervious	**0.873**	**0.922**	**0.828**	**0.885**	0.243	**0.873**	**0.827**	**0.872**
	Mean	**0.923**	**0.933**	**0.874**	**0.915**	0.622	**0.900**	**0.867**	**0.893**
Similar	*Turfgrass*	0.776	**0.832**	0.342	**0.804**	0.304	0.785	0.658	0.792
	Tree	**0.926**	**0.924**	**0.925**	**0.867**	0.724	**0.855**	**0.856**	**0.853**
	Paved	**0.864**	**0.885**	0.671	0.797	0.142	0.694	0.566	0.709
	Roof	0.612	0.635	0.216	0.356	0.345	0.475	0.221	0.508
	NPV	0.748	**0.837**	0.788	**0.819**	0.308	**0.801**	0.784	**0.815**
	Soil	**0.938**	**0.910**	0.704	**0.879**	0.167	**0.902**	0.769	**0.886**
	Mean	**0.811**	**0.837**	0.608	0.754	0.332	0.752	0.642	0.760

average, fractions of spectrally similar classes were also more accurately estimated using multiple-resolution libraries ($R^2 = 0.78$) compared to single-resolution libraries ($R^2 = 0.60$). Multiple-resolution libraries outperformed single-resolution libraries on both resolutions of imagery, with a more pronounced effect at 18 m where they improved average R^2 values forfractions of spectrally dissimilar classes by 0.15 and similar classes by 0.27. At 4 m the effect was less pronounced, improving fractional accuracy for dissimilar classes by 0.03 and similar classes by 0.09. As expected, multiple-resolution libraries were more portable across scenes compared to single-resolution libraries: on the 4 m image, the 18 m multiple-resolution library outperformed the 18 m single-resolution library, and on the 18 m image the 4 m multiple-resolution library outperformed the 4 m single-resolution library. However, multiple-resolution libraries also slightly out-performed single-resolution libraries on their

native resolution scenes, improving mean R^2 by 0.01 and 0.03 at 4 m, and 0.03 and 0.12 at 18 m, for dissimilar and similar fractions, respectively.

3.2.2 Image Resolution

Fractional estimates at 4 m showed better correlation with validation fractions compared to fractional estimates at 18 m. The mean fractional accuracy for the 4 m image was $R^2 = 0.91$ for spectrally dissimilar classes and $R^2 = 0.75$ for similar classes. Mean fractional accuracy for the 18 m image was $R^2 = 0.82$ for dissimilar classes and $R^2 = 0.62$ for similar classes. One factor contributing to the underperformance of the 18 m image was the low accuracy of the fractional estimates produced by the 4 m single-resolution library. On the 18 m image, this library produced mean fractional accuracies of $R^2 = 0.62$ for dissimilar classes and $R^2 = 0.33$ for similar classes. Examination of the MESMA product revealed significant BRDF effects resulting in confusion between classes. Investigation of the remaining 18 m MESMA products showed slight BRDF effects, but these were less affected overall. Excluding this BRDF-affected library increased mean fractional accuracies for the 18 m image to $R^2 = 0.89$ for spectrally dissimilar classes and $R^2 = 0.72$ for similar classes, which were more like the average accuracies obtained on the 4 m image.

Image resolution appears to be the primary driver of pixel complexity (Table 2). We allowed MESMA to select up to three EMs per pixel for both resolutions of imagery, however the 4 m fraction maps had fewer mixed pixels compared to the 18 m maps. Across all fraction maps, the majority of 4 m pixels (50.3% - 54.0%) were modeled by a single EM, while the majority of 18 m pixels (57.5% - 66.8%) were modeled by two EMs. Mean pixel complexity in the 4 m scene ranged between 1.51 to 1.66 EMs per pixel, while it ranged

between 1.81 to 1.88 EMs per pixel at 18 m. Both scene resolutions had the smallest proportion of pixels modeled by three EMs.

Table 2. Pixel complexity, ordered by mean complexity (average number of EMs per pixel).

	Scene	Pixel Complexity			
Library	**Resolution**	**Mean**	**% 1 EM**	**% 2 EM**	**% 3 EM**
4 m Multiple-Res.	18	1.88	25.14%	61.77%	13.07%
18 m Multiple-Res.	18	1.85	28.59%	57.53%	13.87%
18 m Single-Res.	18	1.84	22.33%	66.79%	10.83%
4 m Single-Res.	18	1.81	26.73%	65.27%	8.00%
4 m Single-Res.	4	1.66	50.29%	33.27%	16.44%
4 m Multiple-Res.	4	1.65	51.97%	31.35%	16.68%
18 m Multiple-Res.	4	1.64	53.52%	28.70%	17.78%
18 m Single-Res.	4	1.51	53.95%	40.61%	5.44%

3.2.3 Spectral (Dis)similarity

As expected, fractions of spectrally dissimilar VIS classes (GV, Impervious, and non-GV Pervious) had higher correlation to validation polygons than fractions of spectrally similar VIS sub-classes (turfgrass, tree, paved, roof, NPV, and soil). With the exception of the 4 m single-resolution library applied to the 18 m scene, which was highly affected by the BRDF, fractions of all dissimilar classes were estimated with $R^2 > 0.83$ while the estimated accuracy of spectrally similar fractions ranged between $0.22 < R^2 < 0.94$. GV fractions were the most accurately estimated, with average $R^2 = 0.93$ and all libraries detecting GV with $R^2 > 0.90$. Impervious fractions were the second most accurately estimated (average $R^2 = 0.88$), followed by non-GV Pervious (average $R^2 = 0.79$). Fractions of spectrally similar classes as a whole were less correlated with validation data, however certain spectrally similar classes proved easier to detect at sub-pixel levels than others. Tree fractions were estimated across all

libraries with average $R^2 = 0.87$, followed by soil ($R^2 = 0.77$) and NPV ($R^2 = 0.74$). Paved ($R^2 = 0.67$) and turfgrass ($R^2 = 0.66$) fractions were estimated with similar accuracies, while roof fractions were poorly estimated ($R^2 = 0.42$).

Bhattacharyya distance analysis conducted on the 18 m reference library, examining the spectral separability between each class using the mean class vector and covariance matrix, indicated that the most distinct pairs of spectra were those that included one GV EM (Fig. 1.5). Pairs with above average separability were turfgrass-soil, tree-soil, turfgrass-paved, turfgrass-roof, and tree-roof. As expected, the three spectrally similar pairs (turfgrass-tree, paved-roof, and NPV-soil) were the least distinct from each other, followed by tree-NPV and tree-paved.

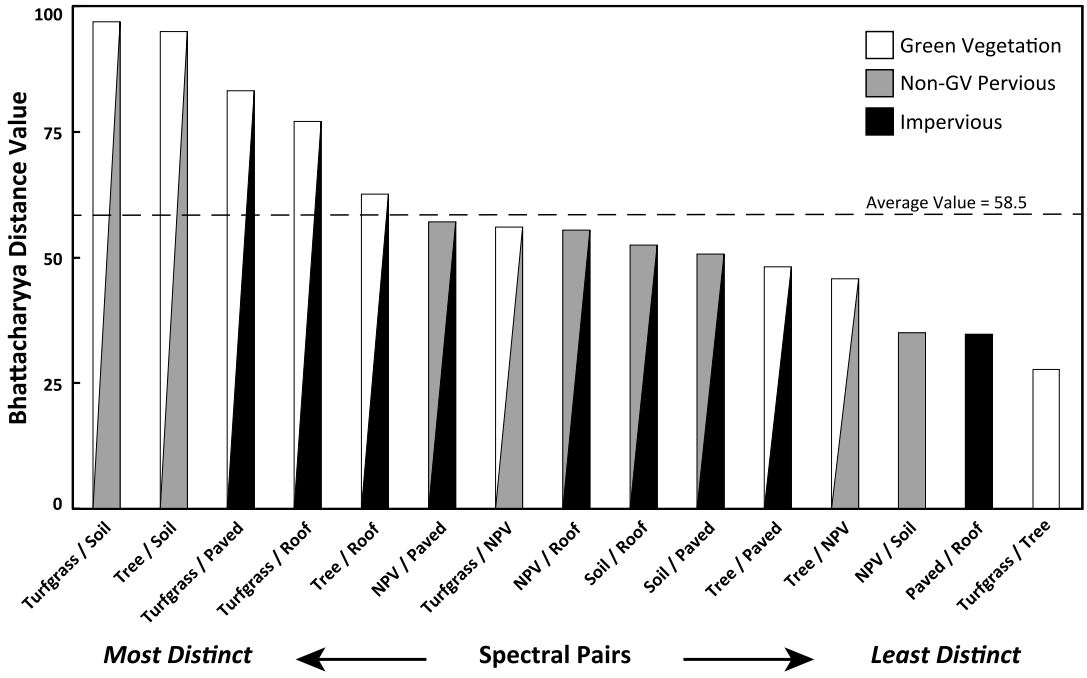

Figure 1.5. Bhattacharyya distance values for all class pairs. A larger value indicates the class pair is more spectrally distinct, and therefore more separable. The dashed line indicates the average distance value.

In general, fractions underestimated overall abundance as represented by slope values (where slope = 1 is a perfect model of abundances) (Table 3). While image resolution was found to not be significant ($p > 0.1$, $n = 72$), MANOVA found significant effects of library resolution (single- or multiple-resolution) and spectral (dis)similarity on slope values ($p < 0.05$, $n = 72$). Multiple-resolution libraries estimated material abundances better than single-resolution libraries for both dissimilar and similar class types: average multiple-resolution library slopes were 0.89 for dissimilar and 0.76 for similar classes, compared to average single-resolution library slopes of 0.80 for dissimilar and 0.65 for similar classes. Across all libraries, abundances of dissimilar classes were more accurately captured (with an average slope of 0.84) than similar class abundances (with an average slope of 0.71).

Table 3. Slope values for all library-imagery combinations for dissimilar and similar classes. Highlighted values indicate slope > 0.80.

		Slope							
		4 m Imagery				18 m Imagery			
		4 m Library		18 m Library		4 m Library		18 m Library	
		Single-Res.	Multiple-Res.	Single-Res.	Multiple-Res.	Single-Res.	Multiple-Res.	Single-Res.	Multiple-Res.
Dissimilar	*GV*	**0.979**	**0.973**	**0.861**	**0.982**	**1.063**	**1.018**	**1.067**	**1.096**
	Impervious	**0.849**	**0.886**	0.674	**0.825**	0.772	**0.919**	**0.879**	**0.930**
	Pervious	0.687	0.717	0.662	0.730	0.312	**0.807**	0.765	**0.812**
	Mean	**0.838**	**0.859**	0.733	**0.846**	0.716	**0.915**	**0.904**	**0.946**
Similar	*Turfgrass*	**0.815**	0.692	0.475	0.582	0.759	**0.927**	**0.906**	**0.950**
	Tree	**0.931**	**0.935**	**0.814**	**0.897**	**0.822**	**0.943**	**0.978**	**0.961**
	Paved	**0.867**	**0.843**	0.481	**0.831**	0.140	0.579	0.763	0.694
	Roof	0.455	0.542	0.418	0.279	**1.086**	**0.920**	0.435	**0.853**
	NPV	0.608	0.724	0.735	0.703	0.423	**0.825**	**0.846**	**0.863**
	Soil	0.749	0.606	0.562	0.762	0.123	0.656	0.476	0.662
	Mean	0.738	0.724	0.581	0.676	0.559	**0.808**	0.734	**0.830**

Intercept values indicate most models had a slight positive bias, but bias overall was relatively minor (Table 4). Of all library/image pairs, 82% had a positive or negative bias of less than 5%, while the remainder had a positive bias between 5-14%. Paved, roof, and soil classes exhibited positive errors across each library and image pair, while NPV skewed negative for three out of the four 18 m scenes.

Table 4. Intercept values for all library-imagery combinations. Highlighted values indicate an intercept of 5% or less.

	Intercept							
	4 m Imagery				18 m Imagery			
	4 m Library		18 m Library		4 m Library		18 m Library	
	Single-Res.	Multiple-Res.	Single-Res.	Multiple-Res.	Single-Res.	Multiple-Res.	Single-Res.	Multiple-Res.
GV	**0.023**	**0.023**	**0.035**	**0.041**	**-0.012**	**0.032**	**0.024**	**0.022**
Impervious	**0.013**	**0.014**	**0.003**	**0.005**	**0.040**	**0.024**	**-0.003**	**0.007**
Pervious	0.053	**0.026**	0.145	**0.043**	0.077	**-0.004**	**0.034**	**-0.006**
Turfgrass	**0.002**	**-0.002**	0.080	**0.016**	0.127	**0.015**	**0.028**	**0.015**
Tree	**0.046**	0.053	**-0.008**	0.075	**-0.048**	**0.046**	**0.033**	0.059
Paved	**0.037**	**0.032**	**0.019**	0.056	**0.033**	**0.035**	**0.046**	0.051
Roof	**0.025**	**0.041**	0.067	**0.023**	0.120	0.073	**0.041**	**0.026**
NPV	**0.041**	**0.011**	**0.013**	**-0.019**	**0.038**	**-0.012**	**0.000**	**-0.033**
Soil	**0.023**	**0.023**	0.130	0.066	**0.034**	**0.015**	**0.041**	**0.029**

To better understand how spectral similarity affected fraction estimates at the pixel level, we unmixed 6,048 synthetic mixtures using the 4 m multiple-resolution library (Table 5). Of the three spectrally similar class pairs, the easiest to distinguish from each other was NPV and soil: in mixtures of the two, fractional NPV was mapped with $R^2 = 0.90$ and soil with $R^2 = 0.87$, although NPV fractions tended to be slightly overestimated in these mixtures. Soil fractions were the most accurately mapped among all classes, with average $R^2 = 0.90$ across all substrates, however when soil was the substrate the average fractional accuracy for

all non-soil classes was the lowest, at $R^2 = 0.75$. Turfgrass and tree classes were the next most separable pair. In mixtures of the two, turfgrass fractions were estimated with $R^2 = 0.72$ and tree with $R^2 = 0.73$. When turfgrass represented less than 50% of this mixture it tended to be overestimated, and at fractions greater than 50% tended to be estimated as 100% of the mixture. When either turfgrass or tree were a substrate material, the fractional accuracies for all other classes were among the highest, with average $R^2 = 0.85$. The most confused spectrally similar classes were roof and paved, with roof fractions mapped with an accuracy of $R^2 = 0.37$ when mixed with paved, and paved fractions mapped with an accuracy of $R^2 = 0.29$ when mixed with roof.

Table 5. Fractional accuracy (R^2) for simulated class and substrate material mixtures.

		R^2						
		Substrate						
		Turfgrass	*Tree*	*Paved*	*Roof*	*NPV*	*Soil*	**Mean**
Measured Class	*Turfgrass*	NA	0.724	0.942	0.923	0.841	0.947	**0.875**
	Tree	0.733	NA	0.875	0.915	0.696	0.896	**0.823**
	Paved	0.930	0.894	NA	0.288	0.825	0.538	**0.695**
	Roof	0.874	0.773	0.374	NA	0.672	0.480	**0.634**
	NPV	0.842	0.793	0.904	0.917	NA	0.899	**0.871**
	Soil	0.980	0.976	0.801	0.874	0.874	NA	**0.901**
	Mean	**0.872**	**0.832**	**0.779**	**0.783**	**0.781**	**0.752**	

With synthetic mixtures of both bright and dark spectra, we could observe the effects of material brightness on fractional estimates. Bright spectra fractions and abundances tended to be more accurately characterized compared to dark spectra. When mixed with a dark substrate, bright spectra fractions were estimated with average $R^2 = 0.91$ and a mean slope of 1.11. When mixed with a bright substrate, bright spectra fractions were estimated with less

accuracy (R^2 = 0.85), but were more representative of abundances overall (slope = 0.99). Dark spectra abundances were overestimated, with mean slopes of 1.14 when mixed with a dark substrate and 1.04 when mixed with a bright substrate. Dark spectra fractions were also slightly less accurate, with R^2 = 0.84 when mixed with a bright substrate and R^2 = 0.83 when mixed with a dark substrate.

4. Discussion

In this study, we examined the effect of spatial resolution on fractional estimates when using imaging spectrometry, focusing on both the resolution of the spectral libraries as well as the imagery being analyzed. We did this in the context of an expanded VIS model, where we estimated fractions for six urban cover classes.

4.1 The Effect of Library Spatial Resolution on Fractional Estimates

This study represents the first comparative evaluation of multiple-resolution libraries. We found that multiple-resolution libraries performed significantly better than single-resolution libraries, even when compared to fractions produced using native image EMs. Native image EMs are often considered advantageous because they are at the same spatial scale as the original image and contain the same systematic image errors (Plaza et al., 2004; Myint & Okin, 2009). However, in this study, we found that 4 m and 18 m multiple-resolution libraries produced more accurate fractions than 4 m and 18 m single-resolution libraries, respectively, on their native imagery. This effect was more pronounced for the 18 m imagery, where incorporating 4 m EMs increased overall mean R^2 by 0.09.

The improved performance of multiple-resolution libraries is likely because they contain greater levels of material, structural, and sensor-level variability than single-resolution libraries. Materially, 4 m EMs were more variable and supplied spectra such as residential and red tile roofs, open canopy trees, and residential lawns. These were not resolvable as pure pixels at 18 m, but covered large areas of the scene. Combining fine and coarse resolution spectra also increased structurally-related spectral variance. Using the example of a tree crown, a 4 m pixel can measure spectral characteristics related to species, health, stress, and local illumination. Conversely, a tree spectra collected at 18 m likely represents a mixed signal of multiple crowns in a closed canopy, which mutes individual spectral differences and local variability. Combined in one library, these EMs capture a greater range of specific and generalized spectral representation that may better approximate variable mixture levels across a scene. Finally, combining EMs from multiple scenes incorporates sensor-level variability, such as different sun-sensor angles. Our analysis of NDVI (Fig. 1.2) showed the two images to be similarly calibrated, however the 4 m single-resolution library was highly affected by the BRDF when applied to the 18 m scene. The 4 m multiple-resolution library, which was 40% smaller but was composed of one third 18 m spectra, was able to account for BRDF effects, improving R^2 by 0.28 for dissimilar classes and 0.42 for similar classes on the 18 m image. While a more controlled study design could have been used to expand EM spatial resolution variability and minimize sensor variability, we chose to investigate a method that could be available to researchers using coarse spatial resolution orbital imaging spectrometry to estimate urban cover fractions. In these cases, fine resolution EMs will likely come from airborne or ground-based sensors and will be subject to atmospheric and illumination effects that differ from orbital imagery.

Multiple-resolution libraries also estimated fractions more accurately than single-resolution libraries within their non-native scenes, indicating that libraries with multiple resolutions may be more portable across imagery. Others have demonstrated temporal portability, creating multiple-season libraries to classify vegetation, however the effect of multiple resolutions on spatial portability requires further study because we did not apply our libraries to an independent scene (Dudley et al., 2015). A portable library would be critical for mapping urban composition globally, but accounting for spectral diversity related to local materials, ecosystems, solar geometry, etc., remains a challenge. One possibility would be to use a coarse resolution spectral library containing more generalized spectra as a backbone for a multi-regional library, to be augmented with regionally-specific, fine resolution spectra for local applications.

The comparative design of this study required producing single- and multiple-resolution libraries using parallel techniques, which we accomplished with a combined manual- and automated-reduction method to refine our reference libraries and maintain within class variability and class separability. While automated random sampling and IES are easily transferrable, ICR required significant user effort and knowledge. There are many other methods for library refinement that require less user knowledge of the scene. Examples include selecting EMs based on spectral characteristics such as the class average EM RMSE, the lowest mean spectral angle, or their ability to model the most other EMs in a library (Dennison and Roberts, 2003; Roberts et al., 2003; Dennison et al., 2004). Automated Monte Carlo randomly selects multiple EM sets from a larger library, using each to unmix the image and then calculating mean fractions per pixel (Asner et al., 2003). Others have used spatial and spectral clustering to refine a large reference library into highly localized libraries (Deng,

2016). Alternative approaches focus on building libraries instead of reducing a larger set, and include using spatial constraints to automatically extract nearby EMs or synthesizing EMs for materials that may not be present as pure pixels (Berman et al., 2004; Somers et al., 2012).

4.2 The Effect of Image Spatial Resolution on Fractional Estimates

For airborne imagery, spatial resolution is a function of the sensor, including altitude, detector size, focal length, and system configuration, as well as the relationship between the pixel size and the size of ground objects (Herold et al., 2004; Jensen, 2009). A mismatch in this relationship tends to result in greater levels of pixel complexity, which itself can be an indicator of landscape properties such as development level (Powell & Roberts, 2008). In this study, we found that the average complexity of our 4 m imagery was 1.62, with 52% of pixels represented by a single EM, 34% of pixels requiring two EMs, and 14% of pixels requiring three EMs. These findings are similar to estimates made by Okujeni et al. (2013) that less than 10% of their 3.6 m pixels were composed of more than two urban cover types.

The general rule of thumb for minimum pixel size is one half the diameter of the smallest object of interest, which in urban areas results in a prioritization of imagery of 5 m spatial resolution or finer (Myint et al., 2011; Weng, 2012). The significant levels of sub-pixel mixing observed in our 4 m imagery (with 48% of all pixels requiring two or three EMs) indicate that even at 4 m resolution, urban scenes remain highly mixed. Mixtures were observed along boundary areas, such as roof edges, as well as within vegetation patches where GV, NPV, and soil were more intimately mixed. Information regarding these mixtures is important for analyses of urban vegetation function, irrigation, land management, etc., and can be lost with a whole pixel classification.

The 18 m scene had greater pixel complexity than the 4 m scene, with an average complexity of 1.85 and 74% of all pixels requiring two or three EMs to model. However, even with this greater complexity, fractional estimates at 18 m were similar to fractional estimates at 4 m. The most accurate fraction maps at each resolution (produced by the 4 m multiple-resolution library on the 4 m imagery and 18 m multiple-resolution library on the 18 m imagery) differed only by $R^2 = 0.04$ for dissimilar classes and $R^2 = 0.07$ for similar classes. This finding supports the contention that even at coarser spatial resolutions, the spectral resolution of imaging spectrometry is robust enough to conserve fractional estimates across scales, which could be of significant value for urban analysis.

4.3 Estimating Fractions of Spectrally (Dis)similar Classes using Imaging Spectrometry

We estimated spectrally dissimilar and similar fractions at 4 m and 18 m spatial resolution, achieving average $R^2 = 0.87$ for dissimilar classes and $R^2 = 0.69$ for similar classes. We observed trends in fractional accuracy between different classes, with tree fractions accurately estimated across images and library types. The values achieved in this study generally agree with similar studies that have used imaging spectrometry to identify cover fractions of VIS sub-classes, with the exception of the poor performance of our roof class, which is contrary to other studies (Roberts et al., 2012; Okujeni et al., 2013; Roberts et al., 2015; Okujeni et al., 2015). Our results are also generally more accurate than VIS fractions estimated using coarser spectral resolution imagery, such as Landsat (Powell et al., 2007).

Bhattacharyya distance analysis conducted on our 18 m reference library indicates that GV is among the most spectrally distinct urban material. In evaluating all class pairs, those

with above average Bhattacharyya distance values each contained one turfgrass or one tree EM. This is supported by the high correlation observed between MESMA fractional estimates of GV and validation fractions in our image analysis. The least spectrally distinct pairs, aside from pairs of VIS sub-classes, included tree-NPV and tree-paved. In coarser spatial-resolution imagery, these mixtures may be difficult to avoid. Tree and NPV mixtures occur naturally as trees themselves are partially composed of NPV such as bark and branches. Similarly, tree canopy gaps reveal the underlying substrate, such as soil or paved surfaces. At courser resolutions, the substrate reflectance can be integrated into a tree spectral signature, making the tree and substrate classes less spectrally distinct.

Illumination effects in the imagery increased the confusion between spectrally similar pairs, especially in the 18 m scene. Both sets of imagery were collected during similar solar incidence angles (increasing from 30.91° to 35.61° during the 4 m imaging, and decreasing from 36.47° to 30.29° during the 18 m imaging). However, different combinations of flight angle and solar azimuth resulted in different illumination environments. The 18 m scene was collected at a 35-degree northeast-southwest orientation, when the solar azimuth was between 2° and 17° from perpendicular to the flightline, producing a strong BRDF effect with marked brightness differences between the forward and backscattering view. The 4 m scene was collected along an east-west axis with the solar azimuth between 29° and 44° from perpendicular to the flightline, producing a weaker BRDF effect. Because one of the primary spectral differences between turfgrass and tree spectra is overall brightness (due to differences in canopy structure), fractional estimates of these two classes were particularly affected.

This illustrates a shortcoming of airborne imaging spectrometry, but would likely be less of an issue with data collected by an orbital imaging spectrometer. While flight planning can be used to avoid strong BRDF effects, in this case the 18 m imagery was part of NASA's HyspIRI Airborne Preparatory Campaign, which imaged 11 adjacent flightlines over Santa Barbara County. Designing a flight plan with ideal sun-sensor geometry for all flight lines while imaging all areas of interest would have required multiple days of flights, likely leading to other obstacles, such as daily changes in atmospheric properties, clouds, etc. Because we hope this study will inform approaches to processing HyspIRI-like orbital imagery, we elected to not correct for BRDF effects and instead used the standardized image product as provided by the Jet Propulsion Laboratory. Our analysis was clearly affected by this decision and future studies should carefully assess their imagery to avoid similar problems.

While slightly influenced by BRDF, confusion between paved and roof classes was more dependent upon material similarity, as their primary difference in many cases is not spectral but rather spatial and functional (Weng, 2012). While different urban materials can be spectrally unique, the flat averaged spectrum for the roof class in Fig. 1.4 illustrates the challenge of identifying these in sub-pixel mixtures. When many diverse materials are mixed together, unique spectral features are reduced and the material signal, while identifiably impervious, becomes less distinct. This may be more of a problem at coarse spatial resolutions, which have a greater likelihood of incorporating multiple materials per pixel. Paved and roof classes have been more accurately mapped by incorporating additional data, such as high resolution thermal or structural information, however such ancillary data is not available for urban areas globally and so would not be an option for improving global urban cover fraction estimates when using first-generation orbital imaging spectrometry (Roessner

et al., 2001; Bassani et al., 2007; Heiden et al., 2012). Alternatively, fractions of impervious surfaces could be separated into user-defined albedo ranges instead of roof and road classes (Wu & Murray, 2003). While this might be less desirable for mapping urban composition, such a distinction could still provide valuable information for studying urban energy balances. Future fractional analyses could also incorporate image fusion algorithms to pan-sharpen coarse imaging spectrometry to finer spatial resolutions (Selva et al., 2015).

Finally, underestimated abundances, as indicated by mean slope values of 0.84 for dissimilar and 0.70 for similar classes, is likely because MESMA was unable to identify every sub-pixel material, confusion due to shading, or discrepancies with validation polygons. When unmixing simulated mixtures with controlled sub-pixel components, MESMA estimated abundances more accurately (average slope = 0.94).

5. Conclusion

In this study, we set out to answer three questions. First, we asked how spectral library spatial resolution affects spectral library performance. We used a variety of library reduction techniques, including random sampling, IES, and ICR, to create libraries of single- and multiple- resolutions, and found that multiple-resolution libraries improved sub-pixel estimation of fractions of our study classes (mean $R^2 = 0.82$) over that of single-resolution libraries (mean $R^2 = 0.68$). Second, we asked if fractional cover information is conserved as image resolution decreases. We used MESMA to estimate fractions at 4 m and 18 m spatial resolution, and found that our best performing libraries (both multiple-resolution) had similar mean accuracy across all classes at 4 m (mean $R^2 = 0.87$) compared to 18 m (mean $R^2 = 0.81$), indicating that fractional information is conserved. Finally, we asked if imaging

spectrometry could accurately estimate fractions of VIS classes and VIS sub-classes. While sub-pixel fractions of spectrally dissimilar VIS classes were generally identified more accurately (mean $R^2 = 0.86$) than spectrally similar VIS sub-classes (mean $R^2 = 0.69$), pixel-level experiments with synthetic mixtures confirmed that spectrally similar classes could be detected, but that accuracy was affected by pixel substrate materials and brightness differences. Together, these findings suggest that spatial resolution itself can be a source of important spectral variability that, when incorporated into spectral libraries, can improve fractional estimates of narrowly-defined urban classes relative to traditional unmixing models using imaging spectrometry.

Several avenues for future research stem from this study, including additional tests that incorporate the 30 m spatial resolution of the proposed HyspIRI and EnMAP sensors. While we elected to conduct this study using only imagery at native resolutions, the ultimate goal is to develop methods that can be applied to orbital imaging spectrometry data. Second, while this study spectrally resampled the AVIRIS-NG imagery to the resolution of AVIRIS-C, it may be that additional spectral resolution could improve sub-pixel fraction estimates of spectrally similar materials. Alternatively, the extra bands could prove to be redundant, which is an important consideration when dealing with a process as computationally intensive as MESMA. Finally, while our findings showed improved portability when using multiple-resolution libraries, we did not test our libraries on an independent scene. We therefore have not confirmed the extent to which the portability observed here could be applicable for quantifying global urban composition. There is potential to explore this further with imagery collected by NASA's HyspIRI Airborne Preparatory Campaign, which collected three years of seasonal imaging spectrometry data over several California urban areas.

Cities are some of the most materially diverse environments on the planet. The potential for an orbital imaging spectrometer to quantify this diversity is enormous. Doing so requires moving beyond the convention that prioritizes spatial resolution over spectral resolution for urban imaging. Continuing to develop and refine methods for extracting accurate sub-pixel fractions of urban cover classes is a necessary step towards a future where the significant scientific potential for urban imaging spectrometry is fully realized.

Acknowledgements

This research was supported in part by NASA Grant NNX12AP08G— HyspIRI discrimination of plant species and functional types along a strong environmental-temperature gradient; by the NASA Earth and Space Science Fellowship Program; and by the Belgian Science Policy Office in the framework of the STEREO III Program— Project UrbanEARS (SR/00/307). We wish to thank the Jet Propulsion Laboratory for providing radiometrically calibrated, orthorectified AVIRIS data, and our anonymous reviewers who took the time to provide excellent feedback in revising this article.

Chapter 2

Megacity-Scale Analysis of Urban Vegetation Temperatures

With Joseph P. McFadden and Dar A. Roberts.

Reproduced with permission from Remote Sensing of Environment:

Wetherley, E.B., McFadden, J.P, and Roberts, D.A. 2018. “Megacity-Scale Analysis of Urban Vegetation Temperatures.” Remote Sensing of Environment 213 (4): 18-33.

doi: 10.1016/j.rse.2018.04.051

1. Introduction

Vegetation canopy temperature is an indicator of vegetation stress, evapotranspiration (ET) rate, and plant carbon uptake (Moran, 2004; Duursma et al., 2014; Grigsby et al., 2015). Observing vegetation temperature variability across a city is therefore critical for quantifying urban water use, energy budgets, and microclimate variability (Akbari et al., 2001; Ali-Toudert & Mayer, 2005; Moonen et al., 2012). Remote sensing can observe spatial patterns in land surface temperature (LST) across large urban spatial domains; however, the coarse spatial resolution of most remotely sensed imagery, combined with LST variability related to urban materials, tends to obscure thermal signals of vegetation stress or function (Weng, 2009).

Canopy LST can indicate vegetation stress and ET because well-watered vegetation efficiently sheds energy via latent heat flux, lowering LST (Soer, 1980). A water-stressed plant will conserve water by closing its leaf stomata, reducing latent energy exchange (transpiration) and therefore increasing canopy LST. In situ and flux tower studies can observe the physical mechanisms underlying this process, but they operate at the neighborhood rather than the city scale (Voogt & Oke, 1998; Grimmond & Oke, 1999; Arnfield, 2003; Peters et al., 2011; Stewart & Oke, 2012). Remote sensing can measure city-wide negative correlations between LST and vegetation abundance, measured as a fraction or an index value such as Normalized Difference Vegetation Index (NDVI), because areas with greater leaf area and irrigation have greater latent heat exchange (Dousset & Gourmelon, 2003; Amiri et al., 2009; Yuan & Bauer, 2007; Zhang et al., 2009; Liu et al., 2016; Zhou et al., 2017). However, remote sensing cannot observe the underlying functional mechanisms, and because vegetation fraction is a primary driver of LST variability in thermal imagery,

other drivers of vegetation LST are obscured (Weng et al., 2004).

Direct observation of city-scale vegetation LST without the effect of vegetation fraction requires thermal imagery with high spatial resolution. However, thermal infrared wavelengths have lower energy than visible, near-infrared, or short-wave infrared (VSWIR) wavelengths, and therefore require a larger ground instantaneous field of view, referred to as a pixel throughout the remainder of this manuscript. The typical spatial resolution of spaceborne thermal imagery ranges from 90 m (Advanced Spaceborne Thermal Emission and Reflection Radiometer: ASTER) and 100 m (Landsat Operational Land Imager: Landsat OLI) to 1 km (Moderate Resolution Imaging Spectrometer: MODIS) (Mushore et al., 2017). These resolutions will record a single LST value for areas larger than many common urban vegetation patches, including small residential yards or street trees, thus capturing pixels with a range of vegetation cover. Mounting thermal imagers on lower, slower airborne platforms can improve spatial resolution; however, imaging a large urban footprint would require collection over multiple days with varying conditions, and would likely preclude comparative studies between different cities (Zhao & Wentz, 2016). Therefore, quantifying urban vegetation LST variability using coarser resolution thermal imagery remains a priority.

Using coarse resolution thermal imagery to assess urban vegetation LST will require controlling for LST effects of vegetation cover, as well as other surface drivers of LST variability. One such driver is plant functional type, which in most North American cities largely consists of trees and turfgrass (Nowak et al., 2001; Milesi et al., 2005). Tree and turfgrass LST can differ for several reasons. Tree shadows cool nearby surfaces and inhibit soil water evaporation, while turfgrass has far less capacity to cast shadows (Litvak et al., 2014; Gillner et al., 2015). Trees and turfgrass also access water differently because their root

systems are at different depths, although variation in built infrastructure and management practices can increase rooting depth variability in urban trees (Grabosky & Gilman, 2004; Bijoor et al., 2012). From the point of view of a thermal imager, another difference between tree and turfgrass LST is that the LST of tree-covered patches can be affected by the diversity of materials beneath the canopy, such as other vegetation, pavement, or roofs, whereas turfgrass LST does not include effects of dissimilar materials because it does not have an understory (Friedl, 2002). Assessing LST solely in relationship to green vegetation fraction or NDVI ignores these and other sources of LST variability related to vegetation type.

The diversity of abiotic materials found in a city is also a key source of LST variability, due to material properties such as albedo, thermal conductivity, moisture content, and structure (Oke, 1988). Pixels with low vegetation fraction will have LST that is dominated by that of the non-vegetated material, making it especially important to control for this variable when using coarse spatial resolution imagery (Sandholt et al., 2002; Weng, 2009). Furthermore, non-vegetated surfaces can affect nearby vegetation, sometimes in contradictory ways. For example, asphalt can increase ET by advection of warm air over well-watered vegetation, but it can also decrease ET by inducing stomatal closure in overhanging tree canopies (Oke, 1979; Oke, 1988; Kjelgren & Montague, 1998).

Explicit categorization and quantification of surface heterogeneity is the first step for evaluating vegetation LST variability in a thermal image. This must be accomplished over a large urban extent in order to observe a wide range of possible vegetation thermal responses across percent cover gradients of plant functional type and material composition. Surface heterogeneity is generally quantified using optical imagery and, if acquired across a large city, will likely be at spatial resolutions typical of spaceborne sensors such as Landsat OLI (30 m).

At these scales, sub-pixel analysis is necessary to quantify vegetation fractional cover and material mixtures. Sub-pixel composition and fractions are typically estimated using some form of linear spectral mixture analysis (SMA) (Settle & Drake, 1993). SMA assumes that reflectance measured in each pixel is the linear combination of the reflectances from all sub-pixel materials, weighted by their relative fraction within the pixel. For urban environments, Multiple Endmember Spectral Mixture Analysis (MESMA) is particularly well-suited because it allows different cover classes to be represented by multiple endmembers (EM) (Roberts et al., 1998). For example, with MESMA a green vegetation class can be represented by spectra from multiple species of tree and turfgrass, while an impervious surface class can include spectra from concrete, asphalt, metal, or any other material of interest. Incorporating multiple EMs makes MESMA a robust method for unmixing scenes with extreme material diversity, and it has therefore been used to unmix urban scenes across the globe (Rashed et al., 2003; Powell et al., 2007; Franke et al., 2009; Roberts et al., 2012; Wu et al., 2014).

Typically, urban sub-pixel analysis is used to estimate fractions of vegetation, impervious surfaces, and soil (VIS) because these groups tend to be spectrally distinct and therefore easier to discriminate using SMA (Ridd, 1995; Wu, 2004). However, teasing out LST differences between plant functional types and urban materials requires more functionally uniform class definitions than the VIS model provides. A limited number of studies have assessed city-scale temperatures of urban trees and/or turfgrass separately across changing cover fractions, but they have not accounted for the effects of variability in the non-vegetated fraction (Myint et al., 2013; Myint et al., 2015; Jenerette et al., 2016; Zhou et al., 2017). Another group of studies has investigated the role of impervious surface fraction;

however, they have not accounted for differences in plant functional types and other variability related to the non-impervious fraction (Yuan & Bauer, 2007; Zhang et al., 2009; Buyantuyev & Wu, 2010; Morabito et al., 2016). More recently, studies have used the spectral resolution of hyperspectral imagery as well as the EM diversity allowed by methods such as MESMA to expand the VIS model to include tree, turfgrass, roof, impervious surface, non-photosynthetic vegetation (NPV), and soil (Okujeni et al., 2013; Okujeni et al., 2015, Roberts et al., 2017; Wetherley et al., 2017). This creates an opportunity to assess urban LST across both vegetated and abiotic sub-pixel fractions that have unique effects on water and energy fluxes.

In this study, we leveraged these recent advances in our ability to define more functionally uniform sub-pixel classes to quantify material and plant type heterogeneity across the megacity of Los Angeles, California, USA. A megacity is a large urban area with a population in excess of 10 million people (United Nations, 2016). Conducting a study across a megacity allows for a sufficient sample size of pixels with varying surface heterogeneity and associated LST measurements. We extracted 1.7 million pixels to construct plant functional type and urban material fractional gradients and evaluate changing LST. We then derived an expected temperature response based on sub-pixel composition in order to assess deviations from measured temperatures across the study area. We produced a map of vegetation LST variability and investigated additional drivers of vegetation LST that are difficult to observe at city-scales. Specifically, we asked the following questions:

1. What is the urban plant and material variability of Los Angeles?
2. How do plant and material type affect measured LST?
3. How does vegetation LST vary across a megacity?

2. Methods

2.1. Study area

The study area included 4,466 km^2 of urbanized land within the Los Angeles metropolitan area (Los Angeles) (Fig. 2.1). Los Angeles is situated in southern California along the Pacific coast, and includes parts of Los Angeles, Orange, Riverside, San Bernardino, and Ventura Counties (average elevation of 161.8 m and standard deviation of 137.3 m; USGS National Elevation Dataset). It is composed of a range of residential, commercial, industrial, and agricultural areas, with a primary downtown in the city of Los Angeles along with several other urbanized centers located throughout. Urban materials are typical of North American cities, with large expanses of asphalt, concrete, and roofing materials. Area vegetation consists of ~200 urban tree species as well as irrigated lawns, with tree canopy cover varying between neighborhoods by 7–37% in the city of Los Angeles alone (McPherson et al., 2011; Clarke et al., 2013). Los Angeles experiences a Mediterranean climate, receiving an average of 37.9 cm of precipitation annually, mostly during the winter months (U.S. Climate Reference Network: Diamond et al., 2013). Summers in Los Angeles are dry and typically receive only trace amounts of rainfall, requiring urban vegetation in Los Angeles to be largely irrigated. Image collection occurred during the 2012–2015 California Megadrought, which is estimated to be California's most severe drought in the past ~1,200 years (Griffin & Anchukaitis, 2014; Asner et al., 2016).

Study area boundaries were determined using the U.S. Census Bureau's 2010 Urbanized Areas boundary layer, which delineates population zones of 50,000 or more (U.S. Census Bureau, 2010). We used five Urbanized Areas that compose the contiguous Los Angeles metropolitan area: Camarillo, Los Angeles-Long Beach-Anaheim, Riverside-San

Bernardino, Simi Valley, and Thousand Oaks, which collectively have a population of 14,495,451 (U.S Census Bureau, 2010). To ensure that we were examining exclusively urban vegetation, we manually removed large agricultural or undeveloped areas within the Urbanized Area boundaries, including a 1,000 m buffer of land along the edge of the study area.

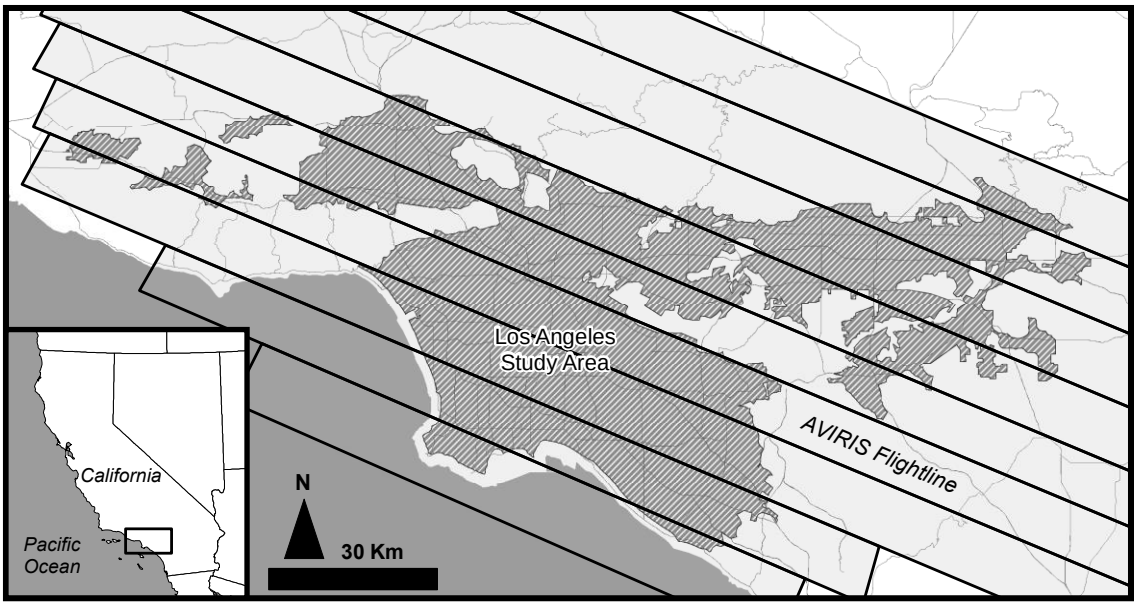

Figure 2.1. Urbanized Los Angeles study area (gray hash marks) and AVIRIS flightlines located in southern California (map inset). Major roads shown as light gray lines.

2.2. Remotely sensed data

Remote sensing imagery of the study area was collected on August 26, 2014 as part of the NASA Hyperspectral Infrared Imager (HyspIRI) Preparatory Airborne Campaign. Hyperspectral reflected VSWIR imagery was collected by the Airborne Visible/Infrared Imaging Spectrometer (AVIRIS), while thermal emissivity was collected by the MODIS-ASTER (MASTER) Airborne Simulator (Green et al., 1998; Hook et al., 2001). Both imagers were flown simultaneously aboard the NASA-ER2 high altitude airborne platform, producing

an AVIRIS swath width of ~12 km and MASTER swath width of ~40 km. AVIRIS imagery aligned with the nadir view of the MASTER imagery. Due to the large study area size, 9 flightlines composing a seamless AVIRIS scene were collected from 10:20–16:00 PDT. Solar noon on the day of flight was at 12:54 PDT, meaning that data were imaged from 2.6 hours before to 3.1 hours after solar noon. The weather on the day of collection was cloud free with mean air temperature peaking at 30.0°C at 13:50 PDT, as calculated from 14 U.S. Climate Reference Network observation stations located throughout the study area (Diamond et al., 2013).

AVIRIS measures 224 narrow bands (10 nm full width at half maximum) of reflected radiance, ranging between 0.38 – 2.5 μm (Green et al., 1998). Initial image processing was conducted by the Jet Propulsion Laboratory (JPL), where imagery was radiometrically corrected, orthorectified, and resampled to 18 m spatial resolution. The standard HyspIRI reflectance product was used in this study (Thompson et al., 2015). MASTER imagery was processed by JPL to calculate per-pixel LST using temperature-emissivity separation (TES) (Gillespie et al., 1998). TES uses atmospherically-corrected thermal radiance to estimate per pixel LST and emissivity. It relies on an empirically-derived relationship between the minimum emissivity value (ε_{min}) and the spectral contrast, defined as the difference between the maximum and minimum emissivities (MMD). Accuracy and precision was assessed by the Ames Research Center, who reported the overall accuracy of LST retrievals to be ≤ 0.33°K, and per band sensor precision as measured by noise equivalent differential temperature (NEdT) to range from 0.15°K–0.74°K (Jeffrey Myers, personal communication). The LST product was spatially resampled (nearest neighbor) to 36 m.

We corrected for remaining locational errors using a NAIP basemap, aggregated to 18 m and 36 m for the AVIRIS and MASTER imagery respectively, and DeLaunay Triangulation. An average of 25 ground control points (GCP) were collected per MASTER flightline (average error: 0.62 pixels) and 26 GCPs per AVIRIS flightline (average error: 0.65 pixels). AVIRIS bands showing strong atmospheric interference were removed. The remaining 179 bands were calibrated to remove spectral features resulting from either over or underestimation of atmospheric transmission during reflectance retrieval. This was done using spectra collected by the AVIRIS-Next Generation (ANG) imager, which was flown on September 1, 2014 over a small portion of our study area, producing imagery with 1.9 m resolution and reflectance lacking significant artifacts. We identified a bright, dry soil target in both the AVIRIS and ANG imagery, and used a polygon to extract an averaged soil spectrum from the target for each image. We then spectrally resampled the ANG imagery to AVIRIS wavelengths, and created a band-by-band ratio of reflectance values for all 179 bands of interest. The average ratio value was 1.013 with a standard deviation of 0.081, indicating that the soil target spectra were similar between the two images (Fig. 2.2). However certain bands displayed greater deviations, ranging from a minimum of 0.698 to a maximum of 1.24. We used the band-specific ratio values to calibrate all AVIRIS spectra. Finally, we used spectral averaging to aggregate the 18 m AVIRIS imagery to the 36 m resolution of the MASTER imagery.

2.3. In situ data

Hourly daytime LST for several impervious surfaces was collected in situ on the University of California, Santa Barbara (UCSB) campus on August 28, 2014 from 9:30–

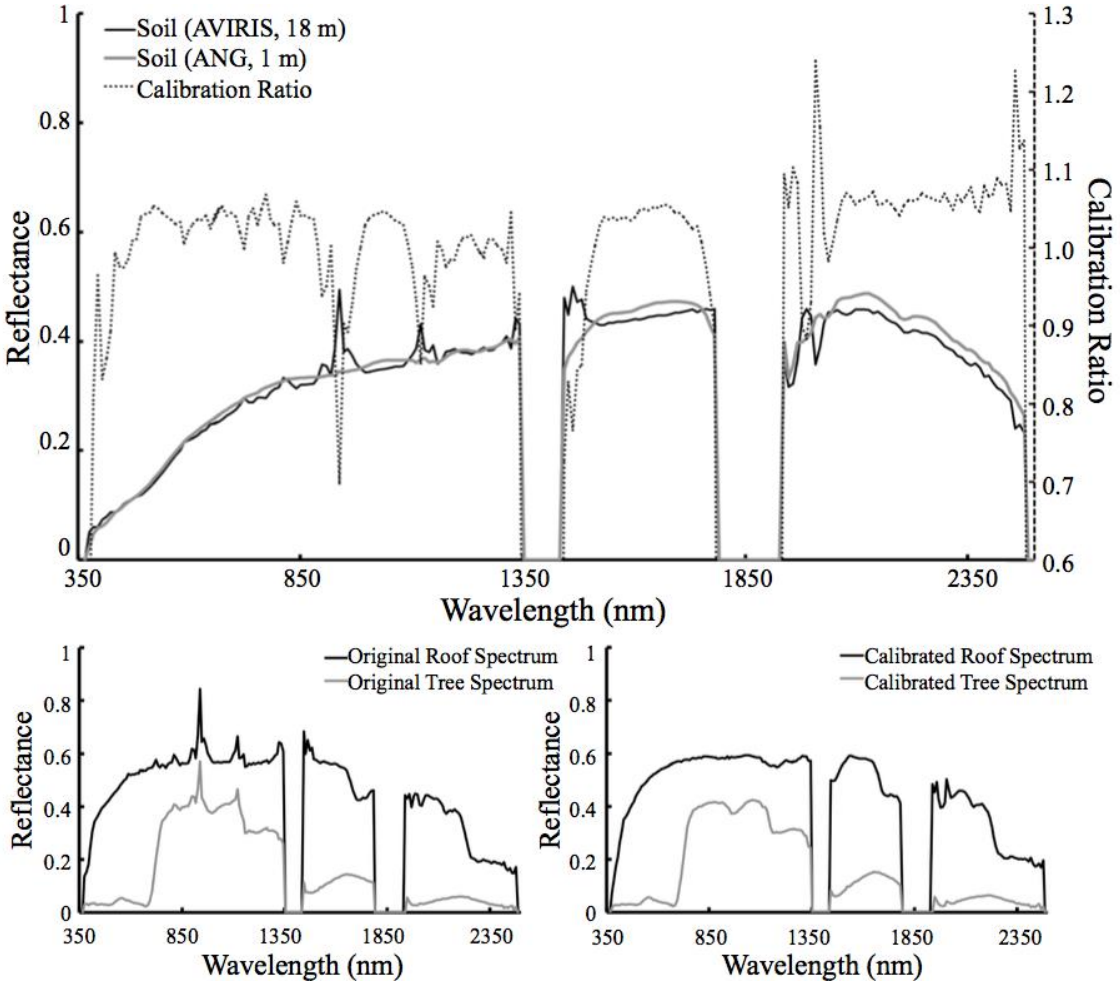

Figure 2.2. Calibration spectra extracted from a homogenous soil patch from AVIRIS and ANG imagery, as well as the spectral ratio used to correct all imagery (top). Example spectra from original (bottom left) and calibrated (bottom right) AVIRIS imagery. Gaps indicate bands that were removed prior to calibration due to atmospheric absorption.

16:30 PDT. While not located within the study area, UCSB is situated at a similar latitude, within a similar climate, and was experiencing similar drought conditions. Maximum air temperature in Santa Barbara on the day of collection was 28.3°C. LST was measured under clear-sky conditions for 3 concrete surfaces and 3 asphalt surfaces using an Apogee IRTS-P Precision Infrared Temperature Sensor, which measures between 6–14 μm (Logan, Utah, USA). All surfaces were flat and fully sunlit throughout the day.

Raw LST was corrected for instrument body temperature using instrument-specific calibration values. We then corrected for emissivity effects of each surface using an assumed emissivity value of 0.94 for both asphalt and concrete (Kotthaus et al., 2014). Downwelling longwave radiation measurements were collected using a Kipp & Zonen CNR1, which was mounted to a meteorological tower located 3.15 km due west from UCSB (Kipp and Zonen, Delft, Netherlands). The CNR1 measures thermal radiation between 5–50 μm. Because this was a larger spectral range than that measured by the IRTS-P, we scaled our longwave measurements by the proportion of thermal radiation emitted between 6–14 μm. This was calculated by using MODTRAN 4.3 to simulate path thermal radiance from the atmosphere using similar conditions as the day of in situ collection (Berk et al., 2005). We found that 28.6% of the energy emitted from the simulated atmosphere between 5–50 μm occurred between 6–14 μm, so all downwelling longwave measurements from the CNR1 were multiplied by 0.286 to better represent the thermal radiance sensed by the IRTS-P. Additionally, downwelling and upwelling shortwave radiation measurements were collected concurrently to each in situ measurement using an Apogee Model MP-200 hand-held pyranometer to calculate surface albedo.

2.4. Fraction estimation and validation

We estimated sub-pixel fractions of tree, turfgrass, impervious surface, commercial roof, NPV, and soil for all 9 AVIRIS flightlines. We used a spectral library composed of representative EMs extracted from all flightlines. Locations of representative surfaces of all 6 classes were manually identified using high resolution Google Earth imagery. We extracted a minimum of 10 spectra per flightline from dispersed locations, including forwardscattering,

backscattering, and nadir viewing geometry. EMs located in sidelap areas were extracted from both flightlines. We removed duplicate spectra to produce a final spectral library of 706 EMs. An existing library of Santa Barbara spectra, produced from imagery collected by the same airborne campaign, was used to visually confirm the purity and accuracy of each spectrum (Wetherley et al., 2017).

We randomly selected and removed 20% of each class, independent of flightline, to be used for validation. The remaining 80% consisted of too many spectra for efficiently estimating fractions using MESMA, so we used iterative endmember selection (IES) to reduce the library (Schaaf et al., 2011; Roth et al., 2012; Somers et al., 2016). IES automatically selects a smaller subset of representative spectra from a larger library by using a kappa value to assess the ability of each EM to classify the entire library. The EM producing the highest kappa value is saved to a smaller IES library. This is an iterative process—each time an EM is selected, IES tests for further improvement by individually subtracting each selected EM and recalculating the kappa value until the original library is optimally represented. Our final library contained 57 EMs, including 8 tree, 6 turfgrass, 9 impervious surface, 22 commercial roof, 7 NPV, and 5 soil.

We used MESMA to estimate sub-pixel fractions across each AVIRIS flightline (Roberts et al., 1998). For each measured spectrum, MESMA evaluates all 1-, 2-, and 3-EM combinations, selecting the best combination by calculating the RMSE between the measured spectrum and the EM model. While more complicated models, produced with more EMs, tend to achieve lower RMSE, they also require more processing power and do not necessarily represent a more accurate estimate of cover fractions (Powell et al., 2007). We therefore constrained MESMA using parameters obtained from the literature to only select a more

complicated model if it improved the RMSE by 0.7% or more (Roberts et al., 2012). Pixels that could not be modeled by our library with an RMSE ≤ 2.5% were left unclassified. We used a photometric shade component to account for brightness differences between modeled and measured spectra, limiting it to ≤ 20% of individual pixel reflectance. Each pixel could contain no more than 3 sub-pixel components, as well as shade, and only one class EM per pixel, e.g., MESMA did not assess mixtures of two turfgrass EMs. Final fractional estimates were shade normalized (Adams et al., 1993).

We assessed class and fractional accuracy using two methods: validation polygons within our imagery and simulated mixtures. We produced 45 validation polygons, each 180 m^2, distributed across Los Angeles. Land cover within each polygon was determined using a high-resolution classification map, which included tree, turfgrass, impervious surface, and NPV (McPherson et al., 2008). Additionally, we assessed pixel-level vegetation fraction accuracy by simulating 1,000 linear mixtures representing all possible two-class combinations of vegetation (tree or turfgrass) and each non-vegetated class, using EMs which had been randomly removed from our library. We used MESMA to estimate fractions using identical parameter values as those described above. Validation polygons and simulated mixture validation were assessed using R^2 and slope, derived from plotting MESMA fractions (y) against known fractions (x).

2.5. Modeling expected LST based on sub-pixel composition

Pixels modeled by 1 EM and 2 EMs were used to characterize material drivers of LST across the study area. Pixels modeled by 1 EM represented “pure” pixels and were used to extract general LST information about each class. Mixed pixels modeled by 2 EMs were used

to characterize LST change as fractional vegetation cover transitioned from 0 to 1. Mixed pixels that did not contain a vegetated/non-vegetated mixture were excluded from this analysis. All pixels, including 3 EM mixtures, were used to calculate land cover statistics.

We assessed four groups of mixed (2 EM) pixels across each AVIRIS flightline: tree-impervious, tree-NPV, turfgrass-impervious, and turfgrass-NPV. Vegetated mixtures with commercial roof and soil were excluded because we were unable to validate these in the imagery. Using fractional bins of 10%, we calculated LST mean and standard deviation from 5% to 95% vegetated fraction. We used a linear model to construct LST-cover curves for each compositional group, then assessed all slopes to quantify how vegetation type (tree or turfgrass) and non-vegetated surfaces (impervious or NPV) affected LST. This analysis was conducted using the nadir-view of each MASTER flightline, subset to the 12 km swath width of the corresponding AVIRIS flightline. However, because each AVIRIS flightline imaged a different spatial domain within the study area, we conducted an additional comparative LST-cover analysis for pixels in the MASTER forwardscattering, backscattering, and nadir viewing geometry to investigate the extent to which LST and LST-cover curve slopes were affected by flightline-specific fractional composition.

2.6. Mapping city-scale vegetation temperatures

We used the slopes and intercepts of the above LST-cover curves to model an expected LST for each pixel based on its composition and fraction, such that:

$$LST_m = m_{FL} \times f_{PFT} + b_{FL} \quad [2.1]$$

where LST_m is the modeled temperature, m_{FL} and b_{FL} are the slope and intercept, respectively, of the LST-cover curve for the specific flightline and sub-pixel mixture, and f_{PFT} is the tree or turfgrass fraction. We then subtracted LST_m from measured LST, such that:

$$LST_0 = LST - LST_m \quad [2.2]$$

where LST_0 represents the residual value between the measured and modeled LST, indicating remaining vegetation temperature variability independent of vegetation fraction, plant functional type, and urban material. Pixels with LST_0 values close to zero are those with similar measured and modeled LST, while those with positive LST_0 are warmer than the model and those with negative LST_0 are cooler than the model.

We produced a map of LST_0 across the Los Angeles study area and then assessed additional drivers of vegetation LST using three separate GIS data sets: building footprints in Los Angeles County (LA County GIS, 2008), block group-level median income (U.S. Census Bureau, 2010), and residential water use data (Los Angeles Department of Water and Power; Mini et al., 2014) that were aggregated to sub-neighborhood scale postal carrier routes (Chen et al., 2015).

3. Results

3.1. Land cover of Los Angeles

Validation with simulated mixtures showed a similar range of accuracy for tree (R^2 = 0.75, slope = 0.76), turfgrass (R^2 = 0.82, slope = 0.89), impervious surface (R^2 = 0.65, slope = 0.81), commercial roof (R^2 = 0.78, slope = 0.84), NPV (R^2 = 0.79, slope = 0.78), and soil (R^2 = 0.84, slope = 0.84). Overall values were slightly underestimated, as indicated by all slopes being < 1, as is typical with MESMA fractional estimates (Wetherley et al., 2017).

Assessment of accuracy using validation polygons indicated that fractions within the study area were well-characterized for turfgrass ($R^2 = 0.94$), tree ($R^2 = 0.82$), impervious surface ($R^2 = 0.77$), and NPV ($R^2 = 0.80$), with a slight intercept offset observed for turfgrass (Fig. 2.3).

The study area was dominated by impervious surfaces (59%), which included ground pavement such as asphalt and concrete, as well as non-commercial (residential) roofs. Despite the drought, nearly one quarter of the study area was vegetated, with trees representing 20% of the land cover and turfgrass representing 4%. Neighborhoods throughout the study area displayed different levels of vegetation cover. The remaining 17% of the study area contained NPV (7%), commercial roofs (6%), and soil (4%) (Fig. 2.4). Because we excluded marginal and agricultural land, the amount of detected NPV and soil was significantly less than that found in undeveloped land surrounding the study area.

To evaluate how SMA affected total cover estimates at a 36 m spatial resolution, we categorized each pixel as its majority class to produce a classification map and compare land-cover estimates with our sub-pixel classification. We found that SMA increased estimates for turfgrass (1.7%), tree (6.3%), commercial roof (3.2%), NPV (2.2%), and soil (0.9%), while it decreased the estimate of impervious surface by –14.3%.

3.2. Urban plant and material temperatures

We assessed general LST characteristics for each class using pure pixels (5.8% of the imagery). Within the warmest flightline, NPV was the warmest class with a mean LST of 57.9°C. Commercial roof (56.9°C), soil (56.7°C), and impervious surface (54.9°C) pixels expressed similar temperatures, while tree (44.3°C) and turfgrass (41.4°C) pixels were

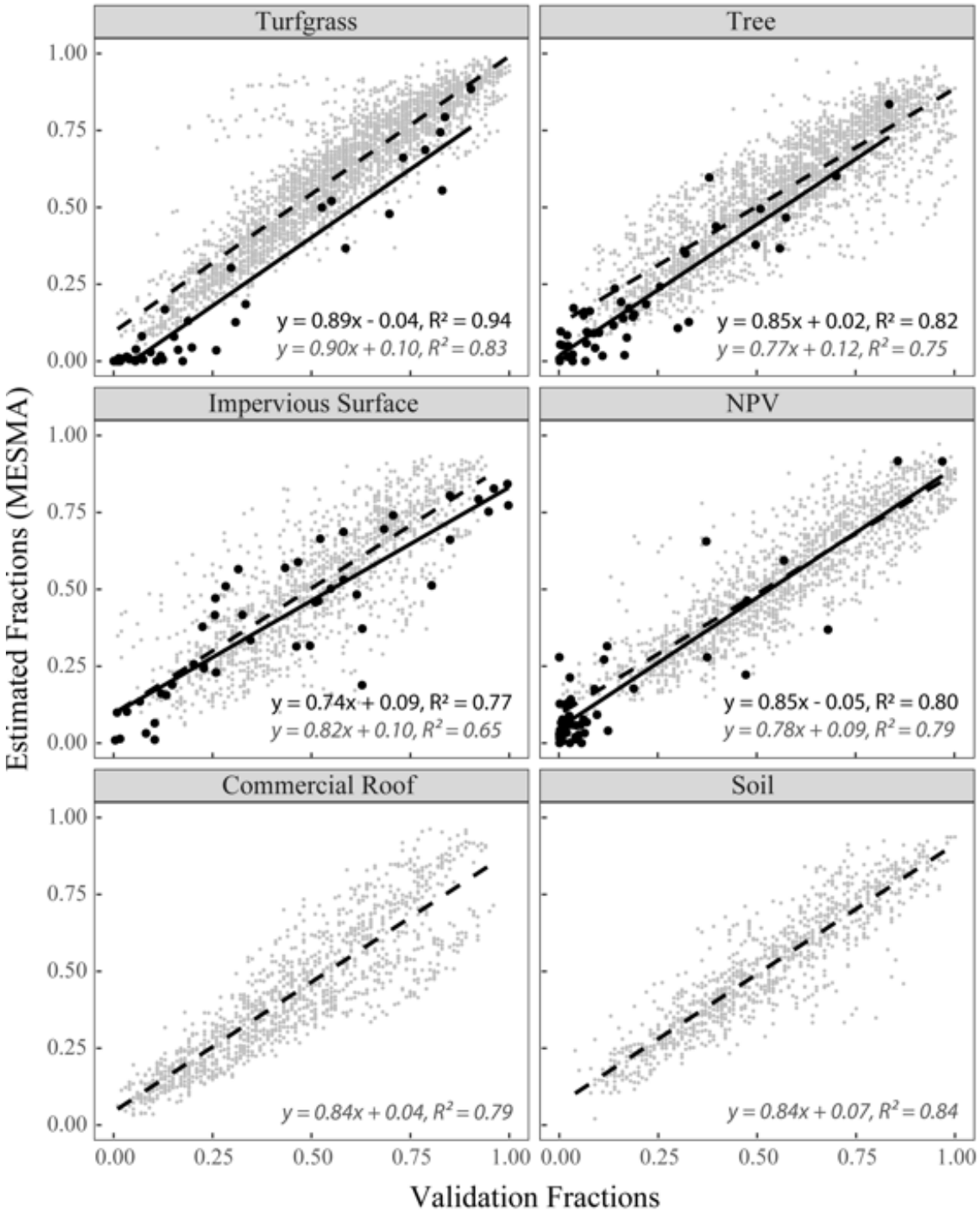

Figure 2.3. Validation scatterplots for validation polygons (black dots with solid line and equation in black text) and simulated mixtures (gray dots with dashed line and equation in gray text). Commercial roof and soil classes were validated using simulated mixtures only.

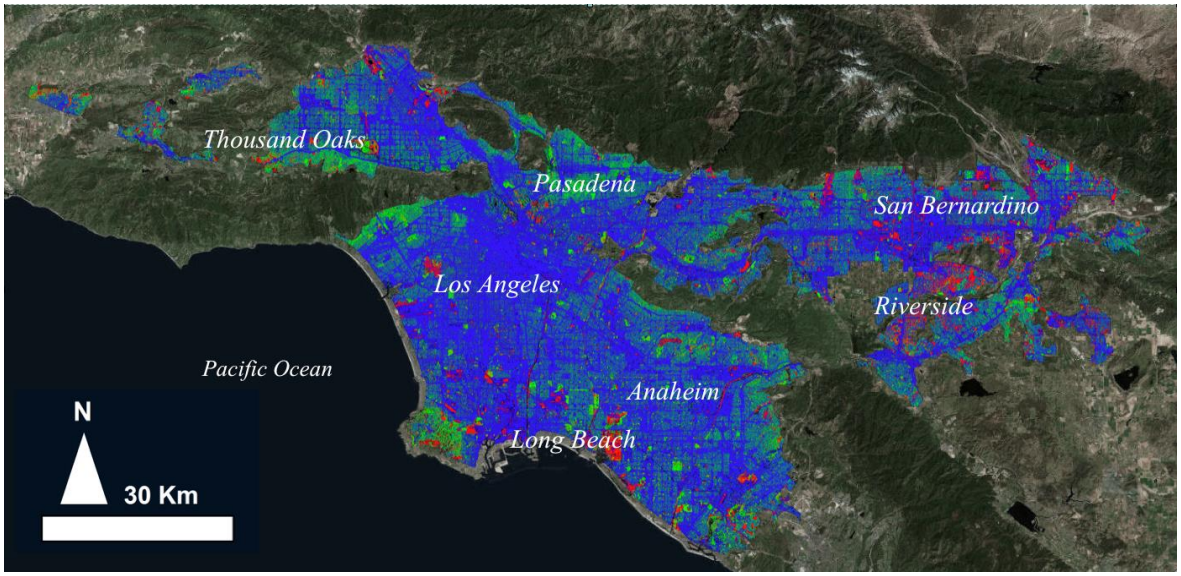

Figure 2.4. Fractional map showing combined soil and NPV (red), tree and turfgrass (green), and impervious surface and commercial roof (blue), overlaid on RGB imagery. Urban centers are labeled for reference.

cooler. Because the 9 MASTER flightlines were collected over a 5.7-hour window, we assessed hourly daytime mean LST for each class by arranging flightlines in chronological order (Fig. 2.5a). Vegetated pixels remained significantly cooler than non-vegetated pixels throughout the day. In the morning, mean turfgrass LST was warmer than tree pixels by 2.1°C; however, just before solar noon their temperatures equalized and, from solar noon until the final flightline, trees remained warmer than turfgrass by a maximum of 3.9°C. Vegetated classes also demonstrated a more depressed daytime range of LST compared to non-vegetated LST ranges: mean tree and turfgrass LST had daytime ranges of 13.6°C and 9.7°C, respectively, while greater variation was observed for commercial roof (17.7°C), NPV (15.8°C), impervious surface (15.7°C), and soil (15.6°C).

Because flightlines were collected parallel to and at different distances from the coastline, LST differences between flightlines were likely influenced by both diurnal changes as well as a coastal-interior gradient. During the daytime, temperatures tend to be cooler

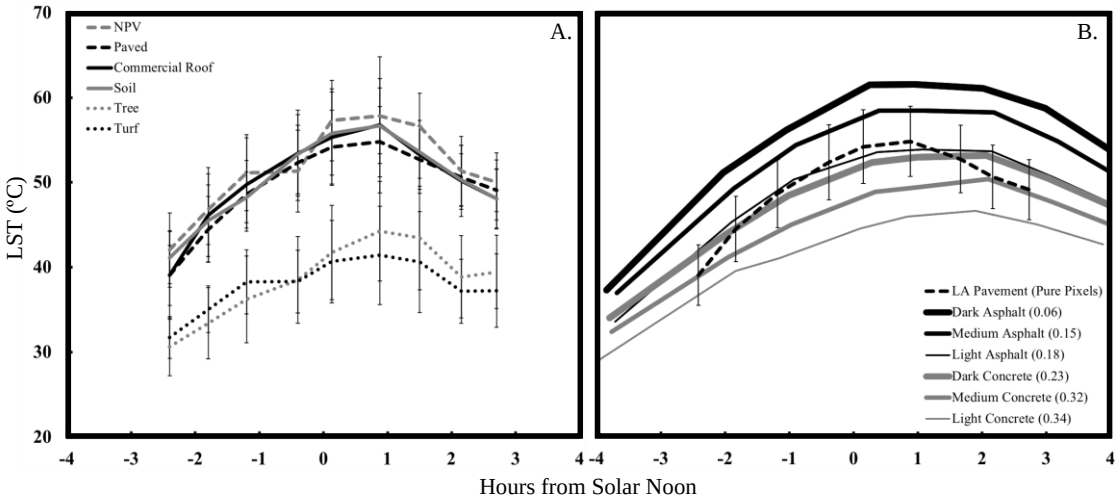

Figure 2.5. A.) Changing daytime LST for pure pixels. Each measurement represents the mean LST for pure pixels (1 EM) of each class in one flightline, arranged in chronological order. B.) Comparison of pure pixel impervious LST to in situ measurements. Material albedo indicated in parentheses. Error bars in both figures show LST standard deviation per flightline.

nearer to the coast, due to the moderating influence of the ocean, and warmer farther from the coast. In our MASTER dataset, we observed that, following solar noon, consecutively collected flightlines had cooler average LST for more interior flightlines, indicating a dominant diurnal effect. We examined this by comparing mean pure-pixel impervious LST to in situ LST measurements of several impervious surface types collected over the course of a day on the UCSB campus (Fig. 2.5b). The most absorptive material measured in situ was asphalt, which had albedos ranging from 6%–18%. Concrete was more reflective, ranging from 23%–34% albedo. In situ surfaces were fully sunlit and horizontal, while pure impervious surface pixels contained a mixture of impervious material types and structure. We found the daytime patterns of impervious surface LST to closely resemble observed in situ LST patterns, falling in the middle of the range of measured material LST. Flightline impervious LST showed steeper slopes of warming in the morning and cooling in the evening

compared to in situ LST, possibly due to changing shadows at low solar zeniths whereas in situ surfaces remained sunlit.

3.3. LST of heterogeneous land cover

Across the study area, 83.3% of all pixels were modeled with 2 EMs. We used these to analyze pixel-level LST with changing vegetation fraction for four pixel mixtures: tree-impervious, tree-NPV, turfgrass-impervious, and turfgrass-NPV. The distribution of LST values was significantly different for all mixture groups ($p < 0.0001$). As expected, LST-cover curves showed decreasing LST with increasing vegetation fractional cover for all groups, and this relationship was observed to be predominantly linear (Fig. 2.6). We observed a significant effect of plant functional type (turfgrass versus tree): an increase in turfgrass cover of 10% resulted in 1.6°C +/- 1.1°C more LST cooling than did a similar increase in tree fraction ($p < 0.001$). We also observed a significant effect of non-vegetated substrate (NPV versus impervious surface): an increase in NPV cover of 10% increased LST by 3.1°C +/- 1.0°C more than a similar increase in impervious surface fraction ($p < 0.001$). This larger slope for NPV mixtures was consistent across all flightlines, representing a greater change in LST as sub-pixel composition transitioned from non-vegetated to vegetated surfaces.

When assessing vegetation type and non-vegetated surface type in combination, we found significantly different slopes between turfgrass and tree when mixed with impervious surface: an increase in turfgrass cover of 10% resulted in 3.2°C +/- 1.1°C more cooling than a similar increase in tree fraction ($p < 0.001$). While we did not quantify nonlinearity for these curves, turfgrass-impervious mixtures appeared to exhibit slight nonlinear behavior, showing a larger decline when the turfgrass fraction reached approximately 50%. No significant

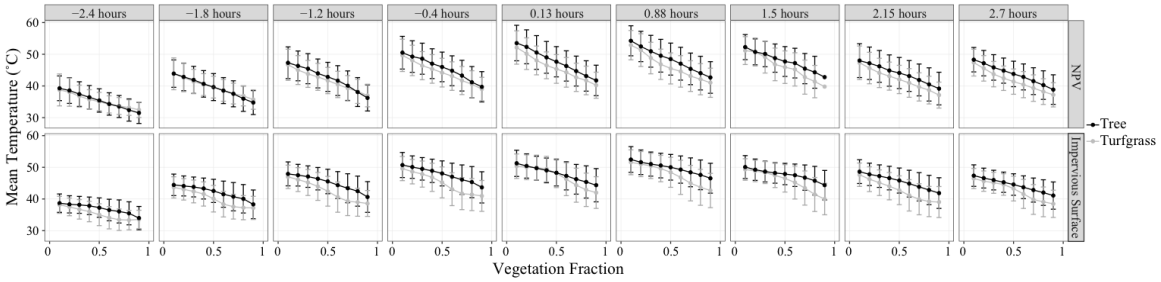

Figure 2.6. LST-cover curves showing change in LST with increasing fraction of tree (black) and turfgrass (gray) mixed with NPV (top) and impervious surface (bottom) for each flightline. Column names indicate the time each flightline was collected relative to solar noon. Error bars show LST standard deviation.

difference was observed between the slopes of turfgrass and tree when mixed with NPV, however these groups did have significantly different LST, with trees averaging 1.8°C +/- 0.1°C warmer than turfgrass ($p < 0.001$).

Slopes for all LST-cover curves varied between flightlines (measured as the total LST change as pixel vegetation fraction transitioned from 0 to 1, or °C/1.0 pixel). Slopes for tree-impervious mixtures ranged between –8.9 to –5.5 with a mean of –7.6, while slopes for turfgrass-impervious mixtures ranged between –12.0 to –6.6 with a mean of –10.8. Tree-NPV mixture slopes ranged from –14.9 to –9.9, with a mean of –12.3, while turfgrass-NPV mixture slopes ranged from –14.8 to –7.9, with a mean of –12.2. Absolute slope values for all mixtures became larger as the morning progressed (Fig. 2.7). Impervious mixtures began to stabilize around an hour before solar noon, while NPV mixtures continued to grow until just after solar noon. Intercept values followed a clear diurnal pattern, peaking around an hour after solar noon before declining.

In addition to diurnal effects, slope differences between flightlines could be due to the fact that each flightline imaged a different subset of the study area. We investigated this possibility by subsetting each MASTER flightline into three spatial domains and re-

calculating the slopes for all LST-cover curves. Spatial subsets represented nadir (center), forwardscattering (southern flightline edge), and backscattering (northern flightline edge) viewing geometry. Differences in LST-cover slope values calculated within each of these domains were found to be statistically insignificant, however LST overall was affected by viewing geometry. Backscattering LST tended to be a slightly warmer than nadir LST (average of 0.7°C across all flightlines), while forwardscattering LST tended to be significantly cooler than nadir (average of 2.3°C across all flightlines) ($p < 0.0001$).

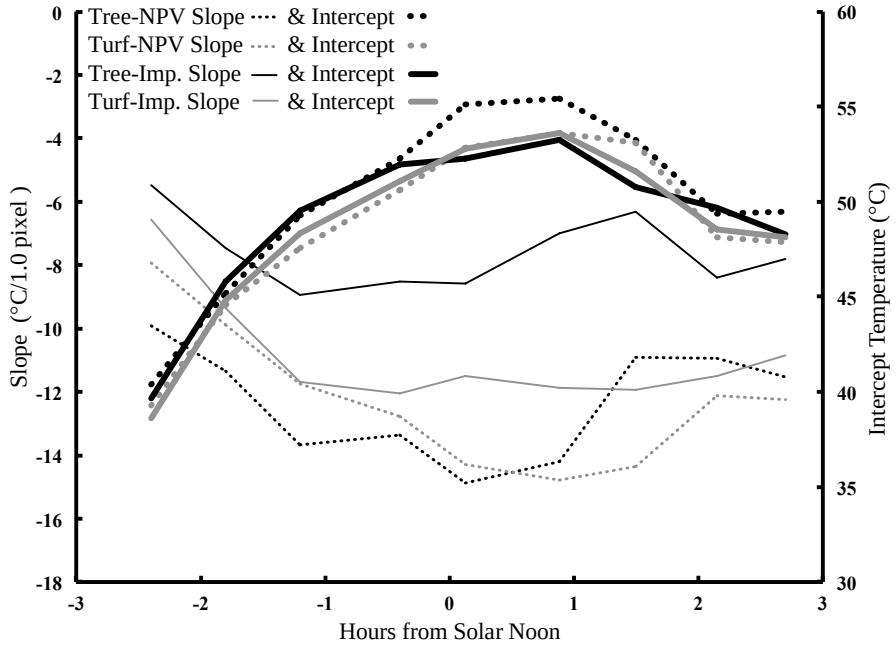

Figure 2.7. Daytime change in slope and intercept for all mixture groups. Color denotes tree (black) or turfgrass (gray), style denotes NPV (dots) or impervious (solid line), and weight indicates slope (thin) or intercept (thick).

3.4. City-scale vegetation temperatures

We subset the 40 km swath of each MASTER flightline to the 12 km swath width of the nadir-view AVIRIS flightline to minimize viewing geometry effects on LST. We used Eq.

2.1 to calculate per-pixel expected LST based on sub-pixel composition, fraction, and flightline, then used Eq. 2.2 to calculate LST_0 for all 2 EM mixtures of tree-impervious, tree-NPV, turfgrass-impervious, and turfgrass-NPV. Such mixtures comprised 1,762,529 pixels, or 53% of the study area. Flightlines were mosaicked by overlapping the backscattering view over the forwardscattering view, producing a map of LST_0 values with a mean of 0.3°C and standard deviation of 3.5°C, which exceeded the reported NEdT of the MASTER sensor (Fig. 2.8). While slight image effects were observed along flightline boundaries, patterns of neighborhood-level vegetation LST variability were revealed across the study area. We used this map of city-scale LST_0 to investigate additional drivers of vegetation temperature variability.

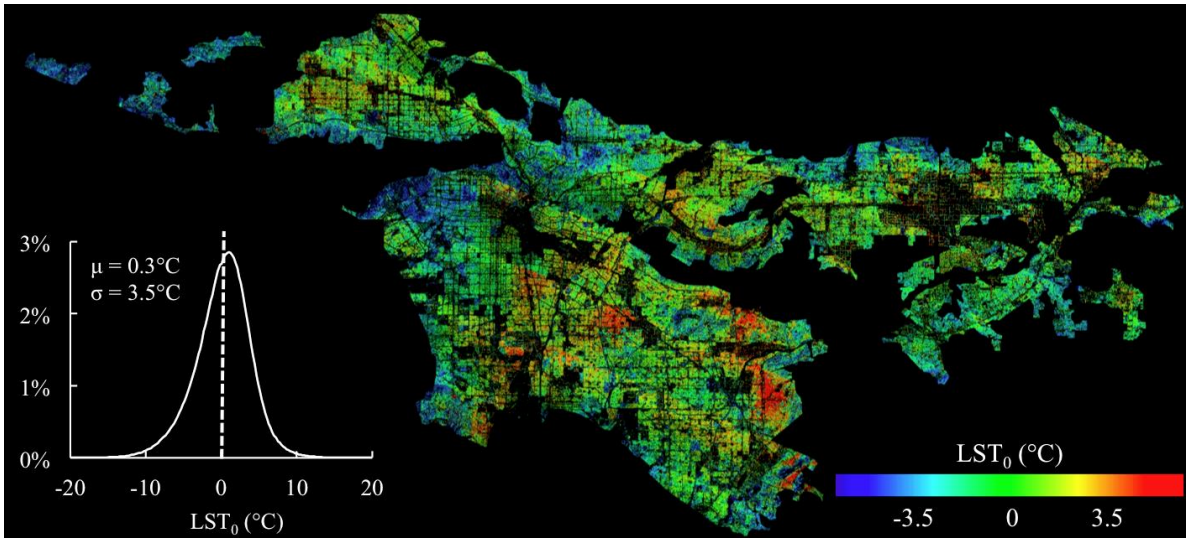

Figure 2.8. Map of LST_0 for all pixels containing mixtures of tree and turfgrass with impervious surface or NPV (53% of the image). Red indicates positive LST_0 (warmer than expected based on sub-pixel composition and fraction), blue indicates negative LST_0 (cooler than expected). Distribution of all LST_0 values shown on the left with dashed line at 0°C.

3.4.1. Building density

Buildings can increase surrounding temperatures by re-radiating absorbed energy or releasing anthropogenic heat, or they can decrease surrounding temperatures by blocking direct solar radiation or channeling wind (Arnfield, 2003; Lindberg & Grimmond, 2011; Stewart & Oke, 2012). To assess how building density affected vegetation LST across our study area, we used a GIS layer of Los Angeles County building footprints (for all buildings > 6 m^2 based on 2008 10-cm orthorectified aerial imagery) to calculate the roof fraction for each 36 m pixel of our imagery. We then evaluated LST_0 for all tree-impervious and turfgrass-impervious mixed pixels that contained a roof fraction. Overall, tree and turfgrass LST_0 were significantly different when mixed with roofs, with the average LST_0 of trees warmer than that of turfgrass (0.51°C and 0.05°C, respectively; $p < 0.0001$). Because per-pixel LST_0 was highly scattered, we used binned roof fraction values (averaged values using a bin width = 0.05, excluding bins containing fewer than 100 pixels) to assess the effect of increasing building density on LST_0. We observed a significant, positive effect of increasing building density on LST_0 for both turfgrass and tree ($p < 0.0001$). LST_0 appeared to increase nonlinearly, particularly for tree mixtures, with a steep rate of increase up to a roof fraction of about 0.2, and a gentler rate of increase thereafter (Fig. 2.9). We separately used a linear model (not shown) to quantitatively compare the effect of building density on trees versus turfgrass. We calculated that for every 10% increase in roof fraction, LST_0 of trees increased 0.12°C, while the LST_0 of turfgrass increased 0.05°C. We observed this linear model to be a good fit for increasing turfgrass LST_0 with roof fraction ($y = 0.82x – 0.17$, $R^2 = 0.80$).

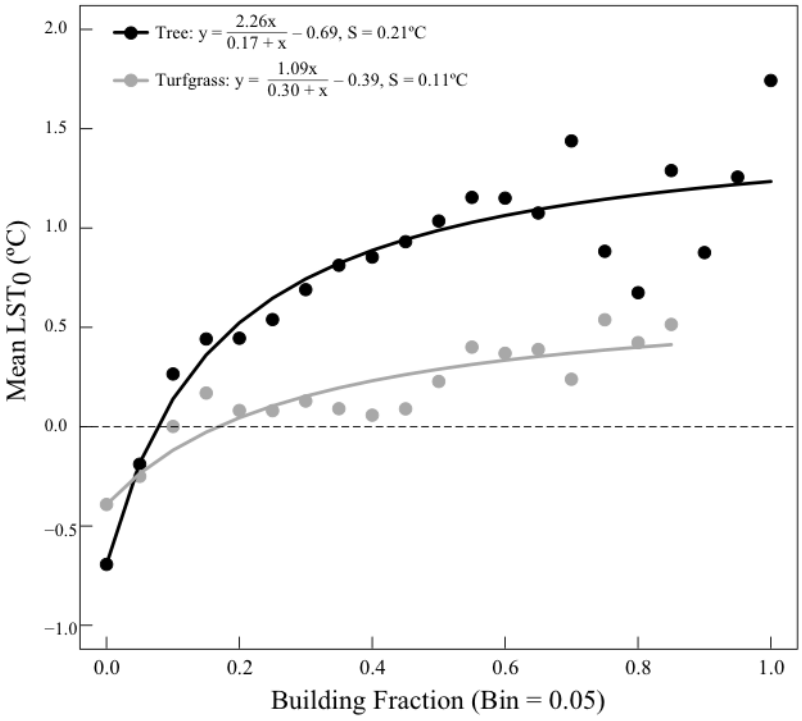

Figure 2.9. Changing LST_0 with building density, and nonlinear model with the standard error of the regression (S) as a measure of fit. Bins with fewer than 100 observations were excluded.

3.4.2. Vegetation management

Nearly all green spaces in Los Angeles require irrigation, however the amount and frequency of irrigation varies among property owners and managers. Therefore, rates of ET may not increase linearly with total green space. We evaluated the effect of vegetation management on LST_0 in two ways. First, we assessed vegetation fraction and LST_0 in relation to block group-level median income from the 2010 U.S. Census. While income itself is not a direct driver of vegetation function, higher income areas in arid cities tend to have more resources to devote to maintaining green space (Clarke et al., 2013; Schwarz et al., 2015). We calculated total vegetated area and mean LST_0 per block group. We found a significant, positive relationship between vegetated area and income in our study area ($p < 0.0001$,

$R^2 = 0.34$) (Fig. 2.10a). Although LST_0 is calculated independently of vegetation fraction, we observed a significant, negative relationship between LST_0 and income: for every $10,000 increase in median income, LST_0 decreased by 0.23°C, with LST_0 transitioning from positive to negative values for median income > $75,590 ($p < 0.0001$, $R^2 = 0.22$) (Fig. 2.10b).

Next, we investigated the relationship between LST_0 and water use data from 2007, which was a year of severe drought similar to our study period. We estimated the monthly irrigation rate from the difference in total residential water use between August, with high water use rates and matching the month of our imagery, and February, which had the lowest monthly rate, indicative of indoor water use (Chen et al., 2015). We aggregated our vegetation and LST_0 data into postal carrier routes (1,546 polygons with average size of 0.39 km^2) to match the water use data set. Because the water use data were for only residential customers, we excluded polygons that had large areas of non-residential water use, including golf courses, cemeteries, recreational fields, and university campuses. We first confirmed that irrigation requirements in 2007 were similar to our study year of 2014 by observing a strong linear relationship between 2007 outdoor water use levels and 2014 green vegetated fraction (Fig. 2.10c). We then calculated mean LST_0 per postal carrier route polygon. We observed a log-linear relationship between increasing irrigation (averaged values using a bin width = 2, excluding bins containing fewer than 3 polygon-level observations) and decreasing LST_0 values ($R^2 = 0.55$) (Fig. 2.10d).

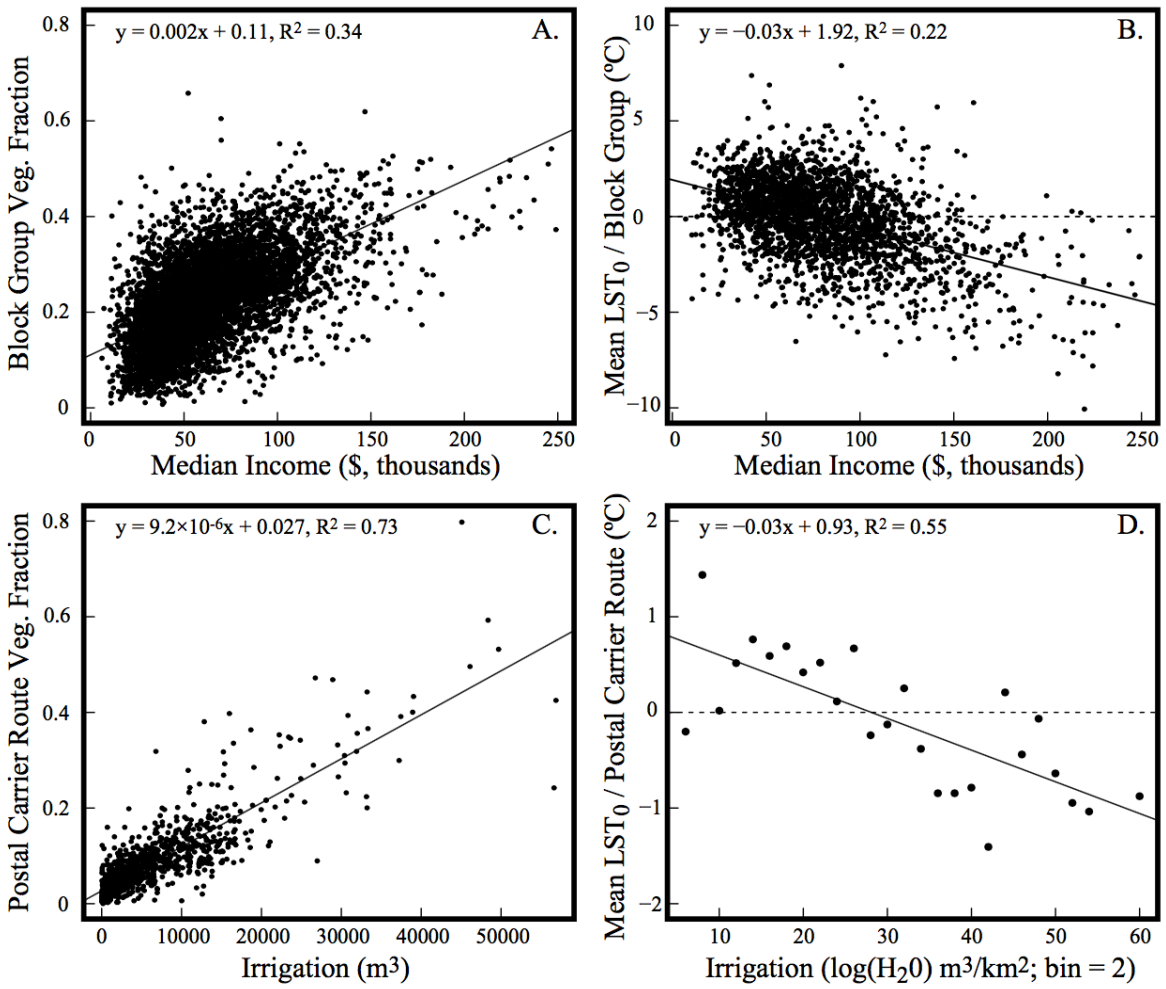

Figure 2.10. A.) Increasing vegetation fraction with increasing median income. B.) Decreasing LST_0 with increasing median income. C.) Linear relationship between vegetation cover during the 2014 data collection and 2007 water use data. D.) Log-linear relationship between LST_0 and binned monthly outdoor water use (per unit area). Bins with fewer than 3 observations were excluded.

4. Discussion

4.1. Effects of urban heterogeneity on measured LST at the city-scale

In this study, we separately quantified the key elements of urban heterogeneity that drive urban microclimates (plant functional types and non-vegetated materials), producing a first assessment of how vegetation LST varies across gradients of vegetation as well as non-

vegetated surfaces. This allowed us to quantify and map differences in vegetation LST independent of local variations in urban surface heterogeneity, and observe the effects of building density and irrigation on vegetation LST.

4.1.1. Effects of plant functional type

We found different plant functional types (tree and turfgrass) to have significantly different effects on measured LST, making their discrimination critical for modeling the effect of urban vegetation on its local environment. Our observations of mixed pixel LST were consistent with the overall negative relationships between vegetation fraction and LST that have been described in previous studies (Bowler et al., 2010; Jenerette et al., 2016; Zhou et al., 2017). However, by discriminating between plant functional types in this study, we found that turfgrass mixtures were consistently cooler than tree mixtures: a 10% increase in turfgrass fraction produced 1.6°C +/- 1.1°C more LST cooling than did a similar increase in tree fraction. Cooler turfgrass temperatures relative to tree temperatures persisted from relatively small to large vegetation fractions, over multiple spatial domains, and throughout most of the day.

Other studies have observed similar temperature relationships between urban trees and turfgrass. Quattrochi & Ridd (1998), using a high resolution airborne sensor over Salt Lake City, USA, found that residential lawns had a daytime thermal response < 70 W/m^2, while urban trees had a response of ~80 W/m^2. In Los Angeles, Crum & Jenerette (2017) using in situ measurements of LST found higher LST for tree canopies as compared to turfgrass for most of the diurnal cycle, which is consistent with our observations. Finally, in a comparison between Las Vegas and Phoenix, USA, Myint et al. (2015) observed similar

turfgrass LST-cover curves but significantly different tree LST-cover curves, suggesting that differences in plant functional type LST could depend on additional factors such as spatial arrangement. Trees can affect the temperature of the surrounding environment in both negative (shading and ET) and positive (reducing wind, longwave energy release, and ET of neighboring vegetation) ways (Litvak et al., 2014; Zhang et al., 2017). Across our study area, the balance of these contradictory effects resulted in a smaller reduction of LST for each incremental increase of tree cover compared to turfgrass. It is important to note that, as in other remote sensing studies, the nadir view angle of our imagery means that our LST measurements were dominated by the top of the tree canopy, which receives maximum solar radiation, and less influenced by the shaded subcanopy, which would have lower temperatures (Potchter et al., 2006).

Our results show that, in Los Angeles, building density may have been an important factor contributing to the observed higher LST in tree-covered versus turfgrass areas. We found building roof fraction to have more than twice as large a positive effect on tree LST_0 compared to turfgrass LST_0. This is consistent with previous reports of interactive LST effects between rooftops and tree canopies (Zhao et al., 2015; Feng & Myint, 2016). Buildings can warm tree canopies by blocking air circulation, or by heating air which can rise or advect into nearby canopies. Using a GIS layer to calculate per-pixel roof fraction may have enabled our observation of these interactive effects, since we could account for roof areas obscured beneath tree canopies. Conversely, buildings and turfgrass are adjacent and therefore their temperatures are more decoupled. In this study, the small, relatively linear increase in turfgrass LST_0 observed with increasing building fraction may also be influenced

by the positive relationship between roof area and roof LST that has been observed by others (Zhao et al., 2015).

Physiological and structural differences between trees and turfgrass would also have contributed to the higher LST of tree covered areas. Tree canopies are relatively tightly coupled to atmospheric water vapor, which increases stomatal sensitivity to high vapor pressure deficits (Kjelgren et al., 2000). Trees can also inhibit water loss from understory vegetation and soil beneath the canopy through shading (Litvak et al., 2014). Turfgrass is an aerodynamically smooth surface and is relatively less coupled to atmospheric water demand, resulting in lower stomatal sensitivity. Turfgrass also has less capability to cast shadows and reduce soil water loss, therefore soil evaporation continues to reduce LST even after turfgrass transpiration shuts down due to high vapor pressure deficit (Edmonson et al., 2016). This results in higher rates of ET for turfgrass compared to tree-covered areas, with one Los Angeles study observing turfgrass transpiration of 2–10 mm d–1 and tree transpiration of < 1 mm d–1 (Litvak et al., 2014). Furthermore, a relatively damped daytime variation of soil water evaporation compared to stomatally controlled plant transpiration would also be expected to minimize the daily range of LST in turfgrass relative to trees (Quattrochi & Ridd, 1998). Consistent with this, we observed that turfgrass LST varied the least of all classes, with a daytime range of 9.7°C, while trees varied by 13.6°C.

Finally, trees and turfgrass express water stress differently in the VSWIR and thermal ranges. Turfgrass expressions of water stress are well-coupled between the VSWIR and the thermal. Well-irrigated turfgrass requires around 2.5 cm of water per week and will remain green and cool as it continues to transpire (Milesi et al., 2005). Poorly-irrigated turfgrass will begin to transition to NPV if water inputs are withheld for as little as 6 weeks, which will

also coincide with a rise in LST as transpiration shuts down (Kaufmann, 1994). Tree expressions of water stress in the VSWIR and thermal are less coupled. While well-watered trees remain green and cool, poorly-irrigated trees have been shown to express stress through elevated LST, while overall greenness can be less affected (Zarco-Tejada et al., 2011; Sims et al., 2014). The implications for studies that combine VSWIR and thermal imagery to assess urban vegetation, such as ours, are that areas identified as turfgrass are almost certainly being irrigated, whereas areas identified as tree-covered may be experiencing a comparatively greater range of water availability and stress. This difference in stress response between turfgrass and trees could be of significance for assessments of the urban surface energy balance as well as human thermal comfort studies in arid urban environments.

4.1.2. Effects of non-vegetated material

While vegetation fraction is a primary driver of LST variability in thermal imagery, non-vegetated materials are known to have a significant effect on mixed pixel LST, especially when they occur at higher fractions (Yuan & Bauer, 2007; Weng, 2009). In our study, we observed significant differences between the LST effects of impervious surfaces and NPV, with observed daytime patterns for LST-cover curve slopes of different mixtures likely driven more by the greater daily LST ranges expressed by non-vegetated materials (15.6°C to 17.7°C) compared to that of vegetation.

We observed a greater influence of NPV (larger slopes) on mixed pixel LST compared to impervious surfaces. However, tree and turfgrass mixtures with NPV did not exhibit significantly different slopes. This may have been because NPV itself is indicative of vegetation condition, with increasing NPV fractions potentially indicating degrees of

vegetation senescence. Roberts et al. (2012) observed LST variation in relation to NPV fraction, which they hypothesized to be due to changing vegetation function and water stress with senescence. As trees and turfgrass transition from healthy to senesced, transpiration may have been minimized such that their LST values became more similar, reflective of having similar composition of senesced leaf material, compared to the larger differences observed due to contrasting ET rates in active, healthy trees and turfgrass.

In contrast to NPV, in mixtures with impervious surfaces, tree and turfgrass LST-cover curves showed significantly different slopes. Paved surfaces interact differently with trees compared to turfgrass. Paved surfaces surrounding trees can increase subcanopy LST and air temperatures, trap or decrease soil moisture, and increase longwave and sensible heat inputs into the canopy (Souch & Souch, 1993; Kjelgren & Montague, 1998; Friedl, 2002; Chen et al., 2017). These effects result largely because trees can occupy the same vertical column of space as pavement. Conversely, while turfgrass and impervious surfaces occur nearby one another, both are of similar height and therefore each lacks a view factor for direct radiative transfer with the other. For this reason, the interactive effects between turfgrass and impervious surfaces tend to be limited to advection, which influences turfgrass ET by altering local vapor pressure deficits, as opposed to direct radiative exchanges (Oke, 1979; Armson et al., 2012).

Interestingly, we observed turfgrass-impervious mixtures to be the least linear of any combination, with a steeper decline at around 50% turfgrass fraction. This is similar to observations made by Myint et al. (2013), who noted a steeper slope for turfgrass fractions above 40% and concluded that turfgrass fractions < 40% are not effective in lowering LST. We hypothesize that a bimodal transition between residential lawns (mapped as small

turfgrass pixel fractions), and larger, public green spaces (mapped as large pixel fractions along greenspace edges and pure turfgrass pixels in the greenspace center), may result in the observed LST nonlinearity. Energetically, small patches of turfgrass have higher ET potential than large patches, because small patches are situated in more heterogeneous environments and therefore subject to more advection of warm, dry air from nearby impervious surfaces (Oke, 1988; Chow et al., 2014). In dry climates, increased ET potential could more rapidly deplete soil water and induce stomatal closure earlier in the day, leading to higher LST. At the same time, large turfgrass patches in Los Angeles tend to be intensively managed public spaces such as parks, cemeteries, or golf courses. Their more intensive management and irrigation regime may produce healthier vegetation, higher ET, and cooler temperatures compared to residential lawns.

4.2. Mapping drivers of vegetation LST

We used a "big data" approach to assess vegetation LST: with 1.7 million pixels, each of a different compositional and fractional mix, we derived broad LST patterns across gradients of land cover heterogeneity to remove its dominant, first-order LST effects. This opens the possibility of examining any additional drivers of LST variability for which we have spatial data. Studies have identified several drivers of urban vegetation LST, including but not limited to plant species, canopy structure, urban canyon geometry, irrigation regime, vegetation spatial configuration, and wind (Leuzinger et al., 2010; McCarthy & Pataki 2010; Litvak et al., 2014; Zhao et al., 2015; Gillner et al., 2016; Zhou et al., 2017). Across a city, these drivers as well as additional factors have significant effects on urban LST. While this

study did not investigate the contributing role of each driver, their combined effects contribute to the LST variability shown in Figures 2.5, 2.6, 2.8, and 2.10.

We examined the effects of building density (Sect. 4.1.1.) and vegetation management on vegetation LST. Variability in residential vegetation management is difficult to observe at city-scales. One approach is to investigate the relationship between personal income and local temperatures (Jenerette et al., 2013; Schwarz et al., 2015; Roberts et al., 2017). While income is not a direct driver of vegetation function, higher income areas have more vegetation, especially in arid cities, which also tends to be better maintained because residents have more resources to devote to management (Clarke et al., 2013; Schwarz et al. 2015). We observed a significant, positive relationship between vegetated area and income in our study area (R^2 = 0.34), which is consistent with other studies in Los Angeles (Mini et al., 2014; Tayyebi & Jenerette, 2016). More green space as well as improved vegetation management reduces local temperatures. For example, Jenerette et al. (2007) found that a $10,000 increase in median income was associated with a decrease in temperature of 0.28°C in Phoenix. We observed a similar decrease in LST_0, finding that for every $10,000 increase in median income, LST_0 decreased 0.23°C. Importantly, in our study LST_0 was independent of both vegetation fractional cover and plant functional type, meaning that the LST decrease was directly linked to differences in irrigation and associated latent heat fluxes, rather than the amount or type of green space. This was confirmed in part by our observation of significant LST_0 cooling as irrigation inputs increased.

4.3. Methodological considerations

4.3.1. Improved sub-pixel analysis for urban environments

With a study area of 4,466 km^2, this study demonstrates that a single, small spectral library is capable of accurately estimating sub-pixel fractions across a very large spatial extent and multiple flightlines. At a spatial resolution (36 m) similar to Landsat (30 m), this study shows the importance of additional spectral information for sub-pixel urban mapping, which decreased estimates of the majority class (impervious surface) by nearly 15% and increased detection of small patches of cover, consistent with MacLachlan et al. (2017). Additionally, this study contributes to the growing body of work establishing the importance of high spectral resolution imagery for estimating urban cover fractions beyond the VIS model, including different plant functional types (Roberts et al., 2012; Okujeni et al., 2013; Okujeni et al., 2015; Wetherley et al., 2017). With spaceborne hyperspectral missions planned for the near future, being able to characterize functionally uniform sub-pixel cover at resolutions typical of a spaceborne sensor will improve our ability to study urban environments globally.

Trees and turfgrass are the two primary plant functional types in North American cities. Their differences in water use, stress response, and shading effects result in contrasting impacts on local energy and water fluxes, making their discrimination important for characterizing urban environments (Grimmond et al., 2011; Peters et al., 2011). While species-level spectral differences exist within both types, when grouped into broad functional categories the primary distinguishing spectral feature between them is overall brightness: trees, due to their greater leaf area and more complex canopy, reflect less energy than turfgrass. In our spectral library, tree spectra were, on average, 49% as bright as turfgrass

spectra, with this difference remaining relatively consistent through the visible (53%), NIR (50%), near short-wave (44%), and far short-wave (50%) parts of the spectrum.

Because brightness is a key difference between trees and turfgrass, limiting the corrective MESMA shade factor to 20% proved to be key for separating the two plant functional types. The MESMA shade factor is used to account for brightness differences between library EMs and measured spectra (Dennison & Roberts, 2003). Typically, this factor is assigned a large value, ranging from 50%–80%, which gives MESMA greater flexibility for modeling a dark pixel with a bright EM (Powell et al., 2007; Powell 2011; Dudley et al., 2015; Liu & Yang, 2015). However, when brightness itself is a key discriminating factor this can lead to confusion—in the case of trees and turfgrass, with a large enough shade factor MESMA could disregard brightness differences to select a bright turfgrass EM to model a dark tree canopy in an image if its spectral features were the best fit. The tradeoff of using a smaller shade parameter is that more pixels remain unclassified or a larger spectral library may be required to account for brightness variation in an image.

4.3.2. Challenges and opportunities when using airborne thermal imagery

Several of the challenges in calculating LST_0 in this study stemmed from the particularities of airborne imagery. One such issue was viewing geometry effects on measured LST. Viewing geometry effects in urban thermal imagery depend on the location of the sensor relative to solar position as well as urban surface morphology (Roth et al., 1989). Viewing angles that deviate from nadir increase the amount of vertical surface that is visible to the sensor, which has been observed to affect LST measurements from off-nadir sensors in the range of 5°C–10°C in some urban areas (Lagouarde et al., 2004; Trigo et al., 2008;

Bechtel et al., 2012). Although MASTER flightlines were imaged with a nadir view orientation, surfaces in the forwardscattering view of each flightline were ~2°C cooler than surfaces in the nadir view, while backscattering surfaces were < 1°C warmer. This is likely because the 45° viewing angle of MASTER was enough to detect the effects of urban thermal anisotropy along flightline edges. Urban thermal anisotropy results from urban structural heterogeneity, such that shadows and different angles of solar exposure produce LST variability (Voogt & Oke, 1998; Voogt, 2008). From the perspective of the MASTER imager, shadows in the forwardscattering view reduced LST, whereas high solar exposure on south-facing vertical walls in the backscattering view resulted in warmer LST. The observed temperature differences between forwardscattering and backscattering views (above), shows that shadowing had the stronger effect on LST. However, the slopes of LST-cover curves, and therefore the relationships between surface cover and LST observed here, did not significantly differ by viewing geometry. We also removed the areas most affected by viewing geometry from our analysis by subsetting each MASTER swath (~40 km wide) to the swath of the corresponding nadir-view AVIRIS flightline (~12 km wide) before calculating LST_0.

Another challenge of using a large airborne thermal dataset involved accounting for temporal variation. Solar angle variation affects LST diurnally, as observed in our dataset, as well as seasonally. Temporal normalization between thermal images collected at different times is of interest to compare thermal measurements (Li et al., 2013). One temporal normalization method models the diurnal temperature cycle to estimate LST based on a thermal image (Göttsche & Oleson, 2001). Another method, specific to airborne imagery, uses flightline sidelap areas to calibrate LST between adjacent flightlines (Tayyebi &

Jenerette, 2016); however, our results showed that viewing geometry may affect the accuracy of this correction method. In this study, we used 9 MASTER flightlines collected over a 5.7-hour window before and after solar noon. By processing each using per-flightline LST-cover slopes, we were able produce a normally distributed LST_0 map of the study area. This indicates that our method is robust to temporal LST variation and could provide an alternative technique for standardizing LST between multiple thermal images.

Thermal imagery, particularly over urban areas, can also be subject to errors arising from TES. These errors tend to fall into one of two categories, both of which we attempted to minimize in our study design (Gillespie et al., 1998). First, systematic errors across the imagery can result from improper atmospheric calibration. We attempted to minimize this error and ensure a consistent retrieval across all flightlines by using imagery collected during a single day. Second, errors can result if the ε_{min} of a material and its MMD are not well-characterized by the empirically-derived relationship between them used in the TES algorithm. While this relationship describes many natural materials, including vegetation, soil, rock, and water, it does not accurately characterize materials having both low spectral contrast and low emissivity, which is typical of some metals such as aluminum (Kotthaus et al., 2014). Sobrino et al. (2012) found that the ε_{min}-MMD relationship can describe many common urban surfaces that have low MMD and high emissivity, including concretes, construction materials, road asphalt, and tar, concluding that TES can retrieve accurate LST values for these materials. We limited the EMs representing our impervious surface class to these paving materials. This left pixels containing metallic or other problematic surfaces unclassified, thereby excluding them from our LST-cover analysis.

There are a few other ways our results may have been influenced by specific characteristics of the MASTER dataset. First, while airborne imagery allowed us to explore hourly daytime LST change, the pattern of flightline collection prevents us from completely disentangling diurnal effects from the influence of the coastal-interior climatic gradient, although our in situ measurements provided confidence that we observed diurnal patterns between our flightlines. Additionally, flightline orientation likely influenced our results. Each LST-cover curve depended upon the LST variability captured within a specific flightline, and this variability could have been very different had flightlines been acquired using a coast-to-interior orientation rather than one approximately parallel to the coast. Finally, the spatial resolution of thermal imagery has been shown to affect measurements of vegetation cooling, which we did not explore here (Weng et al., 2004; Weng, 2009; Zhou et al., 2017). Using satellite imagery with a larger swath would address several of these issues. The proposed NASA HyspIRI Satellite, which would combine an imaging spectrometer with a thermal imager, would produce ideal imagery for a systematic assessment of city-scale urban vegetation LST.

5. Conclusion

In this study, we set out to answer three questions. First, we asked what is the urban plant and material variability of the megacity of Los Angeles. We found Los Angeles to be dominated by impervious surfaces (59%) with 24% vegetation cover. Sub-pixel estimation of cover was critical for quantifying non-impervious classes, increasing estimates of turfgrass (1.7%), tree (6.3%), commercial roof (3.2%), NPV (2.2%), and soil (0.9%) while decreasing estimates of impervious cover by 14.3%. Second, we asked how plant functional type and

urban material type affect LST. We found that plant functional type (turfgrass and tree) and non-vegetated surfaces (impervious and NPV) had significantly different effects on LST. In particular, trees were consistently warmer than turfgrass, and the two functional type LST-cover curves exhibited significantly different slopes when mixed with impervious surfaces. Finally, we asked how vegetation LST varied across our megacity study area. We found large, neighborhood-scale patches of warm and cool vegetation, with detectible effects related to building density and vegetation management. Together, these findings suggest that it is possible to examine vegetation LST in highly mixed urban environments and quantify city-scale effects of environmental drivers that have previously been obscured by urban surface heterogeneity.

Our study results provide several avenues for future work. Primarily, quantifying the effects of additional spatial drivers on city-scale LST_0, such as tree species or urban canyon geometry, will be a critical step towards isolating the thermal signals that indicate vegetation stress in mixed LST pixels. In this context, further analysis of the relationship between building density and tree LST could be enhanced by incorporating height information. We expect that the heights of trees and buildings relative to each other will significantly affect the observed relationship. Additionally, while our study examined LST changes within a 5.7-hour window, understanding the dynamics of LST change among different materials and plant types across the full diurnal cycle would be of value for studies of urban microclimates, the urban heat island, and human thermal comfort.

Cities are some of the most climatologically complex environments on the planet, with diverse microclimates produced by material, vegetation, and structural heterogeneity. In situ studies and urban climate models have advanced our understanding to a great degree, yet

the challenge remains to unlock the potential for remote sensing to disentangle the drivers of urban climate variability at the city-scale. Doing so at the resolution of near-future orbital sensors, which will allow for repeat assessment of urban LST across multiple cities, seasons, and climates, will ultimately help to develop a deeper, quantitative understanding of the functioning urban environment.

Acknowledgements

This research was supported by the NASA Earth and Space Science Fellowship Program (17-EARTH17R-68); and by the Belgian Science Policy Office in the framework of the STEREO III Program—Project UrbanEARS (SR/00/307). We thank the Jet Propulsion Laboratory for providing all imagery used in this analysis and the County of Los Angeles for providing additional GIS data.

Chapter 3

Urban Microclimate Variability of a Large, Semi-Arid Metropolitan Area

With Joseph P. McFadden, Dar A. Roberts, C. Naomi Tague, Dale A. Quattrochi and Charles Jones

1. Introduction

A major challenge in the field of urban climate is that fluxes of heat and moisture can have large amounts of temporal and spatial variability across a city, complicating city-scale assessment. Remote sensing can capture city-wide surface variability for a single moment in time, and advances in remote sensing are improving our ability to measure urban surface materials and structure, quantifying urban heterogeneity in greater detail and across larger domains (Jensen, 2009; National Academy of Sciences, 2018). Conversely, urban energy balance models can simulate hourly time series of surface fluxes for local environments at the neighborhood scale (Grimmond et al., 2010). This creates an opportunity to couple the relative spatial and temporal strengths of current imaging and urban energy balance modeling techniques to quantify dynamics across a complete urban system.

The urban energy balance can be calculated as:

$$Q + F = H + LE + \Delta S \quad [3.1]$$

Where Q is net radiation, F is anthropogenic heat flux resulting from the burning of fuels, H is sensible heat, LE is latent heat, and ΔS is net heat storage within the urban surface (Oke, 1987). Urban microclimates result from differences in the amount of available energy (Q + F – ΔS) and the partitioning of that energy into turbulent fluxes (H and LE) (Oke, 1988; Roberts et al., 2006). Energy partitioning depends on the amount of available moisture, and is therefore affected by vegetation transpiration and, by extension, vegetation stress (Soer, 1980; Dimoudi & Nikolopoulou, 2003). Assessment of urban microclimates therefore must account for the amount and condition of vegetation in addition to properties of the built environment and other physical factors that influence the surface energy budget.

Microclimatic differences across a city are driven in part by surface diversity, which

can be quantified by remote sensing in several ways (Chapin et al., 2011; Esau & Lyons, 2002; Weng et al., 2018). For example, imagery can be used to estimate the proportion of energy reflected from the surface (albedo), and therefore the magnitude of Q (Liang et al., 2010). Remote sensing can also help to quantify local material diversity. Recent advances in hyperspectral imagery, which captures tens or hundreds of very narrow bands across the electromagnetic spectrum, have improved our ability to classify landcover based on relatively fine spectral features (Herold et al., 2003; Franke et al., 2009). Several orbital hyperspectral sensors are planned for the near future, which will expand its application to cities globally (Guanter et al., 2015; Candela et al., 2016; National Academy of Sciences, 2018).

High spectral resolution can also be leveraged to derive detailed landcover at sub-pixel scales, including vegetation types (turfgrass and trees), as well as paved ground, roofs, bare soil, and senesced vegetation (Roberts et al., 2012; Okujeni et al., 2013; Okujeni et al., 2015; Wetherley et al., 2017; Wetherley et al., 2018). A common technique for deriving sub-pixel cover is spectral mixture analysis, which assumes that measured reflectance is a linear combination of the reflectances from all surfaces within a pixel, weighted by their relative pixel fraction (Settle & Drake, 1993). Sub-pixel estimation is critical for mapping urban vegetation, which can exist in relatively small patches (e.g., street trees); depending on spatial resolution, these may not be detected at the scale of a full pixel (Ferrato & Forsythe, 2013; Nordbo et al., 2015). At the same time, the ability to discriminate plant type is important for isolating characteristic transpiration responses to the surrounding environment (Peters et al., 2011).

The relative proportions of local land cover types, and particularly the proportion of vegetated to non-vegetated area, strongly influence local energy partitioning (Grimmond et

al., 2010). Partitioning is further affected by surface roughness and aerodynamic resistance, which impact evaporation as well as local vegetation conditions (Penman, 1948; Monteith, 1965; Christen & Vogt, 2004). Urban morphology, including vertical structure such as building and tree heights, can be measured using Light Detection and Ranging (LiDAR), which is an active remote sensing technique that emits laser pulses and times their return to derive object heights (Priestnall et al., 2000). Airborne-based LiDAR has been used to quantify the 3D surface for cities around the world, although the availability of these datasets can be limited due to the high costs of acquisition (www.citygml.org). It has also been used in combination with hyperspectral imagery for various urban applications, including mapping urban tree species and leaf area index, classifying urban surface cover, and monitoring urban infrastructure (Chen et al., 2009; Brook et al., 2010; Alonzo et al., 2014; Alonzo et al., 2015).

Albedo, land cover type and fraction, and vertical structure are important parameters for describing a physical site in regards to its local energy budget (Grimmond et al., 2010). As such, they constitute relatively common inputs into neighborhood scale (10^2 – 10^4 m) urban energy balance models, yet they can be quantified for much larger domain (Grimmond et al., 2011). This raises the possibility of expanding the application of local-scale urban flux analyses to that of a larger metropolitan area. However, this would require similarly-scaled estimates of meteorology as well as surface moisture to assess LE fluxes. Biological controls on LE (i.e., transpiration) and its response to local soil moisture deficit, wind, heat, vapor pressure deficit, and/or light intensity, must be similarly assessed at a large scale (Chapin et al., 2011).

Irrigation is another critical variable, as it strongly influences local soil moisture levels, yet it is difficult to quantify across large domains as its application may be influenced

by spatially variable management decisions, property owner income, water availability, the mode of irrigation used, conservation policies, or plant water needs (Grimmond & Oke, 1999; MacDonald et al., 2010; Peters & McFadden, 2010; DeOreo et al., 2011; Järvi et al., 2011; Pataki et al., 2011; Clarke et al., 2013; Schwarz et al., 2015). Several methodologies have been developed to estimate urban outdoor water use, including assuming minimal levels of soil moisture, tying irrigation to potential evapotranspiration, or developing empirical relationships between measured water use and spatially distributed variables (Xiao et al., 2007; Järvi et al., 2011; Vahmani and Hogue, 2014). Remote sensing can inform this last category by providing information about the spatial distribution of irrigated vegetation. In this vein, studies have estimated urban water use based on remote sensing observations of NDVI, plant type classification, or vegetation fraction (Keith et al., 2002; Nouri et al., 2013; Mini et al., 2014; Chen et al., 2015)

Due to the high spatial variability of surface types and structures across a city, and the difficulty of producing detailed maps of parameters that govern heat and moisture fluxes, many urban energy balance models are designed to run at the neighborhood scale. This roughly corresponds to the size of a micrometeorological flux tower footprint, which can provide highly localized meteorological data and validation of estimated fluxes (Järvi et al., 2011). Neighborhood scale studies can also be augmented with in situ observations of additional variables, such as soil moisture. However, the results of these studies are site-specific, making them difficult to extrapolate to other sites and limiting their ability to untangle the complicated individual and interactive effects of biology, climate, and human agency on urban LE variability.

In this study, we used several large datasets to conduct a spatially extensive

investigation of energy partitioning in the megacity of Los Angeles, with the goal of teasing apart the relative contributions of landcover, climate, and irrigation. We used remote sensing datasets to derive a highly detailed surface parameterization for the study area, including fractional material cover, albedo, and vertical surface structure. We combined this with estimates of irrigation derived from a spatially explicit water use dataset, as well as high resolution meteorology derived from the Weather Research and Forecasting (WRF) model and local station data (Skamarock & Klemp, 2008). We used these data layers as inputs to the Surface Urban Energy and Water Balance Scheme (SUEWS) to derive temporally-detailed estimates of local moisture and fluxes, which we assessed using thermal imagery and field data (Järvi et al., 2011; Ward et al., 2017). We then used this rich dataset to examine the spatial and temporal drivers of flux variability across the Los Angeles metropolitan region. Specifically, we asked the following questions:

1. How do urban material composition and vertical structure vary across the Los Angeles metropolitan region?
2. How do surface cover characteristics, including landcover and irrigation, affect turbulent energy fluxes?
3. How does regional climate drive spatial and temporal latent heat flux variability?

2. Methods

2.1 Study Area

The study area included 2,123 km^2 of urbanized land located within Los Angeles County in Southern California, including the City of Los Angeles and 79 surrounding communities and urbanized suburbs that together comprise the Los Angeles metropolitan

area (referred to as Los Angeles for the remainder of this manuscript). Los Angeles is a densely populated American megacity with a population greater than 10 million (U.S. Census Bureau, 2012). It is composed of different types of urban development, including a primary downtown core, commercial centers, industrial zones, and residential neighborhoods of various densities. Urban materials are consistent with other North American cities, including different impervious surfaces such as asphalt, concrete, and various roofing materials. Building sizes range from small one-story structures to downtown skyscrapers. Los Angeles vegetation consists of around 200 tree species as well as large expanses of turfgrass lawns, recreational fields, and large golf courses (Clarke et al., 2013). Vegetation is unevenly distributed across the area, with neighborhoods varying in their canopy cover by 7-37% (McPherson et al., 2011).

The adjacency of Los Angeles to the Pacific coast produces a strong coastal-interior climatological gradient. Northern parts of the study area, including parts of the San Fernando Valley, are separated from the coast by both distance as well as a low mountain range, and thus have drier and hotter summertime conditions relative to the more coastal south. In general, Los Angeles experiences a seasonal Mediterranean climate, with warm dry summers and cool wet winters. In a typical year, Los Angeles receives an average of 37.9 cm of precipitation, mostly in the winter (U.S. Climate Reference Network (USCRN): Diamond et al., 2013). Summer weather is typically hot and dry, and during the period of this study (August 2014) Los Angeles was in the middle of an extreme and extended drought, estimated to be one of the most severe experienced in the area in ~1200 years (Griffin & Anchukaitis, 2014; Asner et al., 2016). As a result, precipitation in the preceding year was minimal and virtually all areas of green vegetation required consistent irrigation.

2.2 Remote Sensing Data

2.2.1 Hyperspectral Imagery

Urban surface characteristics were derived from several remote sensing datasets. Landcover was mapped using hyperspectral imagery from the Airborne Visible Infrared Imaging Spectrometer (AVIRIS), which was flown over the study area on August 26, 2014 by NASA's Hyperspectral Infrared Imager (HyspIRI) Airborne Campaign. AVIRIS measures 224 narrow bands between 0.38 and 2.5 μm (Green et al., 1998). A total of 7 flightlines on a northwest-southeast orientation were acquired to cover the complete study area. The imagery was first processed by the NASA Jet Propulsion Laboratory (JPL) to produce reflectance (Thompson et al., 2015). We then resampled it to a spatial resolution of 36 m and applied additional spectral and spatial corrections, following Wetherley et al. (2018).

Spectral mixture analysis was used to derive sub-pixel landcover classes of turfgrass, tree, soil, senesced vegetation, paved ground, and commercial roofs for the complete study area. Specifically, we used Multiple Endmember Spectral Mixture Analysis (MESMA: Roberts et a., 1998), a type of spectral mixture analysis that estimates fractions for each class based on a library of spectral endmembers (Somers et al., 2016). MESMA allows different classes to be represented by more than one endmember, and allows the number of endmembers used to model each pixel to vary. This gives MESMA greater flexibility for estimating fractional cover in a scene with great diversity, and has therefore been applied to imagery of several global cities (Rashed et al., 2003; Powell et al., 2007; Roberts et al., 2012; Wu et al., 2014; Roberts et al., 2017).

Fractional estimates were validated using a combination of simulated mixtures and within-image validation areas, and found to be well-characterized for the Los Angeles study

area (Wetherley et al., 2018). However, because only commercial roofs were mapped, we used a 2014 GIS layer of Los Angeles building footprints (Los Angeles County GIS, 2014) to incorporate non-commercial structures such as residential buildings. The building footprints were used to calculate per-pixel building fraction, which was then incorporated into the fractional map by adjusting per-pixel roof and (if necessary) impervious surface fractions to ensure that fractions within each pixel summed to one.

Hyperspectral imagery was also used to derive per-pixel directional albedo (Roberts et al., 2004; Roberts et al., 2012; Shivers et al., in Review). Directional albedo is different from true albedo because it assumes all surfaces to be Lambertian. We used MODTRAN 4.3 to simulate downwelling irradiance for the specific date, location, and time of each flightline (Berk et al., 2005). Atmospheres were generated using a midlatitude summer profile, assuming a surface albedo of 0.25, 1 cm of water vapor, and an air temperature that ranged from 300.9 K to 303.02 K depending on the time of imaging. Downwelling irradiance was multiplied by AVIRIS reflectance across all wavelengths to calculate total reflected irradiance (0.3 – 2.5 μm). Albedo was calculated as the ratio of reflected irradiance to total downwelling radiance.

Retrieved values for a variety of urban targets were assessed by comparing them to published urban landcover albedo values for the neighboring City of Santa Barbara (Roberts et al., 2012). Values for the four southernmost flightlines were determined to contain similar albedo values to the published values. The three northernmost flightlines contained anomalously low values, which we determined to be due to anomalously low reflectances retrieved by JPL. We investigated this by examining overlapping pairs of correct and low albedo values for 21 targets located within a flightline sidelap area. Target albedos in the

correct flightline, ranging from 0.03 to 0.52, were significantly different from those in the dark flightline, which ranged from 0.013 to 0.43 ($p < 0.001$). A strong linear relationship was observed between the two, with $y = 1.11x + 0.02$ ($R^2 = 0.99$). This was used to correct the dark flightlines, producing a consistent albedo retrieval across the scene.

2.2.2 LiDAR Imagery

A high-resolution LiDAR raster (1 m) and a land cover classification map (Los Angeles Region Imagery Acquisition Consortium: LARIAC, 2016) were used to quantify vertical surface structure across Los Angeles. The map had an overall classification accuracy of 95%, while the LiDAR image had a locational accuracy of ±0.61 m. Tree and building classes both had an accuracy of >97% by area. We used the classified image to produce a high-resolution mask for trees and buildings, with edges eroded inward by 20% to remove edge pixels. We used a 5×5 pixel peak filter to remove gaps within the masked areas and derive the final heights for trees and buildings. We retained all values above a 2 m threshold, representing > 99% of the height data. In addition to height measurements, aerodynamic roughness length and zero-plane displacement were calculated across the scene using the full LiDAR dataset and the Urban Model Environment Planner (UMEP) tool (Lindberg et al., 2018). Roughness calculations were based on the methodology recommended by Kanda et al. (2013), which calculates local surface roughness by using maximum building height, the standard deviation of building height, average building height, frontal area index, and ground area. Tree heights were included in the calculation, as recommended by Kent et al. (2017).

2.2.3 Thermal Imagery

Land surface temperature (LST) was measured for the entire study area by the MODIS-ASTER Airborne Simulator (MASTER), as part of the HyspIRI Airborne Campaign (Hook et al., 2001). The full study area was imaged over a 5.6-hour period (10:20 – 16:00 PDT), thus capturing elements of both the spatial and temporal LST variability of Los Angeles (Wetherley et al., 2018). Meteorological conditions consisted of clear skies with air temperature peaking at 30.0°C, as calculated from the mean of 14 USCRN stations located within and throughout the study area. MASTER measured 5 bands of emissivity at 36 m spatial resolution. Thermal imagery was processed by JPL to retrieve per-pixel LST using temperature-emissivity separation (TES) (Gillespie et al., 1998). Overall accuracy was reported by the Ames Research Center to be ≤0.33 K, with per-band precisions ranging from 0.13 to 0.74 K (Jeffrey Myers, personal communication).

2.3 Additional Data

2.3.1 Water Use

External irrigation was estimated from a 2007 dataset of Los Angeles residential water use (Los Angeles Department of Water and Power; Mini et al., 2014), aggregated to sub-neighborhood scale postal carrier route polygons (1,546 polygons with average size of 0.39 km^2) (Chen et al., 2015). We selected the year 2007 from the available water use data (2000-2010) because it was characterized by a severe drought, which we assumed to best approximate the dry conditions of our August 2014 study period. Outdoor water use (m^3) was estimated from the difference in total single-family residential water use in August (a dry month and matching the month of our study) and February (the month with lowest water use).

Estimated monthly outdoor water use was linearly correlated with postal carrier route polygon vegetation fraction ($R^2 = 0.73$) by Wetherley et al. (2018):

$$f_v = 9.2 \times 10^{-4} w + 2.7 \quad [3.2]$$

Where f_v is fractional vegetation cover (0 – 100) and w is the estimated outdoor water use for one month in m^3. Water use for each grid cell was calculated by rearranging Eq. 3.2 to solve for w based on grid cell f_v.

2.3.2 Field Data

Soil moisture and LST were measured in situ for two turfgrass field sites in Santa Barbara, CA (located at 34.45°N, 119.75°W and 34.42°N, 119.86°W) on August 24 and 29, 2014, where it was possible to synchronize the timing of collections with MASTER airborne acquisitions. Although the field sites were not located within the Los Angeles study area, Santa Barbara is situated at a similar latitude and climate, with conditions on the days of collection close to that of Los Angeles on the day of imaging. A total of 40 individual measurements were collected across the two sites. Point measurements were made every 25 m along 5 transects (100 m), each set 25 m apart. LST was measured using an Apogee IRTS-P Precision Infrared Temperature Sensor, which measures between 6-14 μm (Logan, UT). Temperatures were corrected for longwave radiation using an assumed turfgrass emissivity of 0.95 (Oke, 1987) and measurements of downwelling longwave radiation collected by a Kipp & Zonen CNR1, located 11 km and 2 km from each collection site. The CNR1 measures between 5-50 μm, which is a larger proportion of the spectrum than the IRTS-P, so longwave measurements were scaled by the proportion of thermal radiation emitted between 6-14 μm using the method described by Wetherley et al. (2018). Soil moisture in the top 50 mm of soil

was calculated using a soil moisture probe (ThetaProbe type ML2x, Delta-T Devices, Cambridge, England) to measure percent volumetric near-surface soil moisture.

2.4 Model simulations

We used the Surface Urban Energy and Water Balance Scheme (SUEWS) to assess fluxes across our study area (Järvi et al., 2011; Ward et al., 2017). SUEWS is a neighborhood-scale model that produces energy flux estimates at a 5-minute time step. We selected this model for several reasons. First, SUEWS has been applied to the Los Angeles area and validated against Los Angeles flux tower data, with published parameter values based on local datasets (Järvi et al., 2011). Second, required inputs for characterizing landcover in SUEWS, including albedo, surface cover types, cover fractions, and vertical structure, can be extracted from remote sensing datasets as described in Sections 2.2.1 and 2.2.2. Third, the model generates flux estimates based on relatively common meteorological inputs, including air temperature, relative humidity, pressure, precipitation, shortwave radiation, and wind. Several empirically- and physically-derived sub-models are then used to calculate net radiation, anthropogenic heat flux, storage heat flux, turbulent fluxes, and water balance factors (Grimmond et al., 1986; Grimmond & Oke, 1991; Grimmond et al., 1991; Grimmond & Oke, 1999; Offerle et al., 2003; Loridan et al., 2010). This makes SUEWS a more computationally efficient model in comparison to other energy balance models that require more complicated parameterization (Grimmond et al., 2010).

Computational efficiency is critical for application to a large domain. We divided the study area into 2,123 grids, each 1 km^2 (Fig. 3.1). We calculated surface parameter values for each grid cell using the datasets and methodologies described above. Grid cell fractional

cover of tree, turfgrass, buildings, ground impervious, and soil, as well as albedo, were derived from the hyperspectral datasets. Estimated monthly grid cell water use, based on total vegetated area in the grid cell (turfgrass plus tree fraction), was divided by 31 to obtain a daily amount, and distributed over the diurnal cycle at a 5-minute time step using a profile of hourly watering behavior based on a water use survey of California homeowners (DeOreo et al., 2011). Vertical structure metrics, including mean building and tree height, aerodynamic roughness length, and zero plane displacement, were extracted from the LiDAR imagery. Grid cell elevation was derived from a U.S.G.S. National Elevation dataset and population from a U.S. Census Bureau Census Tract GIS layer (U.S. Census Bureau, 2010; U.S. Geological Survey, 2013).

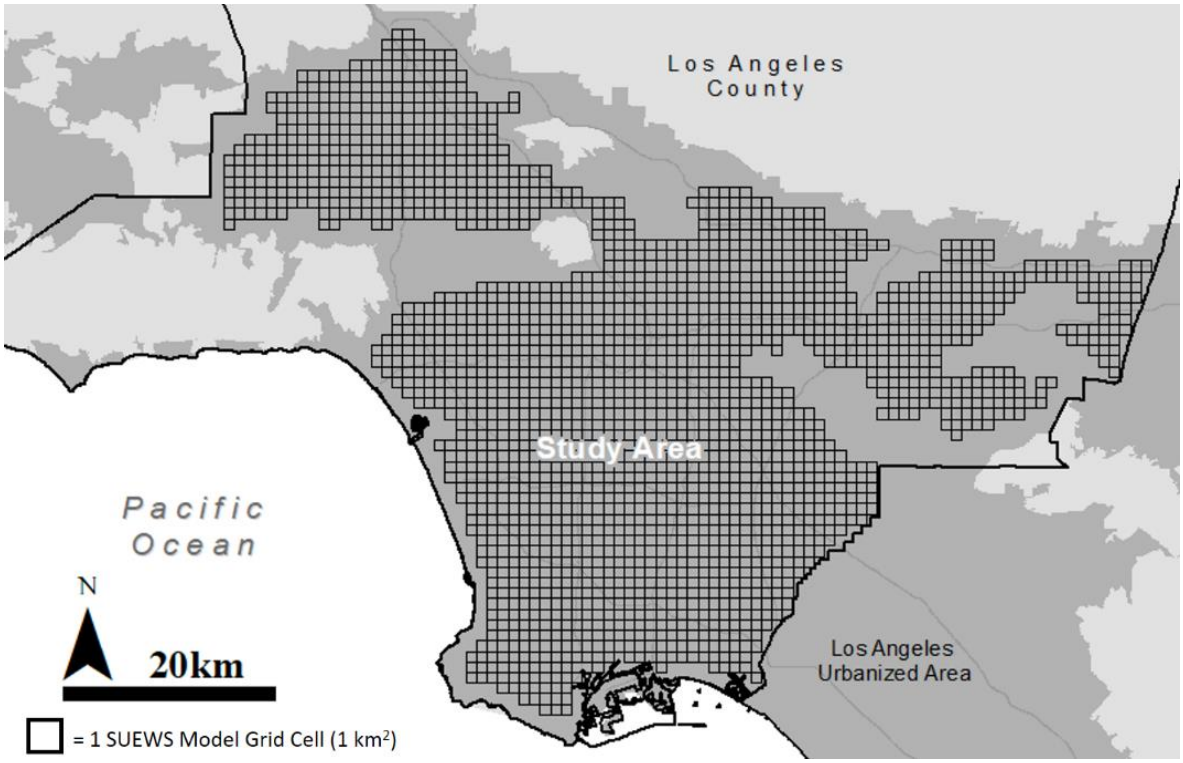

Figure 3.1. Los Angeles study area with model grid cells (n = 2,123). Dark grey indicates urbanized areas, and the thick black line shows the Los Angeles County boundary.

We used two climate modeling frameworks to parameterize SUEWS and approximate study area conditions for August 26, 2014 (the date of remote sensing image collection). North American mesoscale forecast data (NAM) for 13 months preceding the study date (July 2013 – August 214) were acquired for the complete study area from the National Oceanic and Atmospheric Administration National Centers for Environmental Prediction. Shortwave radiation, air temperature, wind speed, relative humidity, and pressure were extracted at a temporal resolution of 6 hours and a spatial resolution of 12 km. Daily precipitation data for the period was derived from 13 weather stations located throughout and surrounding the study area, including stations maintained by the California Irrigation Management Information System (CIMIS), and USCRN. Precipitation values were interpolated across the study area using inverse distance weighting of the nearest 4 stations. Due to the drought conditions, precipitation was a relatively minor source of water, with all stations averaging a total of 10.7 cm in the year prior to the study. The most significant rainfall event preceding the study was 0.6 cm received on April 1, 2014, with only trace rainfall occurring afterward.

We used SUEWS version 2017b to calculate fluxes for our study area (Ward et al., 2017). Outputs from the NAM model runs included stabilized soil moisture resulting from a year of modeled irrigation. These outputs were used as initialization parameters for a second-round model run using WRF model data for August 25 and 26 (Skamarock & Klemp, 2008). WRF data was of finer spatial resolution (3 km) and temporal resolution (hourly) compared to NAM, allowing for greater characterization of meteorological variability across the scene for the date of interest.

We compared WRF air temperature, relative humidity, and pressure values to hourly measurements collected by 8 stations sited across the study area for August 25-27. All three

variables matched the diurnal patterns of the measured data, while also capturing a multi-day increase in air temperature and pressure, and associated decrease in relative humidity. We observed high correlation between modeled and measured air temperature ($R^2 = 0.96$), pressure ($R^2 = 0.97$), and relative humidity ($R^2 = 0.93$). WRF air temperature was slightly warmer than measured, with a mean bias of 0.33°C across all stations and root mean square error (RMSE) of 1.35°C. Modeled relative humidity tended to be lower than measured, with a mean bias of –9.36% and an RMSE of 12.05%. Pressure was also slightly lower than measured, with a mean bias of –1.76 hPa and RMSE of 2.05 hPa. Based on this assessment, we determined WRF climate data to be adequate for driving the SUEWS model calculations for the study date.

SUEWS outputs of LE and H were calculated based on WRF climatology and assessed across all grid cells. We used our LST imagery to calculate a (mean) surface temperature for each grid cell, which we then compared to modeled fluxes. Flux variability was examined across the diurnal cycle, as well as spatially to investigate the effects of local surface characteristics. We also calculated the coastal proximity of each grid cell to assess flux variability along the coastal climate gradient.

3. Results

3.1 Characteristics of Los Angeles metropolitan region landcover

We assessed landcover across the complete Los Angeles metropolitan area using hyperspectral imagery and LiDAR. Landcover estimates derived from hyperspectral imagery (Wetherley et al., 2018) showed that 68.9% of the area was impervious surface, both paved ground (45.6%) and buildings (23.3%), while 22.2% was vegetated by trees (19.3%) and

turfgrass (2.9%). The remaining landcover was 2.8% bare soil and 6.0% dead vegetation, which we combined into a single soil class to match required SUEWS model inputs. Proportions of landcover observed at the grid cell scale were similar, such that fractional coverage in the 2,123 grid cells tended to be dominated by paved ground (45.8 ± 10.1%, mean ± 1 SD) and buildings (23.7 ± 6.7%) (Fig. 3.2). Tree (18.9 ± 9.8%), soil (4.3 ± 4.1%), and turfgrass (2.9 ± 3.1%) constituted significantly smaller fractions of cover across grid cells, however maximum cover for these classes reached 57%, 62%, and 43%, respectively, ensuring that grid cells with a range of landcover combinations were included in the study.

Mean study area albedo derived from hyperspectral imagery was 0.18 ± 0.05. Grid cell-level measurements of albedo ranged from 0.13 – 0.27 with the mean (0.18) and standard deviation (0.04), similar to the entire study area. While whole grid cell albedo was used as the model input for calculating net radiation, we conducted additional analysis of the albedos of the different landcover classes (Fig. 3.2). In general, mean albedos for roofs (0.20), soil (0.20), turfgrass (0.19), paved ground (0.18), and trees (0.17) did not vary greatly. The roof class contained the brightest pixels, ranging as high as 0.42 resulting from highly reflective commercial roofs. Overall ranges for soil (0.03 – 0.30), turfgrass (0.14 – 0.27), and ground pavement (0.10 – 0.32) were all relatively similar to one another. The darkest pixels belonged to the tree class, which ranged from a minimum of 0.12 to a maximum of 0.22.

The vertical structure of grid cells varied widely. Roughness length ranged from 0.045 m – 0.50 m, with a mean (± SD) of 0.61 ± 0.45 m, and zero-plane displacement ranged from 4.73 m – 102.56 m, with a mean of 10.07 ± 3.95 m. This reflected the large variability of object heights across the study area. For example, grid cell tree height ranged from 5.98 – 17.60 m, with a mean of 11.25 ± 1.47 m. Grid cell building height ranged even more widely,

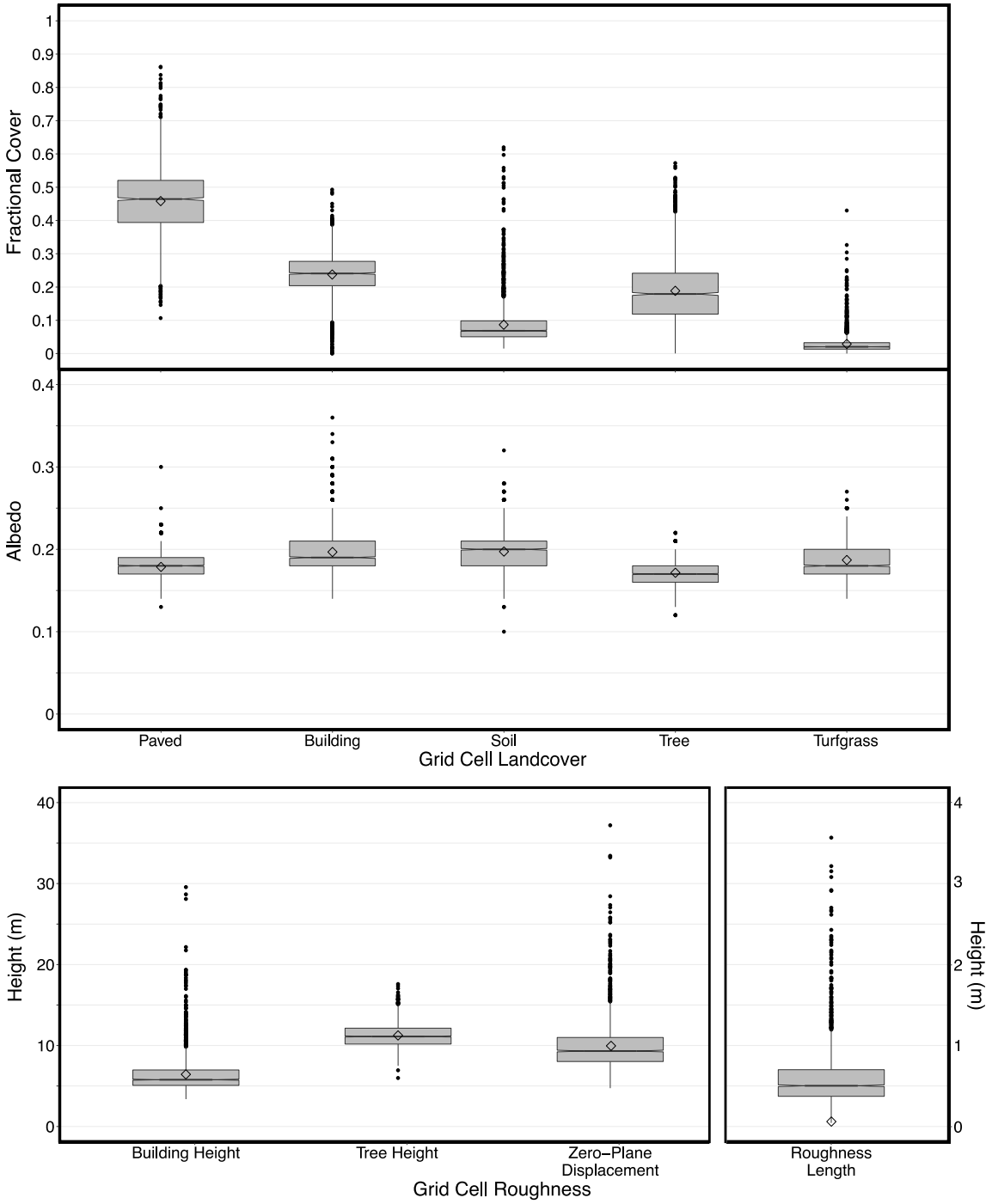

Figure 3.2. Distribution of surface cover (top), albedo (middle), and vertical structure (bottom) parameter values across all study grid cells.

from 3.38 – 60 m. However, the mean building height across all grid cells (6.47 ± 2.60 m) was less than the mean tree height, due to the predominance of one- and two-story buildings. Across all grid cells, 96% had a taller tree height compared to building height, with a mean tree to building height ratio of 1.88 ± 0.47.

3.2 Estimated irrigation water inputs

Estimates of outdoor water use based on residential water consumption data (Mini et al., 2014; Chen et al., 2015) were used to calculate irrigation for each grid cell based on the amount of vegetated area and Eq. 3.2. When scaled by total vegetated area, this produced an estimated irrigation rate of 2.0 to 2.25 cm week^{-1} for grid cells that were > 20% vegetated (Fig. 3.3a). Grid cells that were 10% vegetated received around 1.75 cm week^{-1}, while those with little vegetation (< 3%) received no irrigation.

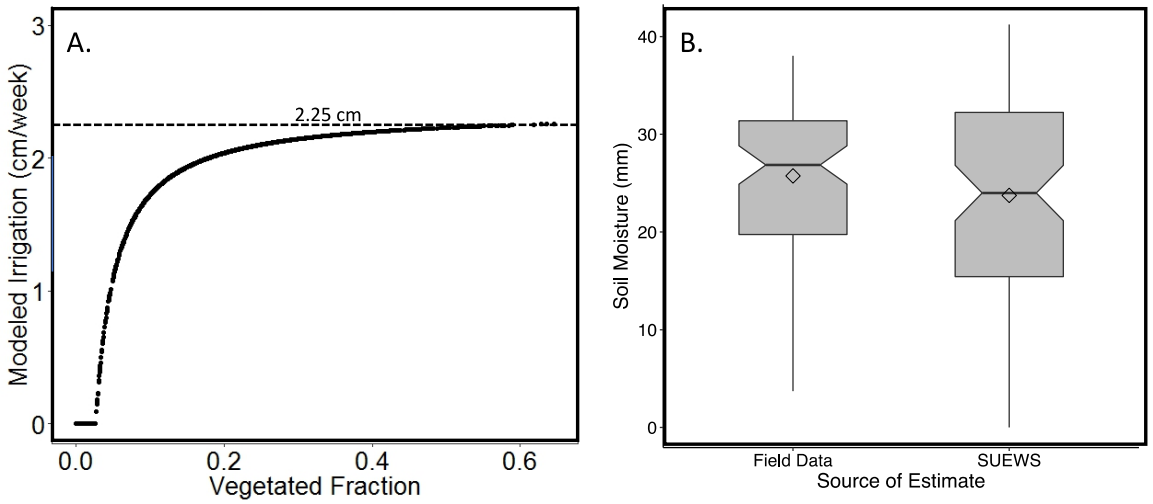

Figure 3.3. Modeled irrigation. A) Estimated weekly irrigation applied to vegetated areas for each grid cell. B) Grid cell soil moisture estimated using two methods—Left: estimated from remote sensing LST and field observations; Right: SUEWS estimate. Mean values are indicated by the diamond and median by the notched horizontal line.

This irrigation estimate was used by SUEWS to calculate the local water balance, including grid cell soil moisture deficit (SMD). SUEWS calculated an average noon-time soil moisture deficit (SMD) of 49.3 ± 10.3 mm across the study area, assuming a soil porosity of 0.57 and soil depth of 150 mm. We converted the SMD estimate to a measure of soil moisture for each grid cell, which we then assessed by using our field data and remote sensing LST to derive a secondary estimate of local soil moisture. We used identical assumptions about local soil conditions to convert field measurements of volumetric soil moisture to an estimate of soil water (mm), extrapolating our near-surface soil moisture measurements to the full 150 mm soil depth by assuming uniform soil moisture throughout. We then used the field-based estimates of turfgrass soil moisture to develop a linear, negative relationship between LST and soil moisture (mm) ($R^2 = 0.52$):

$$\text{Soil Moisture} = -2.35 \times \text{LST} + 120.98 \quad [3.3]$$

We applied Eq. 3.3 to a subset of grid cells from two flightlines that were imaged in the same time window as our field collection. We identified pure turfgrass pixels and averaged their LST for each grid cell, using only grid cells with more than one pure turfgrass pixel (n = 88). We then used the turfgrass LST value for each grid cell to estimate turfgrass soil moisture. Similar analysis for tree cover was not possible, due to additional thermal variability resulting from unknown surface types beneath tree canopies and variable tree rooting depths which could provide additional, unknown water sources (Bijoor et al., 2012).

For the 88 grid cells analyzed, SUEWS produced a soil moisture range from 0 to 44 mm with an average of 24.6 mm, while soil moisture estimates based on field data and thermal imagery ranged from 3.7 to 38.0 mm with an average of 25.7 mm (Fig. 3.3b). A cell-by-cell comparison of the two estimates was highly scattered, indicating the presence of

significant variability in the scene that we could not capture using our methodology. However, differences between the two estimates of soil moisture were not statistically significant ($p > 0.10$), indicating that our estimates of irrigation, and thus available moisture in Los Angeles, were within a reasonable range based on observed LST and field data for turfgrass sites.

3.3 Assessment of modeled fluxes

Because the current version of SUEWS does not estimate surface temperatures resulting from its energy balance computation, we could not directly compare modeled surface temperature estimates to remote sensing LST. Instead, we compared grid cell LE and H fluxes against measured LST (averaged per grid cell) (Fig. 3.4). As it required several hours for the airborne sensors to image the entire Los Angeles study area, we used the grid cell flux values that most closely corresponded to the time at which each grid cell was imaged. Across all flightlines, modeled H was positively correlated with measured LST ($y = 3.9x + 76.1$, $R^2 = 0.21$, $p < 0.001$), while modeled LE was negatively correlated with measured LST ($y = –5.0x + 274.3$, $R^2 = 0.39$, $p < 0.001$). These relationships were expected—surfaces experiencing high LE tend to be cooler as energy is consumed by evaporation, while surfaces with a high H must have high LST as the H of a surface is evidenced by its temperature. The lower R^2 observed for H ($R^2 = 0.21$) relative to LE ($R^2 = 0.39$) is likely because H is modeled as a residual of the energy balance equation, which concentrates energy balance errors in the H term.

At the scale of individual flightlines, the relationship between modeled LE and measured LST improved, while the relationship between modeled H and measured LST

almost completely disappeared. The mean, single-flightline correlation between measured LST and modeled LE reached a maximum of $R^2 = 0.74$ for the final flightline of the day (shown in red in Fig. 3.4), and the average R^2 from all flightlines was $R^2 = 0.48$. Estimates of LE varied greatly within each flightline, producing a pronounced negative relationship with measured LST. This was especially true for the earliest flightline of the day (shown in purple in Fig. 3.4), which included the highest LE estimates. Later afternoon flightlines corresponded more consistently with comparatively lower LE estimates, but still showed a similar linear relationship with LST.

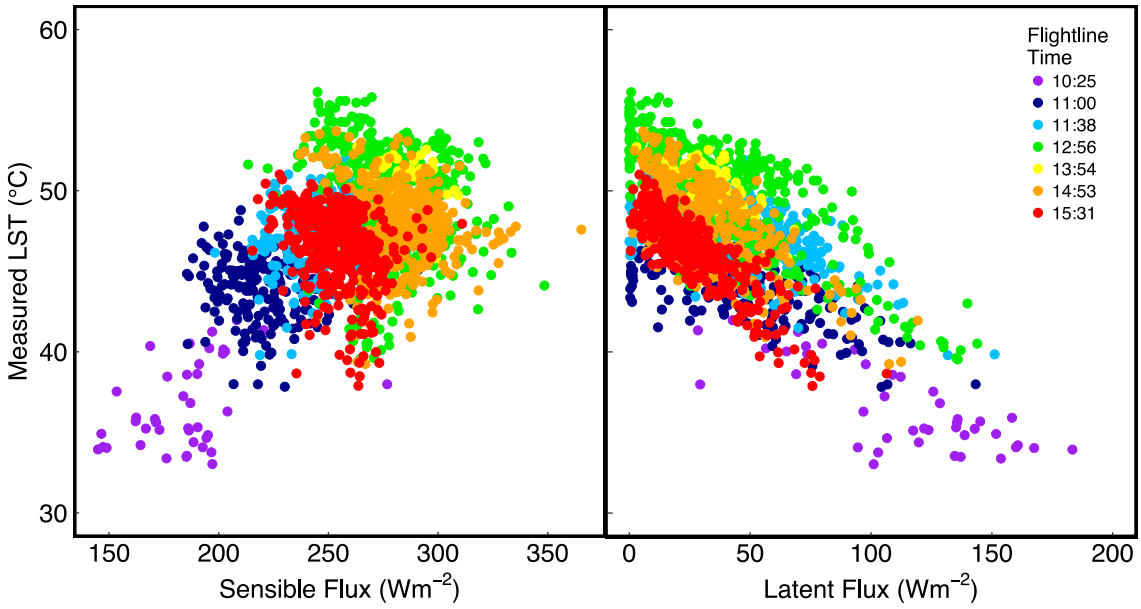

Figure 3.4. Relationship between SUEWS modeled H (left) and LE (right) with mean grid cell LST as measured by remote sensing. Colors indicate the time of day each flightline was collected.

While LE exhibited a strongly linear relationship with LST at the flightline scale, estimates of H at the flightline scale were tightly clustered with very weak to no linear relationship with measured LST (mean $R^2 = 0.05$ across all flightlines). The linear relationship between H and LST displayed in Fig. 3.4 was instead produced by diurnal

temperature changes—as the day progressed, warmer flightlines corresponded to higher estimates of H. It was only by using thermal imagery captured at different times of day that a significant the relationship between H and measured LST could be observed.

Diurnal behavior of H and LE also differed (Fig. 3.5). For most of the daylight hours, the overall magnitude of H was larger than LE. The exception to this occurred between roughly 6:00-8:00 in the morning, when LE and H both increased with similar magnitudes following sunrise. By mid-morning, the magnitudes of the two fluxes differed markedly, with LE peaking at 10:00 with a mean flux of 62.4 ± 36.3 Wm^{-2}. H continued to increase until peaking at 14:05, one hour after peak net radiation, with a mean H of 296 ± 18.7 Wm^{-2}.

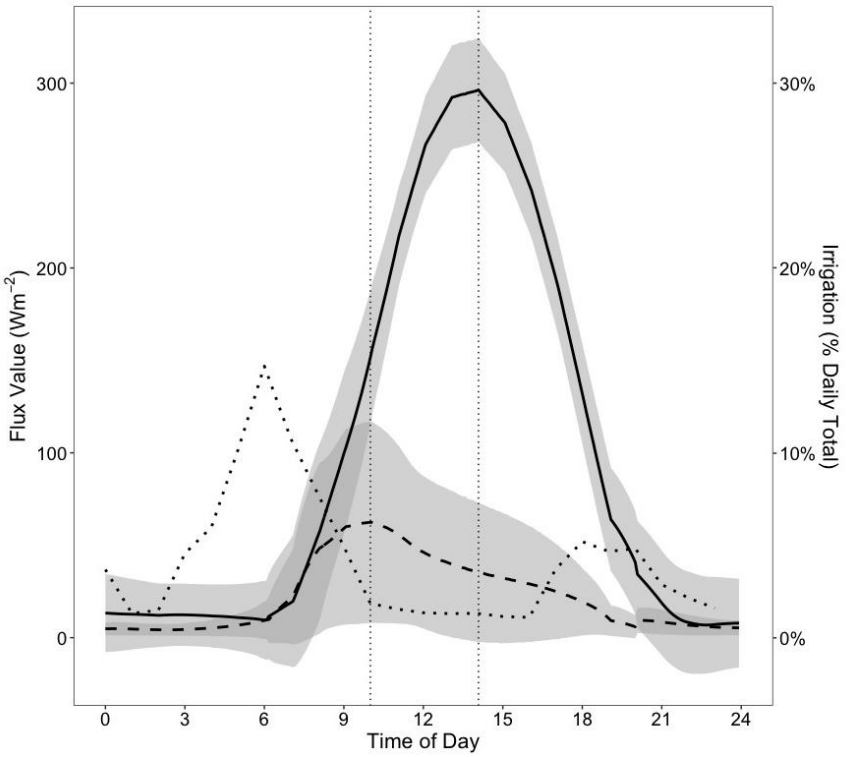

Figure 3.5. Mean diurnal values for H (solid line) and LE (dashed line) across all grid cells (shaded area shows 1.5 times the standard deviation). Dotted line shows daily profile of irrigation (second y axis). Vertical dotted lines correspond to the maximums of LE at 10:00 and H at 14:05, which are mapped in Fig. 3.6.

While H was the larger flux, LE exhibited greater spatial variability. Over the course of the day, the standard deviation of LE across all grid cells ranged from 2.1 Wm^{-2} to 36.3 Wm^{-2}. H displayed a narrower range of variability, with standard deviations ranging from 11.2 Wm^{-2} to 31.9 Wm^{-2} over the course of the day. For both fluxes, the minimum variation was observed at night. For LE, maximum variation occurred at the time of maximum LE at 10:00, while maximum H variation occurred just after 8:00, corresponding to the time when H was steeply increasing over LE.

3.4 Spatial distribution of fluxes

We mapped fluxes of LE and H at the times of their diurnal maxima to examine the spatial variability of the fluxes across the study area. The spatial pattern of LE was closely related to that of vegetation percent cover (Figs. 3.6a and 3.6b). The highest LE generally occurred along the edges of the study area, corresponding to well-vegetated neighborhoods such as Beverly Hills and Rancho Palos Verdes. Conversely, highly developed areas such as the central business district and commercial areas, had relatively low LE. At the diurnal maximum, the 5% trimmed range (i.e., 5^{th} to 95^{th} percentile) of LE across the study area was 119.2 Wm^{-2} and the standard deviation of LE was 36.3 Wm^{-2}.

In contrast, fluxes of H at their diurnal maximum were less variable across the study area, with a 5% trimmed range of 62 Wm^{-2} and a standard deviation of 18.7 Wm^{-2} (Fig. 3.6c). The spatial pattern of H was more strongly related to local albedo, rather than lack of vegetation (or conversely, high impervious fraction) (Fig. 3.6d). This effect was strong enough to ensure that areas of high H did not exactly correlate with areas of low LE. In fact,

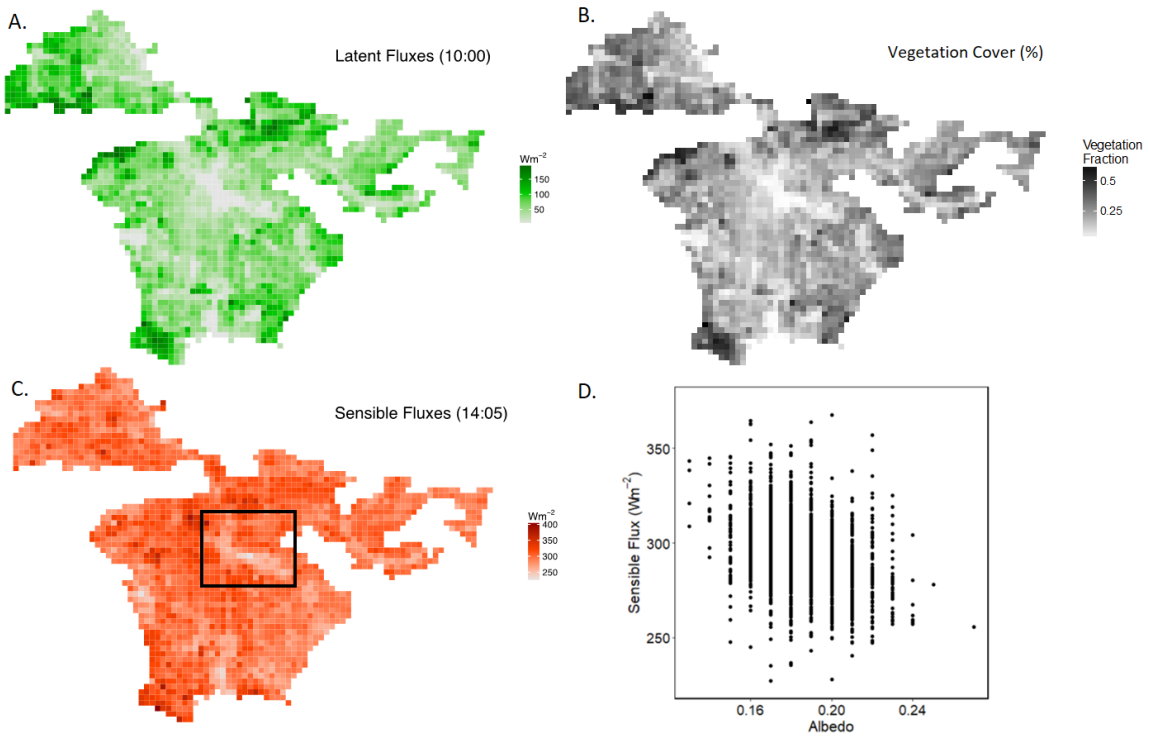

Figure 3.6. Maps of urban fluxes and associated drivers. A) Peak LE and B) vegetation cover shown at the top. C) Peak H and D) scatterplot of albedo and H shown at the bottom. Albedo values were rounded to the nearest 0.01, producing vertical structure in the scatterplot.

many areas with high impervious cover had lower H relative to less impervious areas because of the high albedo of the impervious surfaces, which reduced the available energy to be partitioned into H and LE. For example, the region in the center of the map has both low H and low LE and corresponds to a highly impervious commercial center (box in Fig. 3.6c). Low LE values in this region were due to small amounts of vegetation cover, while low H values occurred because the commercial buildings had high albedo roofs that reduced net radiation relative to grid cells in other areas.

To examine the interactions between H and LE across Los Angeles, we mapped grid cell daily Bowen ratios (β), calculated as the ratio of total daily H to total daily LE (Fig. 3.7). The minimum value across the study area was 1.57, meaning that integrated over the entire

day, no grid cell experienced greater LE relative to H. Overall, 84% of grid cell β fell between 1-10, while the remainder had a value greater than 10 with a maximum of 156.8. These higher values occurred in grid cells with very low vegetation cover, such as the highly developed downtown core, the Los Angeles International Airport, and various industrial centers and refineries. Overall, in our study area we found β could be predicted by f_v using the following equation:

$$\beta = 0.92 \times f_v^{-1.09} \quad [3.4]$$

Based on this relationship, a grid cell with a vegetated fraction of 0.93 or greater would be necessary to produce a β value <1 ($R^2 = 0.77$, $p < 0.001$).

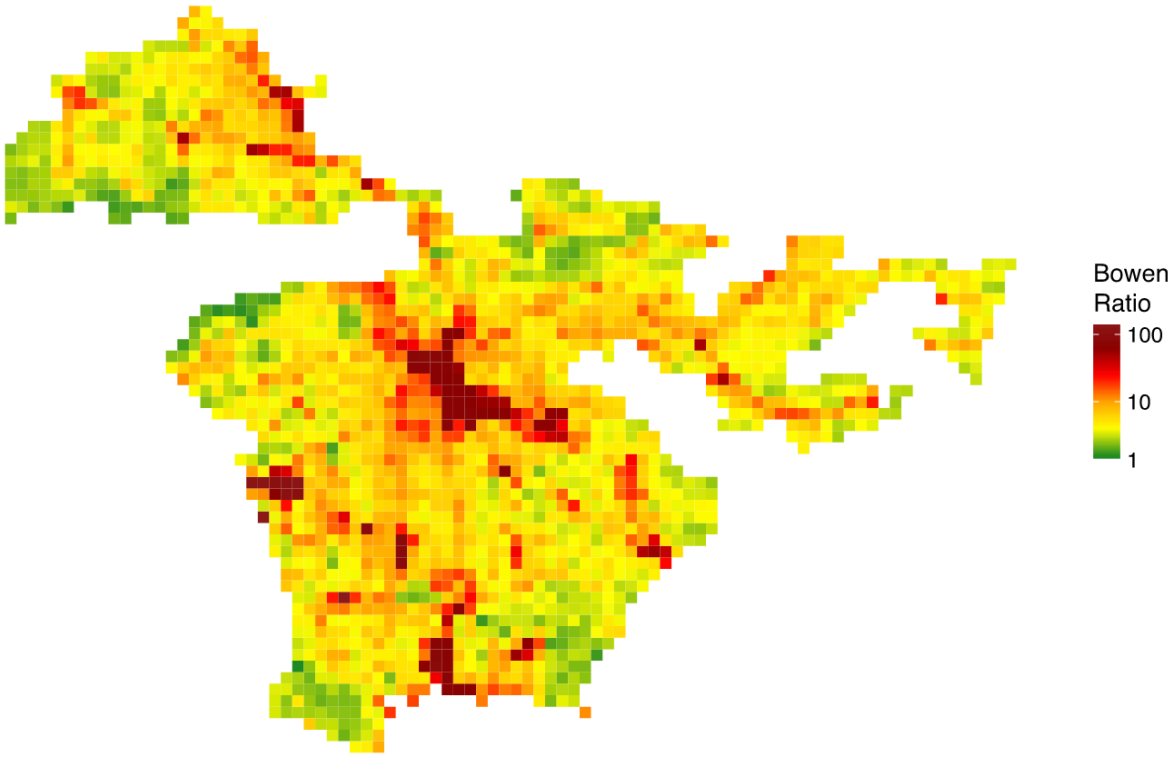

Figure 3.7. Map of daily β across Los Angeles. Colors shown in log scale.

We compared our modeled grid cell β to measured diurnal β from 40 flux tower studies in 27 international cities (Fig. 3.8) (Oke et al., 2017). Our model grid cell pattern of β relative to local vegetation cover was similar to the pattern observed across global urban flux studies, with most of the flux tower studies producing slightly smaller values than modeled here. Three of the flux tower studies were conducted within the Los Angeles study area, occurring in July of 1993 and 1994 (Grimmond & Oke, 1995; Grimmond et al., 1996; Grimmond & Oke, 2002). The β value for these local studies were similar to the range of values that we modeled over the Los Angeles metropolitan region.

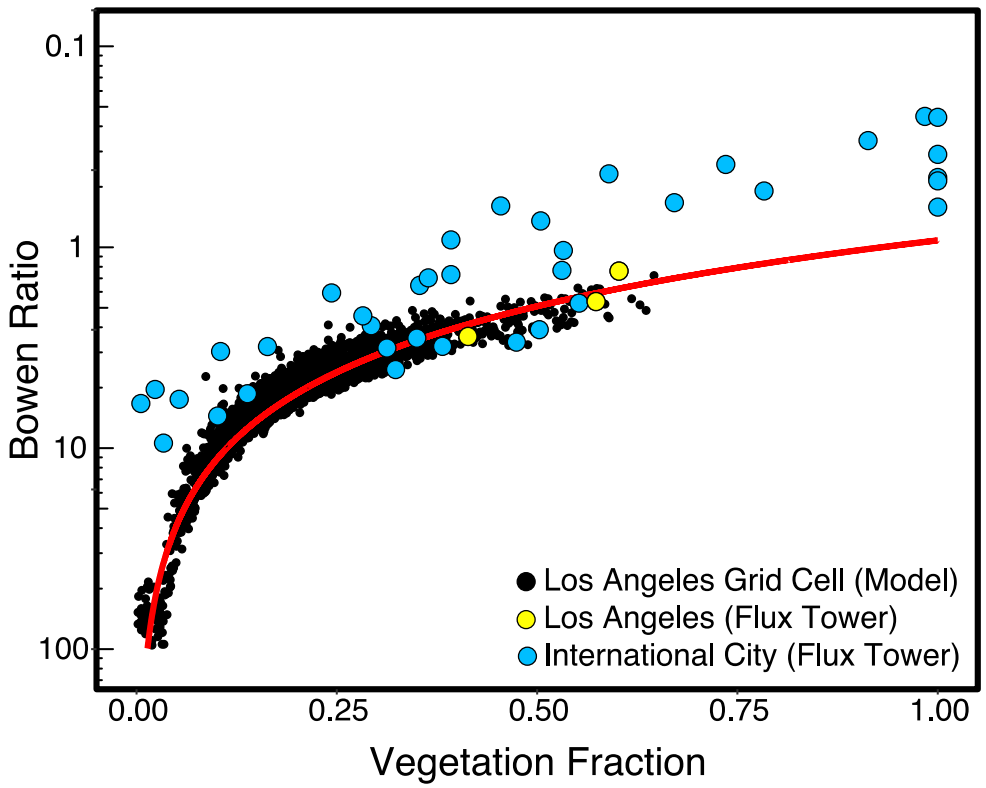

Figure 3.8. Modeled grid cell β with fitted (red) line from Eq. 3.4, compared to β calculated by three flux tower studies that occurred in the Los Angeles study area in July 1993 and July 1994 (yellow). Other international cities shown in blue. All flux tower β values were obtained from Oke et al. (2017). Note the reverse log scale.

3.5 Assessment of climate-driven flux variability

While the spatial pattern of LE across the study area was most closely related to differences in f_v, there were important spatial and temporal variations in this relationship (Fig. 3.9, top row). Early in the day, the relationship between LE and f_v showed little scatter, with the rise in LE corresponding to sunrise at 6:20 and the peak time of irrigation at 6:00. By 9:00, highly vegetated areas continued to experience more LE compared to less vegetated areas. However, decreasing in LE in the early to mid-afternoon produced greater variability than observed in the early morning, following a spatial pattern that was consistent with the distance of the grid cell from the coast. Grid cells closer to the coast, subject to higher levels of humidity and lower air temperatures, had a slower decline in LE, compared to grid cells farther from the coast which experienced higher temperatures and lower humidity. This effect was especially apparent in late afternoon (15:00).

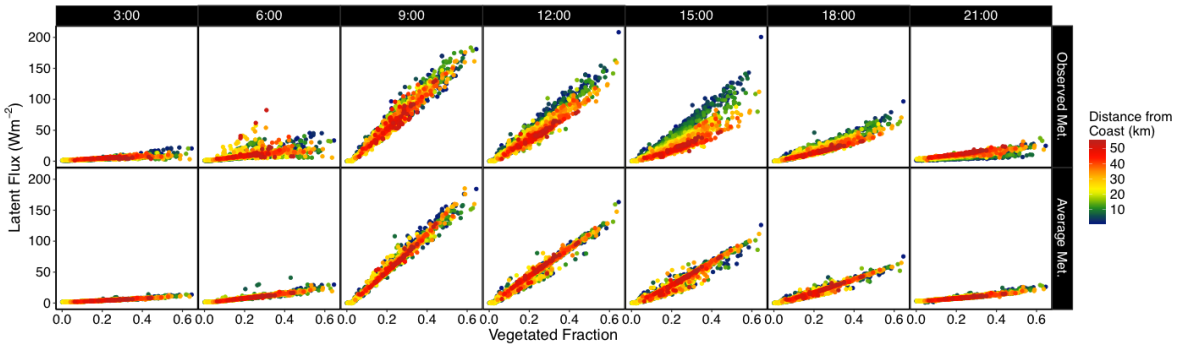

Figure 3.9. Diurnal patterns of LE across the study area in relation to f_v. Each point represents one grid cell, colored by the distance of the grid cell from the coast. The top row shows flux estimates that includes WRF meteorological variables, while the bottom row shows LE estimates using uniform values (hourly average across the study area) for air temperature, relative humidity, and wind.

We further investigated the effect of coastal distance by conducting a second SUEWS simulation with the meteorological effect of the coast removed. We used identical surface parameter values, but replaced spatially varying air temperature, relative humidity, and wind with the study area hourly mean for these variables (as modeled by WRF) to serve as the meteorological forcing for all grid cells (Fig. 3.9, bottom row). This "average" meteorological forcing produced estimates of LE that were much more tightly coupled to f_v. Overall, LE values showed less scatter with no obvious coastal effect observed in the afternoon.

We conducted a multivariate linear regression analysis at a 5-minute time step to quantify the observed spatial and temporal effects of f_v and coastal distance on LE. We first standardized the values of f_v and distance by calculating their z-scores, then conducted multivariate linear regression to produce coefficients for each variable, which we plotted diurnally. Model R^2 values remained below 0.75 before 7:45, however from 8:30 until sunset, R^2 values ranged from 0.88 to 0.97, with an average value of 0.92. The results show the change in LE resulting from a 1 SD increase in f_v (11.2%) or coastal distance (12.4 km) (Fig. 3.10). As expected, we observed a significant, positive effect of f_v throughout the day, peaking at 10:00 when LE was at its maximum ($p < 0.001$). At this time, a 1 SD increase in vegetation cover produced an increase in LE of 35.8 Wm^{-2}. The effect of distance was weaker but significant for all daylight hours ($p < 0.001$). With sunrise there was a slight positive effect of distance, peaking at 7:50 when a 1 SD increase in distance from the coast increased LE by 4.7 Wm^{-2}. This rapidly declined through the late morning, becoming negative an hour later at 8:50. The strongest coastal effect was observed at 14:55 when 1 SD of coastal distance reduced LE by -8.5 Wm^{-2}. At this time, the effect of f_v was 21.3 Wm^{-2}, which means

a theoretical grid cell with 50% vegetation cover and adjacent to the coast would produce 95.0 Wm^{-2} of LE, while an identically vegetated grid cell located farthest from the coast (maximum of 55.9 km (or 4.5 SD) among all grid cells) would produce 56.8 Wm^{-2} of LE, or an overall positive effect of coastal proximity equal to 38.2 Wm^{-2}.

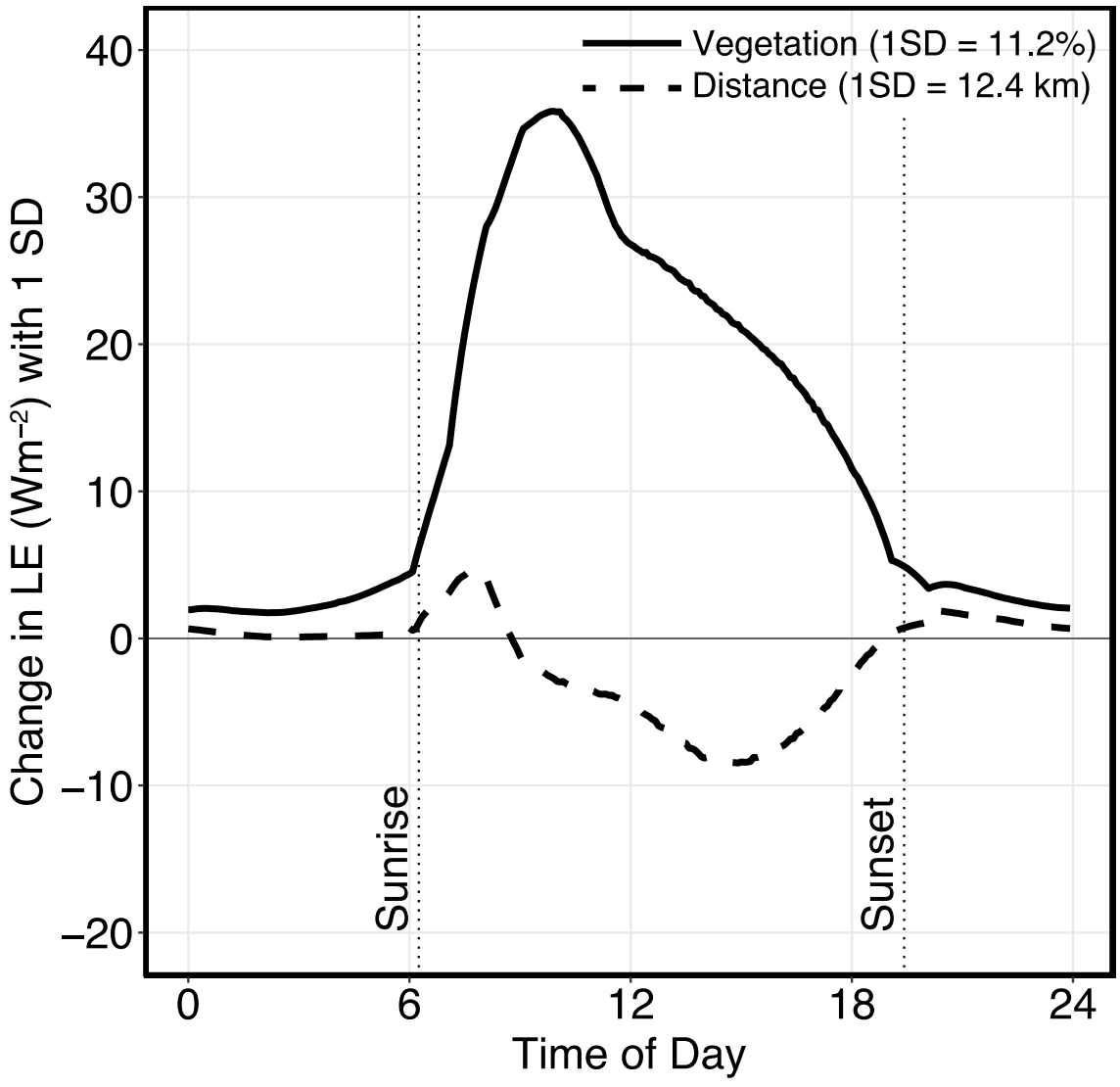

Figure 3.10. Change in LE for every 1 SD change in vegetation cover (solid line) and distance from the coast (dashed line). Vertical dotted lines show sunrise and sunset times.

4. Discussion

4.1 Energy and water exchange across the Los Angeles metropolitan region

We combined hyperspectral imagery with LiDAR to quantify the surface of Los Angeles in terms of its material, plant type, and structural heterogeneity for 2,123 continuous grid cells (2,123 km^2). By carefully parameterizing urban surface variability over an extensive heterogeneous domain, we obtained a large sample of urban neighborhood types that allowed us to conduct a detailed investigation of surface-driven flux variability. Our large spatial domain also allowed us to untangle relative effects of irrigation and regional climate. In contrast, neighborhood-scale applications of SUEWS cannot observe these types of large-scale variability (Karsisto et al., 2016; Nordbo et al., 2015; Onomura et al., 2015; Ao et al., 2016; Demuzere et al., 2017; Golding et al., 2017), while larger applications have typically relied on land use classification maps, or simple assumption about land cover distribution (Alexander et al., 2015; Alexander et al., 2016; Rafael et al., 2016; Ward & Grimmond, 2017; Järvi et al., in Prep). These approaches may not realistically account for complex controls on heterogeneity in land cover in diverse urban areas such as Los Angeles.

Parameters extracted from remote sensing data agreed closely with those reported in the literature for typical urban areas. Our estimates of paved ground (45.6%), roofs (23.3%), and vegetation (22.1%) closely matched existing estimates of paved ground (~40%), roof (20–25%), and vegetation (20–30%) for other North American cities (Rose et al., 2003; Akbari et al., 2009). Our estimated albedo of 0.18 ± 0.05 was slightly higher than the range of 0.14-0.15 reported by Oke (1988), but similar to values reported for Santa Barbara by Roberts et al. (2012), and may have been influenced by the presence of many high albedo commercial roofs in Los Angeles. Our estimate of roughness length was 0.61 ± 0.45 m across all grid

cells, which agreed with the range of 0.2–1.3 m reported for several different cities and urban land use types (Grimmond & Oke, 1999). Our average zero-plane displacement length of 10.07 ± 3.95 m was larger than the typical range of 2–5 m reported by the above, but closely matched those of densely urban cities such as Mexico City (10 m) and Vancouver (19 m).

In the Los Angeles metropolitan region, irrigation represents an important influence on energy partitioning and a major use of water—in the City of Los Angeles alone irrigation accounts for 54% of all water use by single family households, and similar application can be assumed over the larger urbanized region (Mini et al., 2014; Vahmani & Hogue, 2015). We calculated likely irrigation based on a dataset of Los Angeles City water use from a similarly dry period (August 2007) and remote sensing estimates of green vegetation cover. Because irrigation is required to maintain the largely non-native Los Angeles flora in summertime, the presence of green vegetation is a strong indicator of irrigation in our study area (Pataki et al., 2010; Clarke et al., 2013). Furthermore, nearly 70% of southern California homeowners use automatic sprinklers, 87% of which are controlled by automatic timers rather than weather-dependent irrigation controllers, which means irrigation will occur consistently, regardless of weather, season, or soil condition (DeOreo et al., 2011; Chen et al., 2015). Our estimate of ~2.25 cm/week is similar to the recommended irrigation amount of 2.5 cm/week for turfgrass, suggesting that this amount would be adequate to maintain the observed green vegetation (Milesi et al., 2005). Our additional assessment of soil moisture using field data and remotely sensed LST further supports the validity of our irrigation estimate.

Finally, while our collectively fine spatial parameterization of landcover and water use across the metropolitan region enhanced our estimates of local energy fluxes, assessing these fluxes across the strong regional climatic gradients necessitated similarly spatially (and

temporally) detailed meteorological inputs. These we derived from the WRF regional climate model, and assessed using several local weather stations. We found modeled relative humidity to be drier than measured, with a mean bias of –9.36% and an RMSE of 12.05%. As we did not use a coupled WRF-urban climate model, it is possible that the drier conditions produced by the model did not account for elevated humidity from local irrigation. Future work should investigate this further. Despite this discrepancy, overall air temperature, pressure, and relative humidity were strongly correlated with station data ($R^2 \geq 0.93$ for each variable), and incorporating spatially distributed meteorological variables allowed us to quantitatively decouple small-scale (f_v) from regional-scale (coastal proximity) flux effects across the diurnal cycle.

4.2 Study design

There are a few ways our results may have been influenced by our study design. First, our selection of 1 km^2 grid cells likely affected our observations of flux spatial variability. For example, no grid cell had a daily $\beta < 1$, which we calculated would require ≥ 93% vegetation cover. Los Angeles does have some large, well-watered vegetated spaces, and had we selected a smaller grid cell size we would have likely observed lower Bowen values in grid cells with nearly continuous vegetation cover. Considering that SUEWS has been applied to study areas ranging from a few hundred m^2 to 150 km^2, the appropriate grid cell size likely depends on both the features of the study area as well as the goal of the investigation (Ward et al., 2016; Ward & Grimmond, 2017). We assessed our selection of grid cell size by comparing metropolitan-scale cover fractions for each landcover class to the distribution for each class observed among all grid cells. City-level fractions scaled closely to

grid cell distributions for paved ground (45.6% at the metropolitan-scale and 45.8 ± 10.1% across all grid cells), buildings (23.3% and 23.7 ± 6.7%), trees (19.3% and 18.9 ± 9.8%), soil (2.8% and 4.3 ± 4.1%), and turfgrass (2.9% and 2.9 ± 3.1%), suggesting that our grid cell size captured material mixtures representative of the broader metropolitan area.

We also did not account for landcover change during our 13-month model spin-up period. Our map of landcover, including vegetation extent, was based on imagery collected in August. However, vegetation extent at that time was likely less than a year previous, due to the ongoing drought, water conservation campaigns, turfgrass removal programs, and a growing threat from pests (Fears, Feb. 27, 2016; McPherson et al., 2017). Additionally, because we only evaluated fluxes for a single day under relatively unique (drought) conditions, our observations of the interactive effects of coastal proximity should be more extensively evaluated for varying climatic conditions and seasonal variability.

Finally, SUEWS calculates anthropogenic heat flux (F) based on estimated population density, which we calculated per grid cell using U.S. Census Bureau estimates. However, Census population estimates are likely a better indicator of nighttime (residential) population rather than daytime population. In a commuter city such as Los Angeles, where significant population changes occur as people commute between residential and commercial zones, the spatial distribution of F likely changes based on the time of day and day of the week. By using population estimates based on residential population, daytime F was likely overestimated in residential areas and underestimated in commercial areas.

4.3 Applications of novel remote sensing for urban biophysical modeling

In this study, remote sensing allowed for estimation of local parameters across a large

area, ensuring relatively accurate model inputs relative to those acquired from more static sources, such as a classification map. For example, spectral mixture analysis and hyperspectral imagery allowed us to more accurately characterize vegetation at the time of our study, when drought conditions likely reduced the amount of green vegetation and increased soil and senesced vegetation cover (Sahagun, April 19, 2017). With senescence, photosynthetically active and inactive plant material can form small-scale mixtures that, if quantified using a full-pixel classification, could result in an overestimation of vegetation cover (Guerschman et al., 2009). Conversely, a mismatch between a large pixel size and small vegetation patches can result in underestimating vegetation cover and reduce modeled LE (Nordbo et al., 2015). Sub-pixel analysis is not subject to these limitations, and several studies have found the combination of spectral mixture analysis and hyperspectral imagery to produce highly accurate estimates of urban vegetation cover (Roberts et al., 2012; Okujeni et al., 2015; Wetherley et al, 2017). Hyperspectral imagery was also critical for extracting sub-pixel classes matching those required for SUEWS. Due to their spectral similarity, separating turfgrass from tree fractions, as well as bright impervious, soil, and senesced vegetation fractions, at sub-pixel scales typically requires enhanced spectral resolution (Nagler et al., 2000; Wetherley et al., 2017). The resulting fractional product was compatible with SUEWS, which does not require information on the spatial arrangement of surface materials within each grid cell.

Using airborne thermal imagery provided a unique view into the different energetic behaviors of H and LE. Critically, sampling thermal imagery over the course of the day was necessary to observe the positive relationship between H and LST. Taken within any single flightline, there was almost no relationship between H and LST. This is because the

magnitude of H depended on the amount of available energy in the system, with peak H occurring an hour after peak net radiation. While spatial patterns were produce by local albedo, diurnal change had a larger effect on net radiation. Therefore, both net radiation and H exhibited greater diurnal variability rather than spatial variability, which could only be observed using thermal imagery collected at multiple times during the day, as shown in Fig. 3.4. Conversely, a strong negative relationship was maintained between LE and LST within each flightline. LE variability was primarily spatial as it was limited by local meteorological and biophysical factors, which in this study was primarily f_v (Monteith, 1965; Waring & Landsberg, 2011). Together, these findings raise important questions regarding the importance of both spatial and temporal resolution of thermal imagery to assess modeled turbulent fluxes.

4.4 Human and biophysical influences on urban microclimate

Our results showed that water conservation scheduling of automatic irrigation systems may have shifted the diurnal peak of LE to approximately 3 hours earlier than the solar maximum, in contrast to flux observations reported more than two decades ago. We modeled irrigation based on a 2011 survey of California homeowner water use that reported peak irrigation at 6:00, followed by very low outdoor water use for most of the afternoon and a smaller peak around 18:00 (DeOreo et al., 2011). As a result, diurnal LE across grid cells closely matched this profile, with a delayed, primary peak at 10:00 (Fig. 3.5). This contrasts with Los Angeles flux tower observations from 1993 and 1994 that observed peak LE closer to solar noon (Grimmond & Oke, 1995; Grimmond et al., 1996; Grimmond & Oke, 2002). Critically, these studies largely pre-date the onset of water conservation measures throughout

the area. For example, beginning in 2007 the City of Los Angeles instituted several water conservation measures, including time-of-day irrigation restrictions (Mini et al., 2015). We surveyed municipal codes, water provider regulations, and drought-specific emergency measures for the 193 different water-providing jurisdictions within the study area. We found that in August 2014, 55% of jurisdictions representing 71.4% of grid cells (or 1,516 km^2 of the study area) prohibited irrigation between (on average) 9:00 and 17:30, closely matching the survey profile. It is therefore possible that changing irrigation behavior has shifted peak LE to earlier in the day. This raises additional questions of whether water conservation practices could reduce the effectiveness of vegetation for moderating elevated urban temperatures when they are highest later in the day.

Whereas LE was shifted temporally by irrigation, spatially we observed LE to be affected by coastal proximity, with its strongest effect in the late afternoon. LE near the coast was maintained at higher levels (per unit vegetation fractional area) compared to LE farther from the coast. Several studies have observed how sea breezes and higher coastal humidity can moderate urban climates, lowering air temperatures and affecting the nighttime urban heat island (Pinho & Orgaz, 2000; Gedzelman et al., 2003; Pigeon et al., 2006; Hu & Xue, 2016). In our study, a strengthening vapor pressure deficit with coastal distance, combined with limited soil moisture throughout the study area, could induce earlier stomatal closure in interior vegetation, lowering its LE relative to that of coastal vegetation.

In contrast to our findings, a previous study of the Los Angeles coastal gradient found increasingly negative slopes between measured LST and NDVI with greater distance from the coast, concluding that interior vegetation had enhanced cooling power relative to coastal vegetation (Tayyebi & Jenerette, 2016). In addition to the implied assumption of an ample

desert water supply, this previous finding may be further confounded by the time of day when their thermal imagery was captured: the most interior area was imaged first at 10:30, the center at 12:30, and the coast at 14:15, making it possible that the study was comparing a time of peak (morning) LE in the desert to a time of relatively weaker (late afternoon) LE along the coast.

Our large modeling domain allowed us to calculate β as a continuous function of changing vegetation cover, closely agreeing with summertime flux tower data from three tower studies in Los Angeles (Fig. 3.8) (Grimmond & Oke, 1995; Grimmond et al., 1996; Grimmond & Oke, 2002; Oke et al., 2017). This continuous signal cannot be easily observed using flux tower or in situ data, as it requires a large number of sites with varying landcover. The scatter of grid cell β along this curve is determined by intra-city climate variability, which in Los Angeles can largely be attributed to the coastal climate gradient. This is demonstrated by the tightening of the f_v-LE relationship when the coastal effect was removed (Fig. 3.9b).

Additionally, the Los Angeles β function is described by the power law (Eq. 3.4), with very high values at very low f_v , while the pattern across global cities appears to be log-linear. This departure may be driven by the Los Angeles region's dependency on irrigation as a primary source of moisture, producing a tight coupling between LE and local vegetation. This coupling may have been enhanced by our model set-up, which did not include anthropogenic wetting of impervious surfaces, such as street cleaning, which has been observed to reduce β (Best & Grimmond, 2016). In wetter climates, precipitation would decouple urban LE from vegetation—for example, evaporation from impervious surfaces following a rain event accounts for ~20% of total LE, which would reduce the steepness of the β curve at small f_v

(Ramamurthy & Bou-Zeid, 2014).

Our results suggest that arid and irrigation-dependent cities may exhibit a unique pattern of flux partitioning that becomes apparent at small f_v . Modeled β began to steeply increase ~20% vegetation cover, corresponding to our estimate that areas with less than 20% vegetation receive less water than larger vegetated areas (Fig. 3.3a). Evidence that this may be a realistic assumption for arid cities has been observed by remote sensing studies of Los Angeles and Phoenix, which noted a steep, non-linear decrease in remotely sensed LST with increasing turfgrass cover, possibly indicating differences in management of large versus small vegetation patches (Myint et al., 2013; Wetherley et al., 2018).

5. Conclusion

In this study, we set out to answer three questions. First, we asked how urban materials and vertical structure vary across the Los Angeles metropolitan region. We found Los Angeles to have distributions of cover, albedo, and roughness similar to many other urban areas, but with significant variability of cover and roughness among different neighborhoods (grid cells). Second, we asked how surface cover characteristics affect turbulent fluxes simulated by SUEWS. We found LE and H to be dominantly influenced by different surface properties. The spatial distribution of LE was strongly tied to f_v, while non-vegetated areas experienced almost no LE due to a tight coupling between vegetation and moisture availability. Temporally, LE was largely controlled by the timing of irrigation. This may have been shifted by local water conservation policies, raising questions about the capacity of irrigated urban vegetation to mitigate urban heat under water conservation regimes. In contrast, H was mostly influenced by the diurnal pattern of net radiation, with

some spatial relationship shown with local albedo. Finally, we asked how regional climate drives spatial and temporal LE variability across the Los Angeles. We found significant spatial and temporal variability (above that resulting from the distribution of vegetation and irrigation) resulting from coastal distance, with the strongest effect in the late afternoon when LE was reduced by 8.5 Wm^2 for every 1 SD increase in coastal distance. Overall, these findings suggest that the partitioning of energy in a megacity needs to be evaluated across multiple spatial and temporal scales, while demonstrating the powerful role of remote sensing for understanding both static as well as dynamic features of the functioning urban environment.

Several prospects for future work stem from this study. First, our theorized shift in peak LE as a consequence of water conservation could be directly measured by a flux tower or possibly a finer temporal dataset of LST. Second, the detailed parameter values for Los Angeles provide a quantitative window into the surface variability of the region. For example, our discovery that trees across Los Angeles tend to be taller than buildings could have consequences for their function—when trees are above rooflines they are exposed to more wind and could be heated from below, while also casting larger shadows (Kjelgren & Montegue, 1998; Zhao et al., 2015; Feng and Myint, 2016; Wetherley et al., 2018). Third, a more detailed assessment of the coastal effect on LE through different seasons and in non-drought scenarios would provide more information on its microclimate effects. Finally, additional investigation of observed fluxes across other biophysical and socioeconomic variables could illuminate additional sources of variability.

In the Los Angeles metropolitan region, human and biophysical factors individually and collectively affect energy partitioning across spatial and temporal scales. In this study, we

could quantify the microclimate effects of urban vegetation, water conservation policies, and regional climate thanks to observations developed across a large urban footprint. Our strategy of using advanced remote sensing technologies to carefully parameterize a sophisticated urban energy balance model and expand our observational domain could be further extended to capture variability for urban environments across regions, seasons, and climates. Such comparisons will likely illuminate additional drivers of urban climate variability that affect billions of people. The importance of developing such an understanding will continue to grow as urban climates become increasingly affected by global warming, extreme weather, and the urban policies designed to mitigate these emergencies.

Acknowledgements

This research was supported by the NASA Earth and Space Science Fellowship Program (NNX16AO58H); and by the Belgian Science Policy Office in the framework of the STEREO III Program—Project UrbanEARS (SR/00/307). We thank the Jet Propulsion Laboratory for providing hyperspectral and thermal imagery used in this analysis and the County of Los Angeles for providing additional GIS data. We also thank Dr. Leena Järvi for her assistance with SUEWS.

Conclusion

The goal of this work is to contribute to a better understanding of urban vegetation function and its interactive effects with microclimate variability across urban surface heterogeneity. I've shown that urban vegetation can be mapped and its function observed and modeled across large, complex urban systems using remote sensing. In Chapter 1, I found that urban trees and turfgrass, as well as pairs of other spectrally similar classes, can be discriminated accurately at sub-pixel scales when using hyperspectral imagery. Overall fractional accuracy was affected by the spatial resolution of the spectral library and image, as well as the (dis)similarity of the measured classes. Spectral libraries of multiple-resolution endmembers performed better than single-resolution libraries, likely because they increased within-class variance by capturing multiple levels of material variability that occur across spatial scales. Significant pixel mixing occurred at 4 m resolution, with around half of all pixels in the image modeled by more than one endmember. Fractional estimates produced by the best performing libraries at 4 m and 18 m resolution correlated with validation fractions, with mean $R^2 > 0.89$ for spectrally dissimilar classes and mean $R^2 > 0.76$ for spectrally similar classes. These results demonstrate the potential for hyperspectral imagery to detect functionally significant classes, such as plant types, at sub-pixel scales, as well as the scalability of urban cover fractional estimates using hyperspectral imagery.

In Chapter 2, I found significant LST variation between trees and turfgrass. Across heterogeneous mixtures, the negative slopes observed between vegetation fraction and LST were significantly different for these two plant types. I produced a map of vegetation temperature variability by first quantifying LST change across fractional gradients and then removing the first order effect of vegetation fraction on LST. Across the Los Angeles region,

vegetation LST varied by 14°C (+/- 2 SD). The variation displayed visible spatial patterns, with relationships that appeared quantitatively consistent with irrigation ($R^2 = 0.55$), implying that a functional signal of LST was being observed. Significant thermal patterns related to building density were also measured, with an increase in tree LST with building density contrasting with a minimal thermal response of turfgrass to building density. These results show that an LST signal of vegetation function, distinct from that of vegetation fractional cover, can be observed and modeled at city-scales using fractional mixture analysis.

In Chapter 3, modeled latent fluxes were linearly correlated with measured LST at the neighborhood (grid cell) scale ($R^2 = 0.39$), and modeled neighborhood Bowen ratio values closely agreed with previous flux studies conducted in Los Angeles. Albedo was the dominant factor influencing sensible heat flux, while latent heat flux was strongly tied to vegetation fraction. Additionally, latent heat flux across the Los Angeles metropolitan region displayed characteristic spatial and temporal responses to irrigation and regional climate. Early morning irrigation schedules, designed to conserve water, shifted peak latent heat flux to 3 hours before solar noon. This was in contrast to observed peaks at solar noon two decades earlier, suggesting that water conservation policies may reduce the potential of urban vegetation to mitigate elevated urban heat in the afternoon. Additionally, a negative effect of coastal distance on latent heat flux was observed to increase through the morning and late afternoon, resulting in reduced latent heat flux in interior areas relative to coastal areas. These findings suggest that augmenting urban energy flux analyses with large-scale remote sensing and regional climate model inputs can reveal local and regional drivers of urban energy fluxes beyond that which can be determined from in situ measurements at more local scales.

There is great potential for extending the methodology described here to other urban systems around the globe. While the three chapters of this dissertation relied on hyperspectral data to produce enhanced sub-pixel urban landcover maps, imagery collected by the next generation of global imaging systems may have the spectral, spatial, and temporal resolution necessary to produce maps of similar or better quality. For example, Sentinel-2 AB (launched in 2015 and 2017) samples 13 bands in the visible, near-infrared, and short-wave infrared (VSWIR) at 20 m spatial resolution with a revisit time of 5 days (compared to Landsat 8 which samples 7 VSWIR bands at 30 m resolution every 16 days). This spectral resolution may be adequate for mapping fractions of soil, senesced vegetation, and impervious surfaces. It may also be enough to distinguish fractions of urban tree and turfgrass cover—as shown in this work, overall spectral brightness is a primary distinguishing characteristic between these two plant types, which may not require hyperspectral data to resolve. In addition to its global scope, orbital imagery is superior to airborne imagery in other aspects, with a more frequent revisit rate (to capture changing landcover and seasonal or drought-induced vegetation senescence), a larger footprint, and a more consistent sun-sensor geometry.

Where new orbital imagery could enable global mapping of urban composition, the methodology described in Chapter 2 for assessing urban vegetation LST variability requires thermal imagery with a finer spatial resolution than is currently available from Landsat (100 m) or ASTER (90 m). This method relies on mixed thermal pixels that contain only one vegetated and one non-vegetated surface. Larger thermal pixels would be more likely to contain more than two surfaces, which may obscure the thermal signal of vegetation. However, this method could be extended to other cities using airborne thermal imagery, such as that collected by NASA's HyspIRI Airborne Campaign, or even globally using

experimental thermal data, such as imagery acquired by NASA's year-long ECOSTRESS mission.

Large-scale urban flux mapping, as described in Chapter 3, could be accomplished for any urban area that has the necessary data. Certain datasets could be generated for almost any city, including satellite-based (e.g., Sentinel-2) estimates of landcover and albedo, as well as mesoscale models for deriving meteorological inputs (e.g., the Weather Research and Forecasting Model, North American Mesoscale Forecast System, or other climate models that can be downloaded from a variety of publicly available resources). One potentially limiting datasets is LiDAR, which is necessary for characterizing urban vertical structure. While expensive, LiDAR data is increasingly available for global cities and, if not available, could potentially be approximated using local climate zones (Stewart & Oke, 2012). Digital photogrammetry also has considerable potential for deriving height in urban areas. Another necessary dataset is external water application. This study leveraged a large, spatially and temporally distributed dataset of measured water use, however such data are not common and can be subject to privacy protections. Analysis of rain-fed systems that do not depend on irrigation could be more feasible, although quantifying rainfall inputs (and validating wind, pressure, and temperature measurements derived from the mesoscale climate model) will require in situ weather station measurements. While these necessary datasets may be difficult to initially assemble, once integrated at the grid-cell scale estimates and comparisons of urban flux variability can be conducted for cities globally. Establishing a data processing pipeline for incorporating newly available imagery and climate inputs could extend such analyses to examining variability linked to seasonality, inter-annual variability, and global climate change.

This dissertation has shown that while small scale conditions produce urban microclimates, significant drivers of microclimate variability occur across large spatial domains. In the greater Los Angeles metropolitan region, our observational and modeling studies quantified significant thermal responses of vegetation along regional gradients of constructed material, building density, irrigation, income, and climate, all of which required a large urban footprint to observe. The importance of spatial variability further illuminates the potential for advanced remote sensing techniques to complement small-scale in situ or flux tower studies, which are relied upon to parameterize urban energy balance models, as well as optimize their placement. Fusing remote sensing, observational, and modeling techniques will expand our understanding of the functioning urban environment to larger, yet more finely resolved spatial and temporal scales.

Bibliography

Adams, J.B., 1993. Imaging spectroscopy: Interpretation based on spectral mixture analysis. Remote geochemical analysis: Elemental and mineralogical composition 145–166.

Akbari, H., Menon, S., Rosenfeld, A., 2009. Global cooling: increasing world-wide urban albedos to offset CO2. Climatic Change 94, 275–286. https://doi.org/10.1007/s10584-008-9515-9

Akbari, H., Pomerantz, M., Taha, H., 2001. Cool surfaces and shade trees to reduce energy use and improve air quality in urban areas. Solar Energy, Urban Environment 70, 295–310. https://doi.org/10.1016/S0038-092X(00)00089-X

Alexander, P.J., Fealy, R., Mills, G.M., 2016. Simulating the impact of urban development pathways on the local climate: A scenario-based analysis in the greater Dublin region, Ireland. Landscape and Urban Planning 152, 72–89. https:doi.org/10.1016/j.landurbplan.2016.02.006

Alexander, P.J., Mills, G., Fealy, R., 2015. Using LCZ data to run an urban energy balance model. Urban Climate 13, 14–37. https://doi.org/10.1016/j.uclim.2015.05.001

Ali-Toudert, F., Mayer, H., 2005. Numerical study on the effects of aspect ratio and orientation of an urban street canyon on outdoor thermal comfort in hot and dry climate. Building and Environment 41, 94–108. https://doi.org/10.1016/j.buildenv.2005.01.013

Alonzo, M., Bookhagen, B., McFadden, J.P., Sun, A., Roberts, D.A., 2015. Mapping urban forest leaf area index with airborne lidar using penetration metrics and allometry. Remote Sensing of Environment 162, 141–153. https://doi.org/10.1016/j.rse.2015.02.025

Alonzo, M., Bookhagen, B., Roberts, D.A., 2014. Urban tree species mapping using hyperspectral and lidar data fusion. Remote Sensing of Environment 148, 70–83. https://doi.org/10.1016/j.rse.2014.03.018

Alonzo, M., Roth, K., Roberts, D., 2013. Identifying Santa Barbara's urban tree species from AVIRIS imagery using canonical discriminant analysis. Remote Sensing Letters 4, 513–521. https://doi.org/10.1080/2150704X.2013.764027

Amiri, R., Weng, Q., Alimohammadi, A., Alavipanah, S.K., 2009. Spatial–temporal dynamics of land surface temperature in relation to fractional vegetation cover and land use/cover in the Tabriz urban area, Iran. Remote Sensing of Environment 113, 2606–2617. https://doi.org/10.1016/j.rse.2009.07.021

Ao, X., Grimmond, C.S.B., Liu, D., Han, Z., Hu, P., Wang, Y., Zhen, X., Tan, J., 2016. Radiation Fluxes in a Business District of Shanghai, China. J. Appl. Meteor. Climatol. 55, 2451–2468. https://doi.org/10.1175/JAMC-D-16-0082.1

Armson, D., Stringer, P., Ennos, A.R., 2012. The effect of tree shade and grass on surface and globe temperatures in an urban area. Urban Forestry & Urban Greening 11, 245–255. https://doi.org/10.1016/j.ufug.2012.05.002

Arnfield, A.J., 2003. Two decades of urban climate research: a review of turbulence, exchanges of energy and water, and the urban heat island. Int. J. Climatol. 23, 1–26. https://doi.org/10.1002/joc.859

Asner, G.P., Brodrick, P.G., Anderson, C.B., Vaughn, N., Knapp, D.E., Martin, R.E., 2016. Progressive forest canopy water loss during the 2012–2015 California drought. Proceedings of the National Academy of Sciences 113, E249–E255. https://doi.org/10.1073/pnas.1523397113

Asner, G.P., Bustamante, M.M.C., Townsend, A.R., 2003. Scale dependence of biophysical structure in deforested areas bordering the Tapajós National Forest, Central Amazon. Remote Sensing of Environment, Large Scale Biosphere Atmosphere Experiment in Amazonia 87, 507–520. https://doi.org/10.1016/j.rse.2003.03.001

Bassani, C., Cavalli, R.M., Cavalcante, F., Cuomo, V., Palombo, A., Pascucci, S., Pignatti, S., 2007. Deterioration status of asbestos-cement roofing sheets assessed by analyzing hyperspectral data. Remote Sensing of Environment 109, 361–378. https://doi.org/10.1016/j.rse.2007.01.014

Bateson, C.A., Asner, G.P., Wessman, C.A., 2000. Endmember bundles: a new approach to incorporating endmember variability into spectral mixture analysis. IEEE Transactions on Geoscience and Remote Sensing 38, 1083–1094. https://doi.org/10.1109/36.841987

Bechtel, B., Zakšek, K., Hoshyaripour, G., 2012. Downscaling Land Surface Temperature in an Urban Area: A Case Study for Hamburg, Germany. Remote Sensing 4, 3184–3200. https://doi.org/10.3390/rs4103184

Behling, R., Bochow, M., Foerster, S., Roessner, S., Kaufmann, H., 2015. Automated GIS-based derivation of urban ecological indicators using hyperspectral remote sensing and height information. Ecological Indicators 48, 218–234. https://doi.org/10.1016/j.ecolind.2014.08.003

Berk, A., Anderson, G.P., Acharya, P.K., Bernstein, L.S., Muratov, L., Lee, J., Fox, M., Adler-Golden, S.M., Chetwynd, J.H., Hoke, M.L., Lockwood, R.B., Gardner, J.A., Cooley, T.W., Borel, C.C., Lewis, P.E., 2005a. MODTRAN 5: a reformulated atmospheric band model with auxiliary species and practical multiple scattering options: update, in: Algorithms and Technologies for Multispectral, Hyperspectral, and Ultraspectral Imagery XI. Presented at the Algorithms and Technologies for Multispectral, Hyperspectral, and Ultraspectral Imagery XI, International Society for Optics and Photonics, pp. 662–668. https://doi.org/10.1117/12.606026

Berman, M., Kiiveri, H., Lagerstrom, R., Ernst, A., Dunne, R., Huntington, J.F., 2004. ICE: a statistical approach to identifying endmembers in hyperspectral images. IEEE Transactions on Geoscience and Remote Sensing 42, 2085–2095. https://doi.org/10.1109/TGRS.2004.835299

Best, M.J., Grimmond, C.S.B., 2016. Modeling the Partitioning of Turbulent Fluxes at Urban Sites with Varying Vegetation Cover. Journal of Hydrometeorology 17, 2537–2553. https://doi.org/10.1175/JHM-D-15-0126.1

Bijoor, N.S., McCarthy, H.R., Zhang, D., Pataki, D.E., 2012. Water sources of urban trees in the Los Angeles metropolitan area. Urban Ecosystems 15, 195–214. https://doi.org/10.1007/s11252-011-0196-1

Bowler, D.E., Buyung-Ali, L., Knight, T.M., Pullin, A.S., 2010. Urban greening to cool towns and cities: A systematic review of the empirical evidence. Landscape and Urban Planning 97, 147–155. https://doi.org/10.1016/j.landurbplan.2010.05.006

Brook, A., Ben-Dor, E., Richter, R., 2010. Fusion of hyperspectral images and LiDAR data for civil engineering structure monitoring, in: 2010 2nd Workshop on Hyperspectral Image and Signal Processing: Evolution in Remote Sensing. Presented at the 2010 2nd Workshop on Hyperspectral Image and Signal Processing: Evolution in Remote Sensing, pp. 1–5. https://doi.org/10.1109/WHISPERS.2010.5594872

Buyantuyev, A., Wu, J., 2010. Urban heat islands and landscape heterogeneity: linking spatiotemporal variations in surface temperatures to land-cover and socioeconomic patterns. Landscape Ecology 25, 17–33. https://doi.org/10.1007/s10980-009-9402-4

Candela, L., Formaro, R., Guarini, R., Loizzo, R., Longo, F., Varacalli, G., 2016. The PRISMA mission, in: 2016 IEEE International Geoscience and Remote Sensing Symposium (IGARSS). Presented at the 2016 IEEE International Geoscience and Remote Sensing Symposium (IGARSS), pp. 253–256. https://doi.org/10.1109/IGARSS.2016.7729057

Chapin, F.S., Chapin, M.C., Matson, P.A., Vitousek, P., 2011. Principles of Terrestrial Ecosystem Ecology. Springer Science & Business Media.

Chen, Y., Su, W., Li, J., Sun, Z., 2009. Hierarchical object oriented classification using very high resolution imagery and LIDAR data over urban areas. Advances in Space Research 43, 1101–1110. https://doi.org/10.1016/j.asr.2008.11.008

Chen, Y., Wang, X., Jiang, B., Wen, Z., Yang, N., Li, L., 2017. Tree survival and growth are impacted by increased surface temperature on paved land. Landscape and Urban Planning 162, 68–79. https://doi.org/10.1016/j.landurbplan.2017.02.001

Chen, Y.-J., McFadden, J.P., Clarke, K.C., Roberts, D.A., 2015. Measuring Spatio-temporal Trends in Residential Landscape Irrigation Extent and Rate in Los Angeles, California Using

SPOT-5 Satellite Imagery. Water Resources Management 29, 5749–5763. https://doi.org/10.1007/s11269-015-1144-2

Chow, W.T.L., Volo, T.J., Vivoni, E.R., Jenerette, G.D., Ruddell, B.L., 2014. Seasonal dynamics of a suburban energy balance in Phoenix, Arizona. International Journal of Climatology 34, 3863–3880. https://doi.org/10.1002/joc.3947

Christen, A., Vogt, R., 2004. Energy and radiation balance of a central European city. Int. J. Climatol. 24, 1395–1421. https://doi.org/10.1002/joc.1074

Clarke, L.W., Jenerette, G.D., Davila, A., 2013. The luxury of vegetation and the legacy of tree biodiversity in Los Angeles, CA. Landscape and Urban Planning 116, 48–59. https://doi.org/10.1016/j.landurbplan.2013.04.006

Crum, S.M., Jenerette, G.D., 2017. Microclimate Variation among Urban Land Covers: The Importance of Vertical and Horizontal Structure in Air and Land Surface Temperature Relationships. J. Appl. Meteor. Climatol. 56, 2531–2543. https://doi.org/10.1175/JAMC-D-17-0054.1

Demuzere, M., Harshan, S., Järvi, L., Roth, M., Grimmond, C.S.B., Masson, V., Oleson, K.W., Velasco, E., Wouters, H., 2017. Impact of urban canopy models and external parameters on the modelled urban energy balance in a tropical city. Quarterly Journal of the Royal Meteorological Society 143, 1581–1596. https://doi.org/10.1002/qj.3028

Deng, C., 2016. Automated Construction of Multiple Regional Libraries for Neighborhoodwise Local Multiple Endmember Unmixing. IEEE Journal of Selected Topics in Applied Earth Observations and Remote Sensing 9, 4232–4246. https://doi.org/10.1109/JSTARS.2016.2541660

Dennison, P.E., Halligan, K.Q., Roberts, D.A., 2004. A comparison of error metrics and constraints for multiple endmember spectral mixture analysis and spectral angle mapper. Remote Sensing of Environment 93, 359–367. https://doi.org/10.1016/j.rse.2004.07.013

Dennison, P.E., Roberts, D.A., 2003. Endmember selection for multiple endmember spectral mixture analysis using endmember average RMSE. Remote Sensing of Environment 87, 123–135. https://doi.org/10.1016/S0034-4257(03)00135-4

DeOreo, B., Mayer, P., Martien, L., Hayden, M., Funk, A., Karmer-Duffield, M., Davis, R., 2011. California Single Family Water Use Efficiency Study. CA Department of Water Resources.

Diamond, H.J., Karl, T.R., Palecki, M.A., Baker, C.B., Bell, J.E., Leeper, R.D., Easterling, D.R., Lawrimore, J.H., Meyers, T.P., Helfert, M.R., Goodge, G., Thorne, P.W., 2013. U.S. Climate Reference Network after One Decade of Operations: Status and Assessment. Bull. Amer. Meteor. Soc. 94, 485–498. https://doi.org/10.1175/BAMS-D-12-00170.1

Dimoudi, A., Nikolopoulou, M., 2003. Vegetation in the urban environment: microclimatic analysis and benefits. Energy and Buildings, Special issue on urban research 35, 69–76. https://doi.org/10.1016/S0378-7788(02)00081-6

Dousset, B., Gourmelon, F., 2003. Satellite multi-sensor data analysis of urban surface temperatures and landcover. ISPRS Journal of Photogrammetry and Remote Sensing, Algorithms and Techniques for Multi-Source Data Fusion in Urban Areas 58, 43–54. https://doi.org/10.1016/S0924-2716(03)00016-9

Dudley, K.L., Dennison, P.E., Roth, K.L., Roberts, D.A., Coates, A.R., 2015. A multi-temporal spectral library approach for mapping vegetation species across spatial and temporal phenological gradients. Remote Sensing of Environment. https://doi.org/10.1016/j.rse.2015.05.004

Duursma, R.A., Barton, C.V.M., Lin, Y.-S., Medlyn, B.E., Eamus, D., Tissue, D.T., Ellsworth, D.S., McMurtrie, R.E., 2014. The peaked response of transpiration rate to vapour pressure deficit in field conditions can be explained by the temperature optimum of photosynthesis. Agricultural and Forest Meteorology 189–190, 2–10. https://doi.org/10.1016/j.agrformet.2013.12.007

Edmondson, J.L., Stott, I., Davies, Z.G., Gaston, K.J., Leake, J.R., 2016. Soil surface temperatures reveal moderation of the urban heat island effect by trees and shrubs. Sci Rep 6. https://doi.org/10.1038/srep33708

Esau, I.N., Lyons, T.J., 2002. Effect of sharp vegetation boundary on the convective atmospheric boundary layer. Agricultural and forest meteorology 114, 3–13.
Fears, D., 2016. California's drive to save water is killing trees, hurting utilities and raising taxes. Washington Post.

Feng, X., Myint, S.W., 2016. Exploring the effect of neighboring land cover pattern on land surface temperature of central building objects. Building and Environment 95, 346–354. https://doi.org/10.1016/j.buildenv.2015.09.019

Ferrato, L.-J., Forsythe, K.W., 2013. Comparing Hyperspectral and Multispectral Imagery for Land Classification of the Lower Don River, Toronto. Journal of Geography and Geology 5, p92. https://doi.org/10.5539/jgg.v5n1p92

Franke, J., Roberts, D.A., Halligan, K., Menz, G., 2009. Hierarchical Multiple Endmember Spectral Mixture Analysis (MESMA) of hyperspectral imagery for urban environments. Remote Sensing of Environment 113, 1712–1723. https://doi.org/10.1016/j.rse.2009.03.018

Friedl, M.A., 2002. Forward and inverse modeling of land surface energy balance using surface temperature measurements. Remote Sensing of Environment, Recent Advances in Remote Sensing of Biophysical Variables 79, 344–354. https://doi.org/10.1016/S0034-4257(01)00284-X

Frolking, S., Milliman, T., Seto, K.C., Friedl, M.A., 2013. A global fingerprint of macro-scale changes in urban structure from 1999 to 2009. Environmental Research Letters 8, 024004. https://doi.org/10.1088/1748-9326/8/2/024004

Fu, P., Weng, Q., 2016. A time series analysis of urbanization induced land use and land cover change and its impact on land surface temperature with Landsat imagery. Remote Sensing of Environment 175, 205–214. https://doi.org/10.1016/j.rse.2015.12.040

Gedzelman, S.D., Austin, S., Cermak, R., Stefano, N., Partridge, S., Quesenberry, S., Robinson, D.A., 2003. Mesoscale aspects of the Urban Heat Island around New York City. Theor. Appl. Climatol. 75, 29–42. https://doi.org/10.1007/s00704-002-0724-2

Gillespie, A., Rokugawa, S., Matsunaga, T., Cothern, J.S., Hook, S., Kahle, A.B., 1998. A temperature and emissivity separation algorithm for Advanced Spaceborne Thermal Emission and Reflection Radiometer (ASTER) images. IEEE Transactions on Geoscience and Remote Sensing 36, 1113–1126. https://doi.org/10.1109/36.700995

Gillner, S., Korn, S., Hofmann, M., Roloff, A., 2016. Contrasting strategies for tree species to cope with heat and dry conditions at urban sites. Urban Ecosyst 1–13. https://doi.org/10.1007/s11252-016-0636-z

Gillner, S., Vogt, J., Tharang, A., Dettmann, S., Roloff, A., 2015. Role of street trees in mitigating effects of heat and drought at highly sealed urban sites. Landscape and Urban Planning 143, 33–42. https://doi.org/10.1016/j.landurbplan.2015.06.005

Goenaga, M.A., Torres-Madronero, M.C., Velez-Reyes, M., Bloem, S.J.V., Chinea, J.D., 2013. Unmixing Analysis of a Time Series of Hyperion Images Over the Guaica Dry Forest in Puerto Rico. IEEE Journal of Selected Topics in Applied Earth Observations and Remote Sensing 6, 329–338. https://doi.org/10.1109/JSTARS.2012.2225096

Golding, N., Hewitt, C., Zhang, P., Bett, P., Fang, X., Hu, H., Nobert, S., 2017. Improving user engagement and uptake of climate services in China. Climate Services 5, 39–45. https://doi.org/10.1016/j.cliser.2017.03.004

Göttsche, F.-M., Olesen, F.S., 2001. Modelling of diurnal cycles of brightness temperature extracted from METEOSAT data. Remote Sensing of Environment 76, 337–348. https://doi.org/10.1016/S0034-4257(00)00214-5

Grabosky, J., Gilman, E., 2004. Measurement and prediction of tree growth reduction from tree planting space design in established parking lots. Journal of Arboriculture 154–164.

Green, R.O., Eastwood, M.L., Sarture, C.M., Chrien, T.G., Aronsson, M., Chippendale, B.J., Faust, J.A., Pavri, B.E., Chovit, C.J., Solis, M., Olah, M.R., Williams, O., 1998. Imaging Spectroscopy and the Airborne Visible/Infrared Imaging Spectrometer (AVIRIS). Remote Sensing of Environment 65, 227–248. https://doi.org/10.1016/S0034-4257(98)00064-9

Griffin, D., Anchukaitis, K.J., 2014. How unusual is the 2012–2014 California drought? Geophys. Res. Lett. 41, 2014GL062433. https://doi.org/10.1002/2014GL062433

Grigsby, S.P., Hulley, G.C., Roberts, D.A., Scheele, C., Ustin, S.L., Alsina, M.M., 2015. Improved surface temperature estimates with MASTER/AVIRIS sensor fusion. Remote Sensing of Environment. https://doi.org/10.1016/j.rse.2015.05.019

Grimmond, C.S.B., Blackett, M., Best, M.J., Baik, J.-J., Belcher, S.E., Beringer, J., Bohnenstengel, S.I., Calmet, I., Chen, F., Coutts, A., Dandou, A., Fortuniak, K., Gouvea, M.L., Hamdi, R., Hendry, M., Kanda, M., Kawai, T., Kawamoto, Y., Kondo, H., Krayenhoff, E.S., Lee, S.-H., Loridan, T., Martilli, A., Masson, V., Miao, S., Oleson, K., Ooka, R., Pigeon, G., Porson, A., Ryu, Y.-H., Salamanca, F., Steeneveld, G. j., Tombrou, M., Voogt, J.A., Young, D.T., Zhang, N., 2011. Initial results from Phase 2 of the international urban energy balance model comparison. International Journal of Climatology 31, 244–272. https://doi.org/10.1002/joc.2227

Grimmond, C.S.B., Blackett, M., Best, M.J., Barlow, J., Baik, J.-J., Belcher, S.E., Bohnenstengel, S.I., Calmet, I., Chen, F., Dandou, A., Fortuniak, K., Gouvea, M.L., Hamdi, R., Hendry, M., Kawai, T., Kawamoto, Y., Kondo, H., Krayenhoff, E.S., Lee, S.-H., Loridan, T., Martilli, A., Masson, V., Miao, S., Oleson, K., Pigeon, G., Porson, A., Ryu, Y.-H., Salamanca, F., Shashua-Bar, L., Steeneveld, G.-J., Tombrou, M., Voogt, J., Young, D., Zhang, N., 2010. The International Urban Energy Balance Models Comparison Project: First Results from Phase 1. Journal of Applied Meteorology and Climatology 49, 1268–1292. https://doi.org/10.1175/2010JAMC2354.1

Grimmond, C.S.B., Cleugh, H.A., Oke, T.R., 1991. An objective urban heat storage model and its comparison with other schemes. Atmospheric Environment. Part B. Urban Atmosphere 25, 311–326. https://doi.org/10.1016/0957-1272(91)90003-W

Grimmond, C.S.B., Oke, T.R., 2002. Turbulent Heat Fluxes in Urban Areas: Observations and a Local-Scale Urban Meteorological Parameterization Scheme (LUMPS). J. Appl. Meteor. 41, 792–810. https://doi.org/10.1175/1520-0450(2002)041<0792:THFIUA>2.0.CO;2

Grimmond, C.S.B., Oke, T.R., 1999. Evapotranspiration rates in urban areas. IAHS PUBLICATION 259, 235–244.

Grimmond, C.S.B., Oke, T.R., 1995. Comparison of Heat Fluxes from Summertime Observations in the Suburbs of Four North American Cities. J. Appl. Meteor. 34, 873–889. https://doi.org/10.1175/1520-0450(1995)034<0873:COHFFS>2.0.CO;2

Grimmond, C.S.B., Oke, T.R., 1991. An evapotranspiration-interception model for urban areas. Water Resour. Res. 27, 1739–1755. https://doi.org/10.1029/91WR00557

Grimmond, C.S.B., Oke, T.R., Steyn, D.G., 1986. Urban Water Balance: 1. A Model for Daily Totals. Water Resour. Res. 22, 1397–1403. https://doi.org/10.1029/WR022i010p01397

Grimmond, C.S.B., Souch, C., Hubble, M.D., 1996. Influence of tree cover on summer-time surface energy balance fluxes, San Gabriel Valley, Los Angeles. Climate Research 6, 45–57.

Gu, H., Singh, A., Townsend, P.A., 2015. Detection of gradients of forest composition in an urban area using imaging spectroscopy. Remote Sensing of Environment, Special Issue on the Hyperspectral Infrared Imager (HyspIRI) 167, 168–180. https://doi.org/10.1016/j.rse.2015.06.010

Guanter, L., Kaufmann, H., Segl, K., Foerster, S., Rogass, C., Chabrillat, S., Kuester, T., Hollstein, A., Rossner, G., Chlebek, C., Straif, C., Fischer, S., Schrader, S., Storch, T., Heiden, U., Mueller, A., Bachmann, M., Mühle, H., Müller, R., Habermeyer, M., Ohndorf, A., Hill, J., Buddenbaum, H., Hostert, P., van der Linden, S., Leitão, P.J., Rabe, A., Doerffer, R., Krasemann, H., Xi, H., Mauser, W., Hank, T., Locherer, M., Rast, M., Staenz, K., Sang, B., 2015. The EnMAP Spaceborne Imaging Spectroscopy Mission for Earth Observation. Remote Sensing 7, 8830–8857. https://doi.org/10.3390/rs70708830

Guerschman, J.P., Hill, M.J., Renzullo, L.J., Barrett, D.J., Marks, A.S., Botha, E.J., 2009. Estimating fractional cover of photosynthetic vegetation, non-photosynthetic vegetation and bare soil in the Australian tropical savanna region upscaling the EO-1 Hyperion and MODIS sensors. Remote Sensing of Environment 113, 928–945. https://doi.org/10.1016/j.rse.2009.01.006

Hamlin, L., Green, R.O., Mouroulis, P., Eastwood, M., Wilson, D., Dudik, M., Paine, C., 2011. Imaging spectrometer science measurements for Terrestrial Ecology: AVIRIS and new developments, in: 2011 IEEE Aerospace Conference. Presented at the 2011 IEEE Aerospace Conference, pp. 1–7. https://doi.org/10.1109/AERO.2011.5747395

Heiden, U., Heldens, W., Roessner, S., Segl, K., Esch, T., Mueller, A., 2012. Urban structure type characterization using hyperspectral remote sensing and height information. Landscape and Urban Planning 105, 361–375. https://doi.org/10.1016/j.landurbplan.2012.01.001

Heiden, U., Segl, K., Roessner, S., Kaufmann, H., 2007. Determination of robust spectral features for identification of urban surface materials in hyperspectral remote sensing data. Remote Sensing of Environment 111, 537–552. https://doi.org/10.1016/j.rse.2007.04.008

Herold, M., Gardner, M.E. and Roberts, D.A., 2003. Spectral resolution requirements for mapping urban areas. IEEE Transactions on Geoscience and remote sensing, 41(9), pp.1907-1919. https://doi.org/10.1016/j.rse.2004.02.013

Herold, M., Roberts, D., Noronha, V., Smadi, O., 2008. Imaging spectrometry and asphalt road surveys. Transportation Research Part C: Emerging Technologies 16, 153–166. https://doi.org/10.1016/j.trc.2007.07.001

Herold, M., Roberts, D.A., Gardner, M.E., Dennison, P.E., 2004. Spectrometry for urban area remote sensing—Development and analysis of a spectral library from 350 to 2400 nm. Remote Sensing of Environment 91, 304–319. https://doi.org/10.1016/j.rse.2004.02.013

Hodgson, M.E., Jensen, J.R., Tullis, J.A., Riordan, K.D., Archer, C.M., 2003. Synergistic Use of Lidar and Color Aerial Photography for Mapping Urban Parcel Imperviousness. Photogrammetric Engineering & Remote Sensing 69, 973–980. https://doi.org/10.14358/PERS.69.9.973

Hook, S.J., Myers, J.J., Thome, K.J., Fitzgerald, M., Kahle, A.B., 2001. The MODIS/ASTER airborne simulator (MASTER) — a new instrument for earth science studies. Remote Sensing of Environment 76, 93–102. https://doi.org/10.1016/S0034-4257(00)00195-4

Hu, X.-M., Xue, M., 2015. Influence of Synoptic Sea-Breeze Fronts on the Urban Heat Island Intensity in Dallas–Fort Worth, Texas. Mon. Wea. Rev. 144, 1487–1507. https://doi.org/10.1175/MWR-D-15-0201.1

Intergovernmental Panel on Climate Change, Edenhofer, O. (Eds.), 2014. Climate change 2014: mitigation of climate change: Working Group III contribution to the Fifth Assessment Report of the Intergovernmental Panel on Climate Change. Cambridge University Press, New York, NY.

Järvi, L., in Prep. Study of Helsinki Urban Energy Balance.

Järvi, L., Grimmond, C.S.B., Christen, A., 2011. The Surface Urban Energy and Water Balance Scheme (SUEWS): Evaluation in Los Angeles and Vancouver. Journal of Hydrology 411, 219–237. https://doi.org/10.1016/j.jhydrol.2011.10.001

Jenerette, G.D., Harlan, S.L., Brazel, A., Jones, N., Larsen, L., Stefanov, W.L., 2007. Regional relationships between surface temperature, vegetation, and human settlement in a rapidly urbanizing ecosystem. Landscape Ecol 22, 353–365. https://doi.org/10.1007/s10980-006-9032-z

Jenerette, G.D., Harlan, S.L., Buyantuev, A., Stefanov, W.L., Declet-Barreto, J., Ruddell, B.L., Myint, S.W., Kaplan, S., Li, X., 2016. Micro-scale urban surface temperatures are related to land-cover features and residential heat related health impacts in Phoenix, AZ USA. Landscape Ecol 31, 745–760. https://doi.org/10.1007/s10980-015-0284-3

Jenerette, G.D., Miller, G., Buyantuev, A., Pataki, D.E., Gillespie, T.W., Pincetl, S., 2013. Urban vegetation and income segregation in drylands: a synthesis of seven metropolitan regions in the southwestern United States. Environ. Res. Lett. 8, 044001. https://doi.org/10.1088/1748-9326/8/4/044001

Jensen, J.R., 2009. Remote sensing of the environment: An earth resource perspective, 2nd ed. Pearson Education India.

Jensen, J.R., Cowen, D.C., 1999. Remote sensing of urban/suburban infrastructure and socio-economic attributes. Photogrammetric engineering and remote sensing 65, 611–622.

Jensen, J.R., Im, J., 2007. Remote Sensing Change Detection in Urban Environments, in: Jensen, D.R.R., Gatrell, D.J.D., McLean, D.D. (Eds.), Geo-Spatial Technologies in Urban Environments. Springer Berlin Heidelberg, pp. 7–31. https://doi.org/10.1007/978-3-540-69417-5_2

Kailath, T., 1967. The Divergence and Bhattacharyya Distance Measures in Signal Selection. IEEE Trans. Communication Theory 52–60. https://doi.org/10.1109/TCOM.1967.1089532

Kanda, M., Inagaki, A., Miyamoto, T., Gryschka, M., Raasch, S., 2013. A New Aerodynamic Parametrization for Real Urban Surfaces. Boundary-Layer Meteorology 148, 357–377. https://doi.org/10.1007/s10546-013-9818-x

Karsisto, P., Fortelius, C., Demuzere, M., Grimmond, C.S.B., Oleson, K.W., Kouznetsov, R., Masson, V., Järvi, L., 2016. Seasonal surface urban energy balance and wintertime stability simulated using three land-surface models in the high-latitude city Helsinki. Quarterly Journal of the Royal Meteorological Society 142, 401–417. https://doi.org/10.1002/qj.2659

Kaufmann, J.E., 1994. Principles of turfgrass growth and development, in: Leslie, A.R. (Ed.), Handbook of Integrated Pest Management for Turf and Ornamentals. Lewis, USA, pp. 91–98.

Keith, D.J., Walker, H.A., Paul, J.F., 2002. Terrestrial vegetation greenness of the Lower Galveston Bay watershed from satellite remote sensing and its relation to water use and the salinity regime of the Galveston Bay Estuary (USA). International Journal of Remote Sensing 23, 905–916. https://doi.org/10.1080/01431160110040486

Kent, C.W., Grimmond, S., Barlow, J., Gatey, D., Kotthaus, S., Lindberg, F., Halios, C.H., 2017. Evaluation of Urban Local-Scale Aerodynamic Parameters: Implications for the Vertical Profile of Wind Speed and for Source Areas. Boundary-Layer Meteorol 164, 183–213. https://doi.org/10.1007/s10546-017-0248-z

Kjelgren, R., Montague, T., 1998. Urban tree transpiration over turf and asphalt surfaces. Atmospheric Environment, Conference on the Benefits of the Urban Forest 32, 35–41. https://doi.org/10.1016/S1352-2310(97)00177-5

Kjelgren, R., Rupp, L., Kilgren, D., 2000. Water Conservation in Urban Landscapes. HortScience 35, 1037–1040.

Kotthaus, S., Smith, T.E.L., Wooster, M.J., Grimmond, C.S.B., 2014. Derivation of an urban materials spectral library through emittance and reflectance spectroscopy. ISPRS Journal of Photogrammetry and Remote Sensing 94, 194–212. https://doi.org/10.1016/j.isprsjprs.2014.05.005

Labate, D., Ceccherini, M., Cisbani, A., De Cosmo, V., Galeazzi, C., Giunti, L., Melozzi, M., Pieraccini, S., Stagi, M., 2009. The PRISMA payload optomechanical design, a high performance instrument for a new hyperspectral mission. Acta Astronautica 65, 1429–1436. https://doi.org/10.1016/j.actaastro.2009.03.077

Lagouarde, J.-P., Moreau, P., Irvine, M., Bonnefond, J.-M., Voogt, J.A., Solliec, F., 2004. Airborne experimental measurements of the angular variations in surface temperature over urban areas: case study of Marseille (France). Remote Sensing of Environment 93, 443–462. https://doi.org/10.1016/j.rse.2003.12.011

Lee, C.M., Cable, M.L., Hook, S.J., Green, R.O., Ustin, S.L., Mandl, D.J., Middleton, E.M., 2015. An introduction to the NASA Hyperspectral InfraRed Imager (HyspIRI) mission and preparatory activities. Remote Sensing of Environment. https://doi.org/10.1016/j.rse.2015.06.012

Leuzinger, S., Vogt, R., Körner, C., 2010. Tree surface temperature in an urban environment. Agricultural and Forest Meteorology 150, 56–62. https://doi.org/10.1016/j.agrformet.2009.08.006

Li, Z.-L., Tang, B.-H., Wu, H., Ren, H., Yan, G., Wan, Z., Trigo, I.F., Sobrino, J.A., 2013. Satellite-derived land surface temperature: Current status and perspectives. Remote Sensing of Environment 131, 14–37.

Liang, S., Wang, K., Zhang, X., Wild, M., 2010. Review on Estimation of Land Surface Radiation and Energy Budgets From Ground Measurement, Remote Sensing and Model Simulations. IEEE Journal of Selected Topics in Applied Earth Observations and Remote Sensing 3, 225–240. https://doi.org/10.1109/JSTARS.2010.2048556

Lindberg, F., Grimmond, C.S.B., 2011. The influence of vegetation and building morphology on shadow patterns and mean radiant temperatures in urban areas: model development and evaluation. Theor Appl Climatol 105, 311–323. https://doi.org/10.1007/s00704-010-0382-8

Lindberg, F., Grimmond, C.S.B., Gabey, A., Huang, B., Kent, C.W., Sun, T., Theeuwes, N.E., Järvi, L., Ward, H.C., Capel-Timms, I., Chang, Y., Jonsson, P., Krave, N., Liu, D., Meyer, D., Olofson, K.F.G., Tan, J., Wästberg, D., Xue, L., Zhang, Z., 2018. Urban Multi-scale Environmental Predictor (UMEP): An integrated tool for city-based climate services. Environmental Modelling & Software 99, 70–87. https://doi.org/10.1016/j.envsoft.2017.09.020

Litvak, E., Bijoor, N.S., Pataki, D.E., 2014. Adding trees to irrigated turfgrass lawns may be a water-saving measure in semi-arid environments. Ecohydrol. 7, 1314–1330. https://doi.org/10.1002/eco.1458

Liu, K., Fang, J., Zhao, D., Liu, X., Zhang, X., Wang, X., Li, X., 2016. An Assessment of Urban Surface Energy Fluxes Using a Sub-Pixel Remote Sensing Analysis: A Case Study in

Suzhou, China. ISPRS International Journal of Geo-Information 5, 11. https://doi.org/10.3390/ijgi5020011

Liu, T., Yang, X., 2015. Monitoring land changes in an urban area using satellite imagery, GIS and landscape metrics. Applied Geography 56, 42–54. https://doi.org/10.1016/j.apgeog.2014.10.002

Livesley, S.J., McPherson, G.M., Calfapietra, C., 2016. The Urban Forest and Ecosystem Services: Impacts on Urban Water, Heat, and Pollution Cycles at the Tree, Street, and City Scale. Journal of Environment Quality 45, 119. https://doi.org/10.2134/jeq2015.11.0567

Loridan, T., Grimmond, C.S.B., Offerle, B.D., Young, D.T., Smith, T.E.L., Järvi, L., Lindberg, F., 2010. Local-Scale Urban Meteorological Parameterization Scheme (LUMPS): Longwave Radiation Parameterization and Seasonality-Related Developments. J. Appl. Meteor. Climatol. 50, 185–202. https://doi.org/10.1175/2010JAMC2474.1

Los Angeles County GIS, 2014. Countywide building outlines-public domain release.

Los Angeles Regional Imagery Acquisition Consortium, 2016. 3-foot Digital Surface Model (DSM) – LARIAC4.

MacDonald, D.H., Crossman, N.D., Mahmoudi, P., Taylor, L.O., Summers, D.M., Boxall, P.C., 2010. The value of public and private green spaces under water restrictions. Landscape and Urban Planning 95, 192–200. https://doi.org/10.1016/j.landurbplan.2010.01.003

MacLachlan, A., Roberts, G., Biggs, E., Boruff, B., 2017. Subpixel land-cover classification for improved urban area estimates using Landsat. International Journal of Remote Sensing 38, 5763–5792. https://doi.org/10.1080/01431161.2017.1346403

McCarthy, H.R., Pataki, D.E., 2010. Drivers of variability in water use of native and non-native urban trees in the greater Los Angeles area. Urban Ecosyst 13, 393–414. https://doi.org/10.1007/s11252-010-0127-6

McPherson, E.G., Simpson, J.R., Xiao, Q., Wu, C., 2011. Million trees Los Angeles canopy cover and benefit assessment. Landscape and Urban Planning 99, 40–50. https://doi.org/10.1016/j.landurbplan.2010.08.011

McPherson, E.G., Xiao, Q., van Doorn, N.S., de Goede, J., Bjorkman, J., Hollander, A., Boynton, R.M., Quinn, J.F., Thorne, J.H., 2017. The structure, function and value of urban forests in California communities. Urban Forestry & Urban Greening 28, 43–53. https://doi.org/10.1016/j.ufug.2017.09.013

McPherson, G.E., Simpson, J.R., Xiao, Q., Chunxia, W., 2008. Los Angeles 1-million tree canopy cover assessment.

Meister, G., Rothkirch, A., Spitzer, H., Bienlein, J., 2000. BRDF field studies for remote sensing of urban areas. Remote Sensing Reviews 19, 37–57. https://doi.org/10.1080/02757250009532409

Milesi, C., Running, S.W., Elvidge, C.D., Dietz, J.B., Tuttle, B.T., Nemani, R.R., 2005. Mapping and Modeling the Biogeochemical Cycling of Turf Grasses in the United States. Environmental Management 36, 426–438. https://doi.org/10.1007/s00267-004-0316-2

Mini, C., Hogue, T.S., Pincetl, S., 2015. The effectiveness of water conservation measures on summer residential water use in Los Angeles, California. Resources, Conservation and Recycling 94, 136–145. https://doi.org/10.1016/j.resconrec.2014.10.005

Mini, C., Hogue, T.S., Pincetl, S., 2014. Estimation of residential outdoor water use in Los Angeles, California. Landscape and Urban Planning 127, 124–135. https://doi.org/10.1016/j.landurbplan.2014.04.007

Monteith, J.L., 1965. Evaporation and environment. Symp. Soc. Exp. Biol. 19, 205–234.

Moonen, P., Defraeye, T., Dorer, V., Blocken, B., Carmeliet, J., 2012. Urban Physics: Effect of the micro-climate on comfort, health and energy demand. Frontiers of Architectural Research 1, 197–228. https://doi.org/10.1016/j.foar.2012.05.002

Morabito, M., Crisci, A., Messeri, A., Orlandini, S., Raschi, A., Maracchi, G., Munafò, M., 2016. The impact of built-up surfaces on land surface temperatures in Italian urban areas. Science of The Total Environment 551–552, 317–326. https://doi.org/10.1016/j.scitotenv.2016.02.029

Moran, M.S., 2004. Thermal infrared measurement as an indicator of plant ecosystem health. Thermal remote sensing in land surface processes / edited by Dale A. Quattrochi and Jeffrey C. Luvall.

Mushore, T.D., Odindi, J., Dube, T., Matongera, T.N., Mutanga, O., 2017. Remote sensing applications in monitoring urban growth impacts on in-and-out door thermal conditions: A review. Remote Sensing Applications: Society and Environment 8, 83–93. https://doi.org/10.1016/j.rsase.2017.08.001

Myint, S.W., Gober, P., Brazel, A., Grossman-Clarke, S., Weng, Q., 2011. Per-pixel vs. object-based classification of urban land cover extraction using high spatial resolution imagery. Remote Sensing of Environment 115, 1145–1161. https://doi.org/10.1016/j.rse.2010.12.017

Myint, S.W., Okin, G.S., 2009. Modelling land-cover types using multiple endmember spectral mixture analysis in a desert city. International Journal of Remote Sensing 30, 2237–2257. https://doi.org/10.1080/01431160802549328

Myint, S.W., Wentz, E.A., Brazel, A.J., Quattrochi, D.A., 2013. The impact of distinct anthropogenic and vegetation features on urban warming. Landscape Ecol 28, 959–978. https://doi.org/10.1007/s10980-013-9868-y

Myint, S.W., Zheng, B., Talen, E., Fan, C., Kaplan, S., Middel, A., Smith, M., Huang, H.-P., Brazel, A., 2015. Does the spatial arrangement of urban landscape matter? Examples of urban warming and cooling in Phoenix and Las Vegas. Ecosystem Health and Sustainability 1, art15. https://doi.org/10.1890/EHS14-0028.1

Nagler, P.L., Daughtry, C.S.T., Goward, S.N., 2000. Plant Litter and Soil Reflectance. Remote Sensing of Environment 71, 207–215. https://doi.org/10.1016/S0034-4257(99)00082-6

National Academies of Sciences, Engineering, and Medicine, Committee on the Decadal Survey for Earth Science and Applications from Space, Space Studies Board, Division on Engineering and Physical Sciences, 2018. Thriving on Our Changing Planet: A Decadal Strategy for Earth Observation from Space. National Academies Press, Washington, D.C. https://doi.org/10.17226/24938

Nordbo, A., Karsisto, P., Matikainen, L., Wood, C.R., Järvi, L., 2015. Urban surface cover determined with airborne lidar at 2m resolution – Implications for surface energy balance modelling. Urban Climate 13, 52–72. https://doi.org/10.1016/j.uclim.2015.05.004

Nouri, H., Beecham, S., Kazemi, F., Hassanli, A.M., 2013. A review of ET measurement techniques for estimating the water requirements of urban landscape vegetation. Urban Water Journal 10, 247–259. https://doi.org/10.1080/1573062X.2012.726360

Nowak, D.J., Noble, M.H., Sisinni, S.M., Dwyer, J.F., 2001. People and Trees: Assessing the US Urban Forest Resource. Journal of Forestry 99, 37–42.

Offerle, B., Grimmond, C.S.B., Oke, T.R., 2003. Parameterization of Net All-Wave Radiation for Urban Areas. Journal of Applied Meteorology 42, 1157–1173. https://doi.org/10.1175/1520-0450(2003)042<1157:PONARF>2.0.CO;2

Oke, T.R., 1988. The urban energy balance. Progress in Physical Geography: Earth and Environment 12, 471–508. https://doi.org/10.1177/030913338801200401

Oke, T.R., 1987. Boundary Layer Climates. Psychology Press.

Oke, T.R., 1979. Advectively-assisted evapotranspiration from irrigated urban vegetation. Boundary-Layer Meteorol 17, 167–173. https://doi.org/10.1007/BF00117976

Oke, T.R., Cleugh, H.A., 1987. Urban heat storage derived as energy balance residuals. Boundary-Layer Meteorology 39, 233–245. https://doi.org/10.1007/BF00116120

Oke, T.R., Mills, G., Christen, A., Voogt, J.A., 2017. Urban Climates. Cambridge University Press.

Okujeni, A., van der Linden, S., Hostert, P., 2015. Extending the vegetation–impervious–soil model using simulated EnMAP data and machine learning. Remote Sensing of Environment 158, 69–80. https://doi.org/10.1016/j.rse.2014.11.009

Okujeni, A., van der Linden, S., Tits, L., Somers, B., Hostert, P., 2013. Support vector regression and synthetically mixed training data for quantifying urban land cover. Remote Sensing of Environment 137, 184–197. https://doi.org/10.1016/j.rse.2013.06.007.

Ollinger, S.V., 2011. Sources of variability in canopy reflectance and the convergent properties of plants. New Phytologist 189, 375–394. https://doi.org/10.1111/j.1469-8137.2010.03536.x

Onomura, S., Grimmond, C.S.B., Lindberg, F., Holmer, B., Thorsson, S., 2015. Meteorological forcing data for urban outdoor thermal comfort models from a coupled convective boundary layer and surface energy balance scheme. Urban Climate 11, 1–23. https://doi.org/10.1016/j.uclim.2014.11.001

Pataki, D.E., Boone, C.G., Hogue, T.S., Jenerette, G.D., McFadden, J.P., Pincetl, S., 2011. Socio-ecohydrology and the urban water challenge. Ecohydrol. 4, 341–347. https://doi.org/10.1002/eco.209

Pataki, D.E., McCarthy, H.R., Litvak, E., Pincetl, S., 2010. Transpiration of urban forests in the Los Angeles metropolitan area. Ecological Applications 21, 661–677. https://doi.org/10.1890/09-1717.1

Penman, H.L., 1948. Natural evaporation from open water, bare soil and grass. Proc. R. Soc. Lond. A 193, 120–145. https://doi.org/10.1098/rspa.1948.0037

Peters, E.B., Hiller, R.V., McFadden, J.P., 2011. Seasonal contributions of vegetation types to suburban evapotranspiration. Journal of Geophysical Research: Biogeosciences 116. https://doi.org/10.1029/2010JG001463

Peters, E.B., McFadden, J.P., 2010. Influence of seasonality and vegetation type on suburban microclimates. Urban Ecosyst 13, 443–460. https://doi.org/10.1007/s11252-010-0128-5

Pigeon, G., Lemonsu, A., Long, N., Barrié, J., Masson, V., Durand, P., 2006. Urban Thermodynamic Island in a Coastal City Analysed from an Optimized Surface Network. Boundary-Layer Meteorol 120, 315–351. https://doi.org/10.1007/s10546-006-9050-z
Pinho, O.S., Orgaz, M.D.M., 2000. The urban heat island in a small city in coastal Portugal. Int J Biometeorol 44, 198–203. https://doi.org/10.1007/s004840000063

Plaza, A., Martinez, P., Perez, R., Plaza, J., 2004. A quantitative and comparative analysis of endmember extraction algorithms from hyperspectral data. IEEE Transactions on Geoscience and Remote Sensing 42, 650–663. https://doi.org/10.1109/TGRS.2003.820314

Potchter, O., Cohen, P., Bitan, A., 2006. Climatic behavior of various urban parks during hot and humid summer in the mediterranean city of Tel Aviv, Israel. Int. J. Climatol. 26, 1695–1711. https://doi.org/10.1002/joc.1330

Powell, R., 2011. Characterizing Urban Subpixel Composition Using Spectral Mixture Analysis, in: Yang, X. (Ed.), Urban Remote Sensing: Monitoring, Synthesis and Modeling in the Urban Environment. John Wiley & Sons, Ltd, Chichester, UK, pp. 111–128.

Powell, R.L., Roberts, D.A., 2008. Characterizing Variability of the Urban Physical Environment for a Suite of Cities in Rondônia, Brazil. Earth Interact. 12, 1–32. https://doi.org/10.1175/2008EI246.1

Powell, R.L., Roberts, D.A., Dennison, P.E., Hess, L.L., 2007. Sub-pixel mapping of urban land cover using multiple endmember spectral mixture analysis: Manaus, Brazil. Remote Sensing of Environment 106, 253–267. https://doi.org/10.1016/j.rse.2006.09.005.

PwC (PricewaterhouesCoopers). 2014. “Anticipating Problems, Finding Solutions: Global Annual Review 2014.”

Priestnall, G., Jaafar, J., Duncan, A., 2000. Extracting urban features from LiDAR digital surface models. Computers, Environment and Urban Systems 24, 65–78. https://doi.org/10.1016/S0198-9715(99)00047-2

Quattrochi, D.A., Ridd, M.K., 1998. Analysis of vegetation within a semi-arid urban environment using high spatial resolution airborne thermal infrared remote sensing data. Atmospheric Environment, Conference on the Benefits of the Urban Forest 32, 19–33. https://doi.org/10.1016/S1352-2310(97)00179-9

Rafael, S., Martins, H., Sá, E., Carvalho, D., Borrego, C., Lopes, M., 2016. Influence of urban resilience measures in the magnitude and behaviour of energy fluxes in the city of Porto (Portugal) under a climate change scenario. Science of The Total Environment 566–567, 1500–1510. https://doi.org/10.1016/j.scitotenv.2016.06.037

Ramamurthy, P., Bou-Zeid, E., 2014. Contribution of impervious surfaces to urban evaporation. Water Resources Research 50, 2889–2902. https://doi.org/10.1002/2013WR013909

Rashed, T., Weeks, J.R., Roberts, D., Rogan, J., Powell, R., 2003. Measuring the Physical Composition of Urban Morphology Using Multiple Endmember Spectral Mixture Models. Photogrammetric Engineering & Remote Sensing 69, 1011–1020. https://doi.org/10.14358/PERS.69.9.1011

Ribeiro da Luz, B., Crowley, J.K., 2007. Spectral reflectance and emissivity features of broad leaf plants: Prospects for remote sensing in the thermal infrared (8.0–14.0 μm). Remote Sensing of Environment 109, 393–405. https://doi.org/10.1016/j.rse.2007.01.008

Ridd, M.K., 1995. Exploring a V-I-S (vegetation-impervious surface-soil) model for urban ecosystem analysis through remote sensing: comparative anatomy for cities†. International Journal of Remote Sensing 16, 2165–2185. https://doi.org/10.1080/01431169508954549

Roberts, D., Alonzo, M., Wetherley, E.B., Dudley, K.L., Dennison, P.E., 2017. Multiscale Analysis of Urban Areas Using Mixing Models. Integrating Scale in Remote Sensing and GIS 247.

Roberts, D.A., Dennison, P.E., Gardner, M.E., Hetzel, Y., Ustin, S.L., Lee, C.T., 2003. Evaluation of the potential of Hyperion for fire danger assessment by comparison to the Airborne Visible/Infrared Imaging Spectrometer. IEEE Transactions on Geoscience and Remote Sensing 41, 1297–1310. https://doi.org/10.1109/TGRS.2003.812904

Roberts, D.A., Dennison, P.E., Roth, K.L., Dudley, K., Hulley, G., 2015. Relationships between dominant plant species, fractional cover and Land Surface Temperature in a Mediterranean ecosystem. Remote Sensing of Environment 167, 152–167. https://doi.org/10.1016/j.rse.2015.01.026

Roberts, D.A., Gardner, M., Church, R., Ustin, S., Scheer, G., Green, R.O., 1998. Mapping Chaparral in the Santa Monica Mountains Using Multiple Endmember Spectral Mixture Models. Remote Sensing of Environment 65, 267–279. https://doi.org/10.1016/S0034-4257(98)00037-6

Roberts, D.A., Quattrochi, D.A., Hulley, G.C., Hook, S.J., Green, R.O., 2012. Synergies between VSWIR and TIR data for the urban environment: An evaluation of the potential for the Hyperspectral Infrared Imager (HyspIRI) Decadal Survey mission. Remote Sensing of Environment 117, 83–101. https://doi.org/10.1016/j.rse.2011.07.021

Roberts, D.A., Ustin, S.L., Ogunjemiyo, S., Greenberg, J., Dobrowski, S.Z., Chen, J., Hinckley, T.M., 2004. Spectral and Structural Measures of Northwest Forest Vegetation at Leaf to Landscape Scales. Ecosystems 545–562. https://doi.org/10.1007/s10021-004-0144-5

Roberts, S.M., Oke, T.R., Grimmond, C.S.B., Voogt, J.A., 2006. Comparison of Four Methods to Estimate Urban Heat Storage. J. Appl. Meteor. Climatol. 45, 1766–1781. https://doi.org/10.1175/JAM2432.1

Roessner, S., Segl, K., Heiden, U., Kaufmann, H., 2001. Automated differentiation of urban surfaces based on airborne hyperspectral imagery. IEEE Transactions on Geoscience and Remote Sensing 39, 1525–1532. https://doi.org/10.1109/36.934082

Rose, L.S., Akbari, H., Taha, H., 2003. Characterizing the fabric of the urban environment: A case study of Greater Houston, Texas.

Roth, K.L., Dennison, P.E., Roberts, D.A., 2012. Comparing EM selection techniques for accurate mapping of plant species and land cover using imaging spectrometer data. Remote Sensing of Environment 127, 139–152. https://doi.org/10.1016/j.rse.2012.08.030

Roth, M., Oke, T.R., Emery, W.J., 1989. Satellite-derived urban heat islands from three coastal cities and the utilization of such data in urban climatology. International Journal of Remote Sensing 10, 1699–1720. https://doi.org/10.1080/01431168908904002

Sahagun, L., 2017. The trees that make Southern California shady and green are dying. Fast. Los Angeles Times.

Sandholt, I., Rasmussen, K., Andersen, J., 2002. A simple interpretation of the surface temperature/vegetation index space for assessment of surface moisture status. Remote Sensing of Environment, Recent Advances in Remote Sensing of Biophysical Variables 79, 213–224. https://doi.org/10.1016/S0034-4257(01)00274-7

Schaaf, A.N., Dennison, P.E., Fryer, G.K., Roth, K.L., Roberts, D.A., 2011. Mapping Plant Functional Types at Multiple Spatial Resolutions Using Imaging Spectrometer Data. GIScience & Remote Sensing 48, 324–344. https://doi.org/10.2747/1548-1603.48.3.324

Schwarz, K., Fragkias, M., Boone, C.G., Zhou, W., McHale, M., Grove, J.M., O'Neil-Dunne, J., McFadden, J.P., Buckley, G.L., Childers, D., Ogden, L., Pincetl, S., Pataki, D., Whitmer, A., Cadenasso, M.L., 2015. Trees Grow on Money: Urban Tree Canopy Cover and Environmental Justice. PLOS ONE 10, e0122051. https://doi.org/10.1371/journal.pone.0122051

Selva, M., Aiazzi, B., Butera, F., Chiarantini, L., Baronti, S., 2015. Hyper-Sharpening: A First Approach on SIM-GA Data. IEEE Journal of Selected Topics in Applied Earth Observations and Remote Sensing 8, 3008–3024. https://doi.org/10.1109/JSTARS.2015.2440092

Settle, J.J., Drake, N.A., 1993. Linear mixing and the estimation of ground cover proportions. International Journal of Remote Sensing 14, 1159–1177. https://doi.org/10.1080/01431169308904402

Shivers, S.W., Roberts, D.A., McFadden, J.P., 2018. Using paired thermal and hyperspectral aerial imagery to explore land surface temperature variability and assess stress within California orchards.

Sims, D.A., Brzostek, E.R., Rahman, A.F., Dragoni, D., Phillips, R.P., 2014. An improved approach for remotely sensing water stress impacts on forest C uptake. Global Change Biology 20, 2856–2866. https://doi.org/10.1111/gcb.12537

Skamarock, W.C., Klemp, J.B., 2008. A time-split nonhydrostatic atmospheric model for weather research and forecasting applications. Journal of Computational Physics, Predicting

weather, climate and extreme events 227, 3465–3485. https://doi.org/10.1016/j.jcp.2007.01.037

Small, C., 2001. Estimation of urban vegetation abundance by spectral mixture analysis. International Journal of Remote Sensing 22, 1305–1334. https://doi.org/10.1080/01431160151144369

Smith, C., Levermore, G., 2008. Designing urban spaces and buildings to improve sustainability and quality of life in a warmer world. Energy Policy, Foresight Sustainable Energy Management and the Built Environment Project 36, 4558–4562. https://doi.org/10.1016/j.enpol.2008.09.011

Sobrino, J.A., Oltra-Carrió, R., Jiménez-Muñoz, J.C., Julien, Y., Sòria, G., Franch, B., Mattar, C., 2012. Emissivity mapping over urban areas using a classification-based approach: Application to the Dual-use European Security IR Experiment (DESIREX). International Journal of Applied Earth Observation and Geoinformation 18, 141–147. https://doi.org/10.1016/j.jag.2012.01.022

Soer, G.J.R., 1980. Estimation of regional evapotranspiration and soil moisture conditions using remotely sensed crop surface temperatures. Remote Sensing of Environment 9, 27–45. https://doi.org/10.1016/0034-4257(80)90045-0

Somers, B., Asner, G.P., Tits, L., Coppin, P., 2011. Endmember variability in Spectral Mixture Analysis: A review. Remote Sensing of Environment 115, 1603–1616. https://doi.org/10.1016/j.rse.2011.03.003

Somers, B., Tits, L., Roberts, D., Wetherley, E., 2016. Chapter 17 - Endmember Library Approaches to Resolve Spectral Mixing Problems in Remotely Sensed Data: Potential, Challenges, and Applications, in: Ruckebusch, C. (Ed.), Data Handling in Science and Technology, Resolving Spectral Mixtures With Applications from Ultrafast Time-Resolved Spectroscopy to Super-Resolution Imaging. Elsevier, pp. 551–577. https://doi.org/10.1016/B978-0-444-63638-6.00017-6

Somers, B., Zortea, M., Plaza, A., Asner, G.P., 2012. Automated Extraction of Image-Based Endmember Bundles for Improved Spectral Unmixing. IEEE Journal of Selected Topics in Applied Earth Observations and Remote Sensing 5, 396–408. https://doi.org/10.1109/JSTARS.2011.2181340

Song, C., 2004. Cross-sensor calibration between Ikonos and Landsat ETM+ for spectral mixture analysis. IEEE Geoscience and Remote Sensing Letters 1, 272–276. https://doi.org/10.1109/LGRS.2004.832227

Souch, C.A., Souch, C., 1993. The effect of trees on summertime below canopy urban climates: a case study Bloomington, Indiana. Journal of Arboriculture 19, 303–312.

Stein, D., 2003. Application of the normal compositional model to the analysis of hyperspectral imagery, in: IEEE Workshop on Advances in Techniques for Analysis of Remotely Sensed Data, 2003. Presented at the IEEE Workshop on Advances in Techniques for Analysis of Remotely Sensed Data, 2003, pp. 44–51. https://doi.org/10.1109/WARSD.2003.1295171

Stewart, I.D., Oke, T.R., 2012. Local Climate Zones for Urban Temperature Studies. Bulletin of the American Meteorological Society 93, 1879–1900. https://doi.org/10.1175/BAMS-D-11-00019.1

Tayyebi, A., Darrel Jenerette, G., 2016. Increases in the climate change adaption effectiveness and availability of vegetation across a coastal to desert climate gradient in metropolitan Los Angeles, CA, USA. Science of The Total Environment 548, 60–71. https://doi.org/10.1016/j.scitotenv.2016.01.049

Thompson, D.R., Gao, B.-C., Green, R.O., Roberts, D.A., Dennison, P.E., Lundeen, S.R., 2015. Atmospheric correction for global mapping spectroscopy: ATREM advances for the HyspIRI preparatory campaign. Remote Sensing of Environment. https://doi.org/10.1016/j.rse.2015.02.010

Trigo, I.F., Monteiro, I.T., Olesen, F., Kabsch, E., 2008. An assessment of remotely sensed land surface temperature. J. Geophys. Res. 113, D17108. https://doi.org/10.1029/2008JD010035

United Nations, Department of Economic and Social Affairs, Population Division. 2015. "World Urbanization Prospects: The 2014 Revision."

United Nations, Department of Economic and Social Affairs, Population Division, 2016. The World's Cities in 2016 - Data Booklet.

U.S. Census Bureau, Geography Division (Department of Commerce), 2012. Population Estimates. URL https://www.census.gov/popest/data/metro/totals/2012/index.html (accessed 6.6.14).

U.S. Census Bureau, Geography Division (Department of Commerce), 2010. 2010 U.S. census demographic profile data (vector digital data).

U.S. Geological Survey, 2013. USGS NED n34w119 1/3 arc-second 2013 1 x 1 degree ArcGrid: U.S. Geological Survey.

Vahmani, P., Hogue, T.S., 2015. Urban irrigation effects on WRF-UCM summertime forecast skill over the Los Angeles metropolitan area. Journal of Geophysical Research: Atmospheres 120, 9869–9881. https://doi.org/10.1002/2015JD023239

Vahmani, P., Hogue, T.S., 2014. Incorporating an Urban Irrigation Module into the Noah Land Surface Model Coupled with an Urban Canopy Model. J. Hydrometeor. 15, 1440–1456. https://doi.org/10.1175/JHM-D-13-0121.1

Voogt, J.A., 2008. Assessment of an Urban Sensor View Model for thermal anisotropy. Remote Sensing of Environment 112, 482–495. https://doi.org/10.1016/j.rse.2007.05.013

Voogt, J.A., Oke, T.R., 1998. Effects of urban surface geometry on remotely-sensed surface temperature. International Journal of Remote Sensing 19, 895–920. https://doi.org/10.1080/014311698215784

Ward, H., Järvi, L., Onomura, S., Lindberg, F., Grimmond, C., 2017. SUEWS Manual: Version 2016a 51.

Ward, H.C., Grimmond, C.S.B., 2017. Assessing the impact of changes in surface cover, human behaviour and climate on energy partitioning across Greater London. Landscape and Urban Planning 165, 142–161. https://doi.org/10.1016/j.landurbplan.2017.04.001

Ward, H.C., Kotthaus, S., Järvi, L., Grimmond, C.S.B., 2016. Surface Urban Energy and Water Balance Scheme (SUEWS): Development and evaluation at two UK sites. Urban Climate 18, 1–32. https://doi.org/10.1016/j.uclim.2016.05.001

Waring, R.H., Landsberg, J.J., 2011. Generalizing plant–water relations to landscapes. J Plant Ecol 4, 101–113. https://doi.org/10.1093/jpe/rtq041

Weng, Q., 2012. Remote sensing of impervious surfaces in the urban areas: Requirements, methods, and trends. Remote Sensing of Environment, Remote Sensing of Urban Environments 117, 34–49. https://doi.org/10.1016/j.rse.2011.02.030

Weng, Q., 2009. Thermal infrared remote sensing for urban climate and environmental studies: Methods, applications, and trends. ISPRS Journal of Photogrammetry and Remote Sensing 64, 335–344. https://doi.org/10.1016/j.isprsjprs.2009.03.007

Weng, Q., Lu, D., Schubring, J., 2004. Estimation of land surface temperature–vegetation abundance relationship for urban heat island studies. Remote Sensing of Environment 89, 467–483. https://doi.org/10.1016/j.rse.2003.11.005

Weng, Q., Quattrochi, D., Gamba, P.E., Quattrochi, D., Gamba, P.E., 2018. Urban Remote Sensing. CRC Press. https://doi.org/10.1201/9781138586642

Wetherley, E.B., McFadden, J.P., Roberts, D.A., 2018. Megacity-scale analysis of urban vegetation temperatures. Remote Sensing of Environment 213, 18–33. https://doi.org/10.1016/j.rse.2018.04.051

Wetherley, E.B., Roberts, D.A., McFadden, J.P., 2017. Mapping spectrally similar urban materials at sub-pixel scales. Remote Sensing of Environment 195, 170–183. https://doi.org/10.1016/j.rse.2017.04.013

Wu, C., 2004. Normalized spectral mixture analysis for monitoring urban composition using ETM+ imagery. Remote Sensing of Environment 93, 480–492. https://doi.org/10.1016/j.rse.2004.08.003

Wu, C., Deng, C., Jia, X., 2014. Spatially Constrained Multiple Endmember Spectral Mixture Analysis for Quantifying Subpixel Urban Impervious Surfaces. IEEE Journal of Selected Topics in Applied Earth Observations and Remote Sensing 7, 1976–1984. https://doi.org/10.1109/JSTARS.2014.2318018

Wu, C., Murray, A.T., 2003. Estimating impervious surface distribution by spectral mixture analysis. Remote Sensing of Environment 84, 493–505. https://doi.org/10.1016/S0034-4257(02)00136-0

Xiao, Q., McPherson, E.G., Simpson, J.R., Ustin, S.L., 2007. Hydrologic processes at the urban residential scale. Hydrological Processes 21, 2174–2188. https://doi.org/10.1002/hyp.6482

Xiao, Q., Ustin, S.L., McPherson, E.G., 2004. Using AVIRIS data and multiple-masking techniques to map urban forest tree species. International Journal of Remote Sensing 25, 5637–5654. https://doi.org/10.1080/01431160412331291224

Yuan, F., Bauer, M.E., 2007. Comparison of impervious surface area and normalized difference vegetation index as indicators of surface urban heat island effects in Landsat imagery. Remote Sensing of Environment 106, 375–386. https://doi.org/10.1016/j.rse.2006.09.003

Zarco-Tejada, P.J., González-Dugo, V., Berni, J.A.J., 2012. Fluorescence, temperature and narrow-band indices acquired from a UAV platform for water stress detection using a micro-hyperspectral imager and a thermal camera. Remote Sensing of Environment 117, 322–337. https://doi.org/10.1016/j.rse.2011.10.007

Zare, A., Ho, K.C., 2014. Endmember Variability in Hyperspectral Analysis: Addressing Spectral Variability During Spectral Unmixing. IEEE Signal Processing Magazine 31, 95–104. https://doi.org/10.1109/MSP.2013.2279177

Zhang, Y., Odeh, I.O.A., Han, C., 2009. Bi-temporal characterization of land surface temperature in relation to impervious surface area, NDVI and NDBI, using a sub-pixel image analysis. International Journal of Applied Earth Observation and Geoinformation 11, 256–264. https://doi.org/10.1016/j.jag.2009.03.001

Zhang, Y., T. Murray, A., Turner II, B.L., 2017. Optimizing green space locations to reduce daytime and nighttime urban heat island effects in Phoenix, Arizona. Landscape and Urban Planning 165, 162–171. https://doi.org/10.1016/j.landurbplan.2017.04.009

Zhao, Q., Myint, S.W., Wentz, E.A., Fan, C., 2015. Rooftop Surface Temperature Analysis in an Urban Residential Environment. Remote Sensing 7, 12135–12159. https://doi.org/10.3390/rs70912135

Zhao, Q., Wentz, E.A., 2016. A MODIS/ASTER Airborne Simulator (MASTER) Imagery for Urban Heat Island Research. Data 1, 7. https://doi.org/10.3390/data1010007

Zhou, W., Wang, J., Cadenasso, M.L., 2017. Effects of the spatial configuration of trees on urban heat mitigation: A comparative study. Remote Sensing of Environment 195, 1–12. https://doi.org/10.1016/j.rse.2017.03.043